

2016

Functional Imaging of the Lungs using Magnetic Resonance Imaging of Inert Fluorinated Gases

Couch, Marcus

<http://knowledgecommons.lakeheadu.ca/handle/2453/739>

Downloaded from Lakehead University, Knowledge Commons

**Functional imaging of the lungs using magnetic resonance imaging of inert
fluorinated gases**

by

Marcus John Couch

A thesis presented to the Faculty of Graduate Studies,
Lakehead University, Thunder Bay, Ontario

A dissertation submitted in partial fulfillment
of the requirements for the degree of
Doctor of Philosophy in Biotechnology

November 9, 2015

© Marcus John Couch 2015



FACULTY OF GRADUATE STUDIES

NAME OF STUDENT: Marcus Couch
DEGREE AWARDED: PhD
ACADEMIC UNIT: Biotechnology PhD
TITLE OF DISSERTATION: Functional imaging of the lungs using magnetic resonance imaging of inert fluorinated gases

This dissertation has been prepared
under my supervision
and the candidate has complied
with the Doctoral regulations.



Signature of Supervisor

November 4, 2015

Date

Supervisor's Name (Printed) Mitchell Albert

Abstract

Fluorine-19 (^{19}F) magnetic resonance imaging (MRI) of the lungs using inhaled inert fluorinated gases can potentially provide high quality anatomical and functional images of the lungs. This technique is able to visualize the distribution of the inhaled gas, similar to hyperpolarized (HP) helium-3 (^3He) and xenon-129 (^{129}Xe) MRI. Inert fluorinated gases have the advantages of being nontoxic, abundant, and inexpensive compared to HP gases. Due to the high gyromagnetic ratio of ^{19}F , there is sufficient thermally polarized signal for imaging, and averaging within a single breath-hold is possible due to short longitudinal relaxation times. Since inert fluorinated gases do not need to be hyperpolarized prior to their use in MRI, this eliminates the need for an expensive polarizer and expensive isotopes. Inert fluorinated gas MRI of the lungs has been studied extensively in animals since the 1980s, and more recently in healthy volunteers and patients with lung diseases.

This thesis focused on the development of static breath-hold inert fluorinated gas MR imaging techniques, as well as the development functional imaging biomarkers in humans and animal models of pulmonary disease. Optimized ultrashort echo time (UTE) ^{19}F MR imaging was performed in healthy volunteers, and images from different gas breathing techniques were quantitatively compared. ^{19}F UTE MR imaging was then quantitatively compared to ^{19}F gradient echo imaging in both healthy volunteers and in a resolution phantom. A preliminary comparison to HP ^3He MR imaging is also presented, along with preliminary ^{19}F measurements of the apparent diffusion coefficient (ADC) and

gravitational gradients of ventilation in healthy volunteers. The potential of inert fluorinated gas MRI in detecting pulmonary diseases was further explored by performing ventilation mapping in animal models of inflammation and fibrosis. Overall, interest in pulmonary ^{19}F MRI of inert fluorinated gases is increasing, and numerous sites around the world are now interested in developing this technique. This work may help to demonstrate that inert fluorinated gas MRI has the potential to be a viable clinical imaging modality that can provide useful information for the diagnosis and management of chronic respiratory diseases.

Keywords:

Lung, Inert fluorinated gas MRI, Hyperpolarized gas MRI, ^{19}F , ^3He , ^{129}Xe , Fractional ventilation, Apparent diffusion coefficient, Inflammation, Ventilation gradients, UTE

Co-Authorship

Chapter 2 of this thesis was published as an original research article titled “Pulmonary ultrashort echo time ^{19}F MR imaging with inhaled fluorinated gas mixtures in healthy volunteers: feasibility” in the peer-reviewed journal *Radiology* in December 2013 (Couch et al. *Radiology*, 2013; 269: 903–909. DOI:10.1148/radiol.13130609). This article has been reproduced with permission from the publisher, and it was co-authored by Marcus J. Couch, Iain K. Ball, Tao Li, Matthew S. Fox, Shalyn L. Littlefield, Birubi Biman, and Mitchell S. Albert.

Chapter 3 of this thesis is a manuscript titled “Optimized strategies for pulmonary ^{19}F MRI using inert fluorinated gases and comparison of ultrashort echo time and gradient echo imaging”. This manuscript is in preparation for submission to a peer-reviewed journal as an original research article, and it was co-authored by Marcus J. Couch, Iain K. Ball, Tao Li, Matthew S. Fox, Alexei V. Ouriadov, Birubi Biman, and Mitchell S. Albert.

Chapter 4 of this thesis includes excerpts from an invited review article, titled “Inert fluorinated gas MRI: a new pulmonary imaging modality”. This article was published in a special issue of the peer-reviewed journal *NMR in Biomedicine* in December 2014 (Couch et al. *NMR in Biomedicine*, 2014; 27: 1525–1534. DOI:10.1002/nbm.3165). Excerpts from this article have been reproduced with permission from the publisher, and this article was co-authored by Marcus J. Couch, Iain K. Ball, Tao Li, Matthew S. Fox, Alexei V. Ouriadov, Birubi Biman, and Mitchell S. Albert.

Chapter 5 of this thesis is a manuscript titled “Fractional ventilation mapping using inert fluorinated gas MRI in a rat model of inflammation”. This manuscript is in preparation for submission to a peer-reviewed journal as an original research article, and it was co-authored by Marcus J. Couch, Matthew S. Fox, Chris Viel, Gowtham Gajawada, Tao Li, and Mitchell S. Albert.

As first author of these manuscripts, I participated in all aspects of the above-mentioned studies, including the literature review, study design, data acquisition, data analysis, statistical considerations, interpretation the results, manuscript drafting, editing, revisions, figure preparation, and table preparation. Iain Ball performed the MRI pulse sequence programming. Tao Li and Gowtham Gajawada assisted with hardware development. Shalyn Littlefield assisted with clinical and regulatory coordination. Iain Ball, Matthew Fox, Tao Li, Gowtham Gajawada, Chris Viel, and Alexei Ouriadov contributed to the data acquisition and analysis. Matthew Fox, Gowtham Gajawada, and Chris Viel performed the animal preparation. Chris Viel performed the histological analysis for the animal studies. Birubi Biman provided clinical expertise as the qualified investigator in the human imaging studies. Mitchell Albert was the principal investigator for all of the human and animal studies in this thesis, and as such, he provided guidance on all aspects of the above studies.

Acknowledgments

I would first like to thank my supervisor, Dr. Mitchell Albert for his guidance throughout this journey. I would also like to thank the members of my advisory committee, Dr. Laura Curiel and Dr. Gautam Das, who provided continued support throughout the development of this dissertation.

Thank you to the past and present members of the Albert lab for your help with long and arduous experiments. Dr. Iain K. Ball, Dr. Matthew S. Fox, Gowtham Gajawada, Tao Li, Dr. Alexei V. Ouriadov and Chris Viel all made significant contributions to this work.

Thanks to Dr. Patricia Alderson for assistance with animal procedures and to Ralph Hashoian at Clinical MR Solutions for making the human RF coils and the interface electronics. I also gratefully acknowledge the Thunder Bay Regional Health Sciences Centre (TBRHSC) MR Technologists for their time and assistance with MR scanning of study participants.

I am thankful for the financial support that made this work possible. All of the studies in this thesis were supported in part by the Thunder Bay Regional Research Institute (TBRRI). I am also grateful for the external fellowships that allowed me to pursue these studies. I was supported by an Ontario Graduate Scholarship (OGS) for 2011–2012 and a Natural Sciences and Engineering Research Council of Canada (NSERC) CGS-D Alexander Graham Bell Canada Graduate Scholarship for 2012–2015.

Table of Contents

Abstract	iii
Co-Authorship	v
Acknowledgments	vii
Table of Contents	viii
List of Tables	xii
List of Figures	xiii
List of Abbreviations	xvii
1 Introduction	1
1.1 Clinical Motivation	1
1.2 Pulmonary Physiology	2
1.3 Pulmonary Function Tests	5
1.4 Conventional Lung Imaging Techniques	7
1.4.1 X-Ray Computed Tomography.....	7
1.4.2 Nuclear Medicine.....	10
1.4.3 Magnetic Resonance Imaging.....	11
1.5 Functional Approaches to Pulmonary MRI	14
1.5.1 ¹ H MRI.....	14
1.5.2 Hyperpolarized Noble Gas MRI	16
1.5.3 Inert Fluorinated Gas MRI.....	19
1.6 Nuclear Magnetic Resonance	24
1.6.1 Nuclear Magnetic Moment	25
1.6.2 Magnetization	26
1.6.3 Precession in a Static Magnetic Field	30
1.6.4 Precession in a Time-Varying Magnetic Field	31
1.6.5 Spin-Lattice Relaxation	34
1.6.6 Spin-Spin Relaxation	36
1.7 Magnetic Resonance Imaging.....	39
1.7.1 Spatial Localization	39

1.7.2	2D Gradient Echo Imaging	42
1.7.2.1	RF Pulse.....	42
1.7.2.2	Slice Selection	44
1.7.2.3	Phase Encoding	45
1.7.2.4	Frequency Encoding and Readout.....	46
1.7.3	3D Gradient Echo Imaging	48
1.7.4	UTE Imaging	49
1.7.5	X-Centric Imaging	52
1.7.6	SNR Considerations.....	54
1.8	Comparison of ^{129}Xe , ^3He , and Inert Fluorinated Gases.....	55
1.9	Thesis Outline	61
1.10	References.....	64
2	Pulmonary Ultrashort Echo Time ^{19}F MR Imaging with Inhaled Fluorinated Gas Mixtures in Healthy Volunteers: Feasibility	78
2.1	Abstract.....	78
2.2	Introduction.....	79
2.3	Methods.....	82
2.3.1	Subjects.....	82
2.3.2	Image Acquisition.....	82
2.4	Results.....	85
2.5	Discussion.....	89
2.6	Conclusion	91
2.7	References.....	92
3	Optimized Strategies for Pulmonary ^{19}F MRI Using Inert Fluorinated Gases and Comparison of Ultrashort Echo Time and Gradient Echo Imaging	95
3.1	Abstract.....	95
3.2	Introduction.....	96
3.3	Methods.....	98
3.3.1	Phantom Measurements	98
3.3.2	Subjects.....	100
3.4	Results.....	102
3.5	Discussion.....	107
3.6	Conclusion	109

3.7	References.....	110
4	Preliminary Measurements of Functional Biomarkers Using ¹⁹F MRI of Inert Fluorinated Gases	112
4.1	Introduction.....	112
4.2	Volume Measurements and Comparison to HP ³ He MRI	113
4.2.1	Introduction.....	113
4.2.2	Methods.....	115
4.2.3	Results.....	117
4.2.4	Discussion	120
4.2.5	Conclusions.....	122
4.3	Diffusion Imaging.....	122
4.3.1	Diffusion Physics	122
4.3.2	Diffusion Measurements in the Lung	125
4.3.3	Preliminary ¹⁹ F ADC Measurements in Human Lungs	127
4.4	Gravitational Distribution of Ventilation.....	130
4.4.1	Introduction.....	130
4.4.2	Methods.....	131
4.4.3	Results and Discussion	132
4.4.4	Conclusions.....	135
4.5	References.....	136
5	Fractional Ventilation Mapping using Inert Fluorinated Gas MRI in Rat Models of Inflammation and Fibrosis	140
5.1	Abstract.....	140
5.2	Introduction.....	141
5.3	Methods.....	145
5.3.1	Animal Preparation	145
5.3.2	MRI.....	146
5.3.3	Data Analysis	147
5.3.4	Histology.....	148
5.4	Results.....	149
5.5	Discussion.....	158
5.6	Conclusion	163
5.7	References.....	164

6 Discussion	169
6.1 Summary.....	169
6.2 ¹⁹ F MRI Developments in Thunder Bay, Ontario.....	170
6.3 Future Work.....	173
6.3.1 Reproducibility and Validation.....	173
6.3.2 Hardware Improvements.....	174
6.3.3 Pulse Sequence Improvements.....	175
6.3.4 Functional Imaging.....	177
6.4 Outlook.....	178
6.5 Conclusion.....	180
6.6 References.....	181
Appendix A: Research Ethics Board Approval	185
Appendix B: Animal Care Committee Approval	191

List of Tables

Table 1-1: Gyromagnetic ratios of a few NMR-sensitive nuclei (122).	25
Table 1-2: A comparison of the physical properties of ^{129}Xe , ^3He and inert fluorinated gases (100,116,127).	56
Table 2-1: Subject demographics, oxygen saturation, and SNR (\pm standard deviation) from all available coronal ^{19}F 3D UTE images. The breathing protocol used for each subject is indicated.	86
Table 3-1: Echo times used for all PFP and SF_6 resolution phantom measurements.	100
Table 3-2: PFP and SF_6 Resolution Phantom Measurements. Mean SNR (\pm standard deviation) from all ^{19}F 3D UTE, 3D gradient echo, and 3D radial images. The SNR was normalized by the square root of the scan duration.	103
Table 3-3: Human Lung Imaging. Mean whole-lung SNR (\pm standard deviation) from all available ^{19}F 3D UTE and gradient echo images that were acquired in the coronal plane...	104
Table 4-1: Comparison of SNR measurements obtained from ^3He and ^{19}F MRI in all subjects.	119
Table 4-2: Comparison of VV, VDV and VDP measurements obtained from ^3He and ^{19}F MR imaging in the lungs of three subjects.	120
Table 4-3: Diffusion coefficients for ^{129}Xe , ^3He , PFP, and SF_6 , in units of [$\text{cm}^2 \cdot \text{s}^{-1}$] (16-18).	125
Table 4-4: Summary of measured ventilation gradients, coefficients of determination (R^2), and percent changes in ventilation along the vertical direction for all six healthy volunteers. The first four volunteers inhaled the PFP/ O_2 mixture as a 1 L bolus, and the last two volunteers inhaled the PFP/ O_2 mixture using the continuous breathing method. ...	133
Table 5-1: Summary of the mean r values and fractional ventilation gradients from all rats in this study.	153
Table 5-2: Summary of the mean alveolar wall thickness and fraction of collagen content from all rats in this study.	157

List of Figures

Figure 1-1: Weibel’s airway branching diagram. Image reproduced with permission (13).	3
Figure 1-2: Lung micrograph showing the structure of the alveoli and branching airways. Image reproduced with permission (13).	4
Figure 1-3: Lung volumes measured with PFTs. Adapted from (12).	6
Figure 1-4: Conventional ^1H MR lung images acquired in (a) a healthy volunteer and (b) a patient with severe COPD.	13
Figure 1-5: HP ^3He MR images acquired from four individuals: (a) healthy, (b) asthma, (c) moderate COPD, and (d) severe COPD. Images were reproduced with permission (100).	18
Figure 1-6: Comparison of centre slice ^1H localizer and ^{19}F UTE images acquired in the coronal and axial planes.	22
Figure 1-7: (a) Coronal ^{19}F 3D MR images obtained in a COPD patient with emphysema. (b) ^{19}F MR lung images overlaid in greyscale on conventional ^1H MR images. Images were reproduced with permission from Halaweish et al. (116).	23
Figure 1-8: Net magnetization of an ensemble of nuclear spins.	26
Figure 1-9: Thermal polarization of an ensemble of nuclear spins.	28
Figure 1-10: Hyperpolarized ensemble of nuclear spins.	29
Figure 1-11: Application of a 90° RF pulse in a rotating reference frame (x' , y' , z').	33
Figure 1-12: Longitudinal relaxation following a 90° RF pulse for three different T_1 values.	35
Figure 1-13: Transverse relaxation following a 90° RF pulse for three different T_2 values. .	37
Figure 1-14: Pulse sequence diagram for a 2D gradient echo image acquisition.	42
Figure 1-15: Three k -space trajectories in a gradient echo pulse sequence.	47
Figure 1-16: Pulse sequence diagram for a 3D gradient echo image acquisition.	49
Figure 1-17: Pulse sequence diagram for a 3D ultrashort echo time (UTE) acquisition.	50
Figure 1-18: Examples of radial k -space trajectories in a UTE image acquisition.	51
Figure 1-19: Pulse sequence diagram for a 2D x-centric image acquisition.	52

Figure 1-20: k -space trajectories for a 2D x-centric pulse sequence. Since x-centric uses a partial echo factor of 50.5%, the sequence is repeated with the opposite readout gradient polarity. In order to preserve visual clarity, the corresponding horizontal lines are offset slightly.....	53
Figure 2-1: Ideal flip angle sweep consisting of 20 spectra with increasing flip angles. ^{19}F spectra were acquired in a fluorinated gas-filled phantom. As expected, a 90° RF pulse yields the highest possible signal intensity.	84
Figure 2-2: ^{19}F 3D UTE lung images acquired in the coronal plane from subject #4 during a 15 s breath-hold, following inhalation of a 1 L mixture of 79% PFP and 21% O_2 from a Tedlar bag. Images were reproduced with permission (25).....	87
Figure 2-3: ^{19}F 3D UTE lung images acquired in the axial plane from subject #5 during a 15 s breath-hold, following inhalation of a 1 L mixture of 79% PFP and 21% O_2 from a Tedlar bag. Images were reproduced with permission (25).....	87
Figure 2-4: ^{19}F 3D UTE lung images acquired in the coronal plane from subject #9 during a 15 s breath-hold, following continuous breathing from a 5 L mixture of 79% PFP and 21% O_2 and a 1 L inhalation of the same mixture. Images were reproduced with permission (25).	88
Figure 2-5: ^{19}F 3D UTE lung images acquired in the axial plane from subject #8 during a 15 s breath-hold, following continuous breathing from a 5 L mixture of 79% PFP and 21% O_2 and a 1 L inhalation of the same mixture. Images were reproduced with permission (25).	89
Figure 3-1: Schematic diagram of the resolution phantom that was used for SF_6 and PFP imaging. The outer diameter was 126 mm, and the diameters of the circular obstructions are shown.	99
Figure 3-2: Comparison of one slice from 3D images that were obtained in a resolution phantom filled with a mixture of (a) 79% PFP and 21% O_2 or (b) 100% SF_6 . Images were acquired using (i) gradient echo, (ii) UTE and (iii) radial acquisitions, at bandwidths of 140 and 200 Hz/pixel.....	102
Figure 3-3: 1D profiles taken from PFP (left) and SF_6 (right) images acquired in the resolution phantom at a bandwidth of 200 Hz/pixel. Note that the horizontal signal profiles for gradient echo, UTE, and radial imaging were offset for visual clarity. The white arrow indicates the 3 mm obstruction, and the black arrow indicates the 10 mm obstruction.....	103
Figure 3-4: Comparison of four central slices from lung images in the coronal plane acquired in subject #3 in the same imaging session: (a) ^1H localizer, (b) ^{19}F 3D UTE, and (c) ^{19}F 3D gradient echo. The UTE images were reproduced with permission (3).	105

Figure 3-5: Comparison of four central slices from lung images in the axial plane acquired in subject #2 in the same imaging session: (a) ^1H localizer, (b) ^{19}F 3D UTE, and (c) ^{19}F 3D gradient echo. The UTE images were reproduced with permission (3). 106

Figure 3-6: Comparison of centre slice coronal (left) and axial (right) MR lung images from ^{19}F 3D UTE (top) and ^{19}F 3D gradient echo (bottom) overlaid in colour on conventional ^1H MR images. The coronal images were acquired in subject #3, while the axial images were acquired in subject #2. 107

Figure 4-1: Schematic diagram of the semi-automated segmentation algorithm. Images were reproduced with permission from Kirby et al. (7)..... 117

Figure 4-2: Comparison of representative (a) ^1H localizer, (b) ^3He 2D gradient echo, (c) ^{19}F 3D gradient echo, and (d) ^{19}F 3D UTE images acquired in the same healthy volunteer. 118

Figure 4-3: Pulse sequence diagram for a 2D gradient echo acquisition with diffusion sensitization along the phase encoding direction. 124

Figure 4-4: Three slices from ^{19}F 3D UTE lung imaging acquired in a healthy volunteer (a) without diffusion weighting ($b = 0 \text{ s}\cdot\text{cm}^{-2}$), and (b) with diffusion weighting ($b = 9.59 \text{ s}\cdot\text{cm}^{-2}$). 127

Figure 4-5: (a) PFP ADC maps measured in a healthy volunteer, and (b) the corresponding histograms for each slice. 128

Figure 4-6: ADC normalized to the self-diffusion coefficient, $D(t)/D_0$, is shown plotted as a function of diffusion time, t . Note that the diffusion time is scaled in dimensionless units by making use of the free diffusion length scale and the surface-to-volume ratio (S/V). Image reproduced with permission (30). 130

Figure 4-7: (a) Whole lung axial projection ^{19}F MR image acquired in a representative healthy volunteer. (b) Signal intensity as a function vertical distance in the lungs. The solid line represents the calculated gradient. Images were reproduced with permission (31). 134

Figure 5-1: Representative conventional ^1H lung images obtained in the axial plane from a control rat (left), an LPS-instilled rat (middle), and a bleomycin-instilled rat (right). 150

Figure 5-2: Representative series of 2D whole-lung projection ^{19}F wash-out images obtained in the axial plane from a control rat (top row), an LPS-instilled rat (middle row), and a bleomycin-instilled rat (bottom row). 151

Figure 5-3: Representative fractional ventilation maps obtained in the axial plane from a control rat (left), an LPS-instilled rat (middle), and a bleomycin-instilled rat (right). 151

Figure 5-4: Comparison of mean r values from all rats in this study. The r values were only significantly different for bleomycin-instilled rats compared to controls ($p = 0.001$). 152

Figure 5-5: Representative fractional ventilation gradients calculated in the anterior/posterior (A/P) direction from a control rat (triangles), an LPS-instilled rat (circles), and a bleomycin-instilled rat (diamonds). 154

Figure 5-6: Comparison of A/P ventilation gradients from all rats in this study. The ventilation gradients were only significantly different for LPS-instilled rats compared to controls ($p = 0.016$)..... 155

Figure 5-7: Representative H&E-stained micrographs obtained from a control rat (left), and LPS-instilled rat (middle), and a bleomycin-instilled rat (right) imaged using a 40x objective..... 155

Figure 5-8: Comparison of the mean alveolar wall thickness from all rats in this study. The alveolar wall thickness was significantly different for LPS-instilled rats compared to controls ($p = 0.032$)..... 156

Figure 5-9: Representative trichrome-stained micrographs obtained from a control rat (left), and LPS-instilled rat (middle), and a bleomycin-instilled rat (right) imaged using a 40x objective..... 157

Figure 5-10: Comparison of the fraction of collagen content for all rats in this study. The collagen content was significantly different for bleomycin-instilled rats compared to both LPS-instilled rats ($p = 0.009$) and controls ($p = 0.010$). 158

List of Abbreviations

ADC	Apparent Diffusion Coefficient
A/P	Anterior/Posterior
BW	Bandwidth
CF	Cystic Fibrosis
CF ₄	Tetrafluoromethane
C ₂ F ₆	Hexafluoroethane
C ₃ F ₈	Octafluoropropane (also referred to as PFP)
COPD	Chronic Obstructive Pulmonary Disease
CT	Computed Tomography
¹⁹ F	Fluorine-19
³ He	Helium-3
FEV ₁	Forced Expiratory Volume in 1 Second
FD	Fourier Decomposition
FID	Free Induction Decay
FOV	Field of View
FRC	Functional Residual Capacity
FVC	Forced Vital Capacity
¹ H	Hydrogen-1
H&E	Hematoxylin and Eosin
HP	Hyperpolarized
ILD	Interstitial Lung Disease
LPS	Lipopolysaccharide
M ₀	Thermal Equilibrium Magnetization
MRI	Magnetic Resonance Imaging
NMR	Nuclear Magnetic Resonance
O ₂	Molecular Oxygen
OE	Oxygen-Enhanced
p _A O ₂	Alveolar Partial Pressure of Oxygen
PET	Positron Emission Tomography

PFP	Perfluoropropane
PFT	Pulmonary Function Test
r	Fractional Ventilation
Rb	Rubidium
RBC	Red Blood Cell
RF	Radio Frequency
SEOP	Spin Exchange Optical Pumping
SF ₆	Sulfur Hexafluoride
SNR	Signal-to-Noise Ratio
SPECT	Single Photon Emission Computed Tomography
SpO ₂	Peripheral Oxygen Saturation
S/V	Surface to Volume Ratio
T ₁	Longitudinal Relaxation Time
T ₂	Transverse Relaxation Time
T ₂ *	Apparent Transverse Relaxation Time
TE	Echo Time
TBRRI	Thunder Bay Regional Research Institute
TCV	Thoracic Cavity Volume
TR	Repetition Time
TV	Tidal Volume
VDP	Ventilation Defect Percent
VDV	Ventilation Defect Volume
Voxel	Volume Element
V/Q	Ventilation to Perfusion Ratio
VV	Ventilated Volume
¹²⁹ Xe	Xenon-129
Xe-CT	Xenon-Enhanced Computed Tomography

Chapter 1

Introduction

1.1 Clinical Motivation

Respiratory diseases, such as asthma, cystic fibrosis (CF), chronic obstructive pulmonary disease (COPD), and interstitial lung disease (ILD), are a very significant world-wide health care burden. Chronic obstructive pulmonary disease (COPD) is associated with progressive and irreversible airflow limitation in the lung (1). COPD encompasses chronic bronchitis and emphysema, which represent airway obstruction and the enlargement of alveoli due to tissue destruction, respectively. COPD is currently one of the six leading causes of death in the United States, and death rates from COPD have been steadily increasing since 1970 (2). In Canada, approximately 4.4% of adults aged 35 and over have COPD (~700,000 people), and this number very likely underestimates the true prevalence of COPD in Canada (3). On the global scale, COPD affects between 9 and 10% of adults aged 40 and over (4). Asthma is associated with airway narrowing and airway wall inflammation in the lung (5). Like chronic bronchitis, asthma leads to airway obstruction and reduced ventilation in the lungs, however, this airway limitation is reversible with treatment (6). It has been estimated that asthma affects between 5 and 16% of the world's population (7).

Interstitial lung diseases (ILD) are a group of pulmonary disorders that affect the interstitial tissues in the alveoli, resulting in inflammation and fibrosis (8). A 20 year old epidemiological study estimated that ILD affects 80.9 per 100,000 men, and 67.2 per 100,000 women in the United States (9). More recent studies have shown that the incidence and mortality of idiopathic pulmonary fibrosis (IPF), one type of ILD, is on the rise (10). Although these numbers seem low compared to COPD and asthma, the prognosis of ILD is generally very poor, as the root cause is sometimes unknown and the basic mechanisms are poorly understood.

Given the substantial prevalence of respiratory diseases, numerous research efforts are currently underway that aim to help improve clinical outcomes. Unfortunately, a number of gaps have been identified in the care of pulmonary diseases, which can lead to an inadequate assessment of diagnosis and treatment progression (11). In other words, there is a problem in translating existing knowledge to routine clinical practice. Therefore, there is a significant need for new and effective methods to diagnose and manage respiratory diseases; these techniques should be relatively low-cost and easily translatable to clinical practice.

1.2 Pulmonary Physiology

The principal function of the lung is to permit gas exchange, where oxygen (O_2) from the air is able to move into venous blood and carbon dioxide (CO_2) is able to move out (12). The lung branches from the trachea into progressively narrower airways until the alveolar

ducts and alveolar sacs are reached. Figure 1-1 shows a diagram of the “airway tree” structure, with approximately 23 generations of branching between the trachea and alveoli (13). The first 15 generations are called the “Conducting Airways”; their purpose is to transport gas and they do not participate in gas exchange. The final 8 generations are called the “Acinar Airways”, which contain alveoli that participate in gas exchange through diffusive mechanisms.

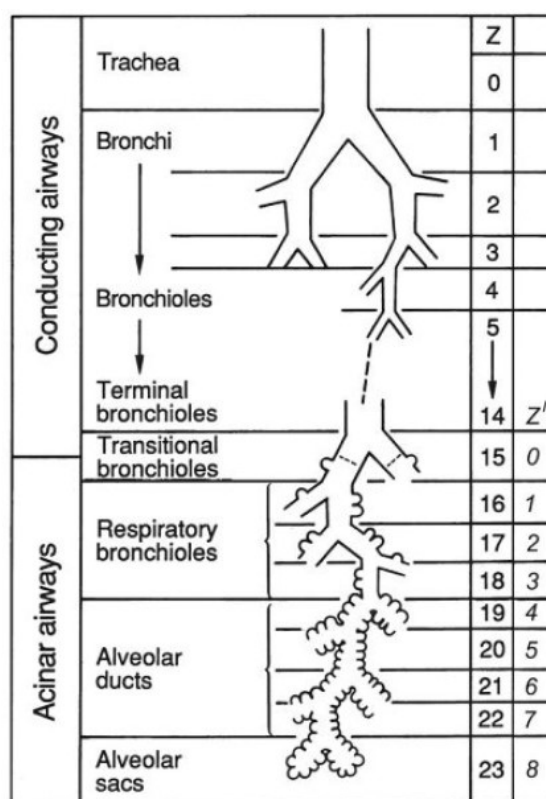


Figure 1-1: Weibel’s airway branching diagram. Image reproduced with permission (13).

There are on average 480 million alveoli in the human lung (14) with a mean diameter of $\sim 200 \mu\text{m}$ (15). Overall, the total surface area available for gas exchange in the human lung is approximately 130 m^2 (13), which is roughly half the size of a tennis court. Figure 1-2 shows a micrograph from a human lung section, where the alveoli appear to have a

sponge-like structure and a terminal bronchiole clearly branches into respiratory bronchioles, alveolar ducts, and alveoli.

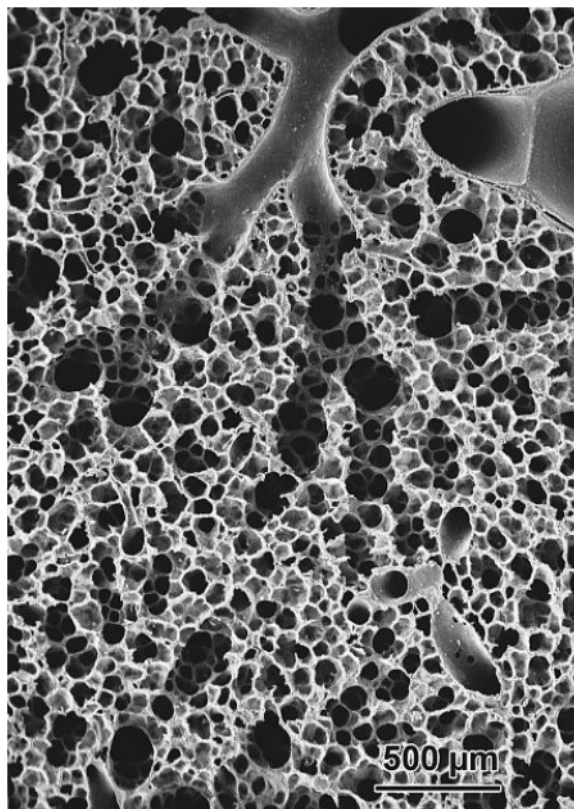


Figure 1-2: Lung micrograph showing the structure of the alveoli and branching airways. Image reproduced with permission (13).

The interested reader is referred to “*Respiratory Physiology: The Essentials*” by John B. West for more details on lung function, ventilation, and gas exchange (12). In addition, the companion volume “*Pulmonary Pathophysiology: The Essentials*” by John B. West offers insight into the pathology, pathogenesis and clinical features of various pulmonary disorders (16).

1.3 Pulmonary Function Tests

Pulmonary function tests (PFTs) are the current gold standard for the diagnosis and assessment of respiratory diseases such as COPD, CF, and asthma (17). One type of PFT is spirometry, which tests lung function by measuring airflow parameters as a function of time while a patient is either inhaling or exhaling through a tube (18). The volume of air that is exhaled in the first second of a forced expiration called the forced expiratory volume (FEV_1), while the total volume exhaled is called the forced vital capacity (FVC) (12). The disease severity can then be evaluated with these parameters as well as ratios such as FEV_1/FVC . For example, COPD is characterized by airflow limitation where both FEV_1 and FVC are expected to decrease; however, FEV_1 generally decreases more than FVC and therefore an FEV_1/FVC ratio less than 0.7 is a typical threshold used to diagnose COPD (17). COPD is further classified into four stages according to the Global Initiative for Chronic Obstructive Lung Disease (GOLD) guidelines (17). These stages are defined according to FEV_1 as a percentage of the predicted value that is normalized based on demographic parameters such as age, sex, height, weight, etc.:

- Stage I (mild) has an FEV_1 of $>80\%$ of the predicted value,
- Stage II (moderate) has an FEV_1 between 50 and 80% of the predicted value,
- Stage III (severe) has an FEV_1 between 30 and 50% of the predicted value,
- Stage IV (very severe) has an $FEV_1 <30\%$ of the predicted value.

Another type of PFT is body plethysmography, which is able to measure lung volumes while a patient is sitting inside an enclosed box (19). By measuring pressure changes inside the box during respiratory efforts, lung volumes can be calculated. Parameters of interest include the residual volume (RV), functional residual capacity (FRC), and total lung capacity (TLC). Figure 1-3 shows how these lung volumes relate to breathing manoeuvres that are performed during PFT measurements. The TLC is the total lung volume after a maximal inspiration, the FRC is the volume remaining after normal expiration, and the RV is the volume remaining after a maximal expiration.

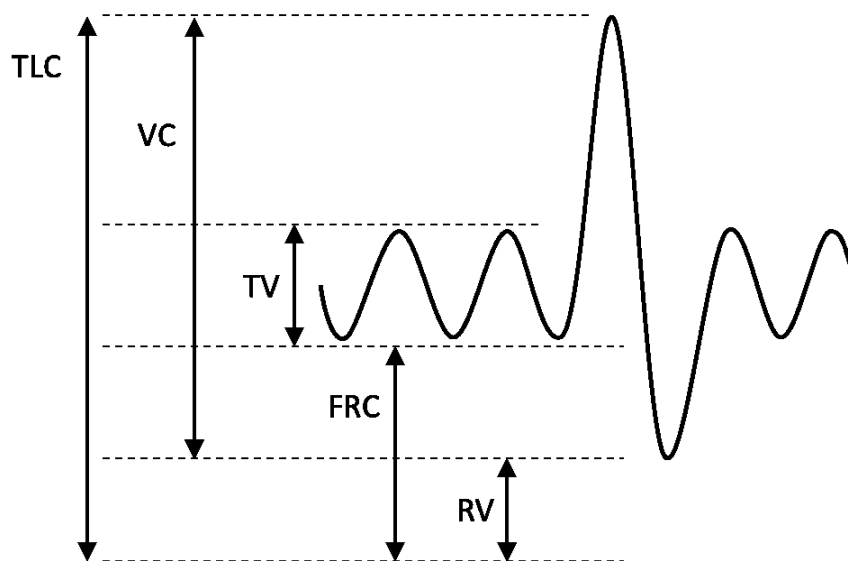


Figure 1-3: Lung volumes measured with PFTs. Adapted from (12).

Other parameters include the vital capacity (VC), which is the volume exhaled following a maximal inspiration, and the tidal volume (TV), which is the volume change during a normal breathing cycle.

In addition to spirometry and plethysmography, other types of PFTs include helium dilution (20), multiple breath nitrogen wash-out (MBNW) (21), and the diffusing capacity of carbon monoxide (D_{LCO}) (22). Although PFTs are considered to be the gold standard diagnostic tools, they do not provide any regional information with respect to lung function, whereas the distribution of lung function is well-known to be heterogeneous and largely driven by gravity (23). A number of non-invasive lung imaging techniques have been developed recently that may be able to provide critical functional and regional information that PFTs lack. Overall, these developments may help to improve the diagnosis and treatment of respiratory diseases.

1.4 Conventional Lung Imaging Techniques

The following sections briefly describe a number of non-invasive imaging techniques that can be used to study lung structure and function, including X-ray computed tomography (CT), single photon emission computed tomography (SPECT), positron emission tomography (PET), and magnetic resonance imaging (MRI). For more details on the physics of these imaging modalities, the interested reader is referred to “*The Essential Physics of Medical Imaging*” by Bushberg et al. (24).

1.4.1 X-Ray Computed Tomography

X-ray computed tomography (CT) of the lung has been performed since the 1970s and it still plays an important role in the diagnosis of respiratory diseases (25). A CT system consists of a rotating gantry mounted with an x-ray tube and detector system.

Transmission measurements are performed at many angles around the patient, and the X-ray attenuation data is used to reconstruct a map of the tissue density. Tissue density is measured on a linear scale in Hounsfield units (HU), which is defined as zero for water, and -1000 for air (26). Therefore, high-density structures, such as bone, appear bright; while low density structures, such as the lungs, appear dark.

Some of the first reports involving quantitative pulmonary CT were published by Hoffman et al. in the 1980s, and these studies examined the volume and shape of the lungs (27), gravitational gradients in the distribution of ventilation (28,29), the effects of orientation on lung expansion (28,29), and models for calculating the fractional air content (30). Pulmonary CT imaging has also been used to study airway narrowing and airway wall thickness in asthmatic subjects (31). CT is also able to quantify emphysema by measuring the fraction of the lung where air spaces have been enlarged due to tissue destruction (32). A threshold CT number is set, typically -950 HU, below which the tissue is considered emphysematous. Therefore, CT is able to phenotype COPD by identifying disease attributes through the measurement of image-based biomarkers (33).

Stable xenon (Xe) gas can be used as a contrast agent in CT imaging to obtain functional information from the lung (34). Since Xe is non-radioactive and denser than air, the measured CT density is directly proportional to the Xe concentration. Dynamic lung imaging during Xe breathing cycles allows for the measurement of wash-in and wash-out characteristics (35), and this technique also permits the calculation of regional ventilation (36). The use of dual-energy CT allows for a direct visualization of the Xe distribution

without the registration artifacts that arise in methods that require a subtraction of enhanced and unenhanced images (37,38). Pulmonary perfusion can also be measured using dual-energy CT by injecting an iodine-based contrast agent (39). Ventilation and perfusion measurements obtained using dual-energy CT have been successfully validated with comparisons to SPECT and conventional CT (40). Recent studies have shown that dual-energy CT is able to provide clinically meaningful information that can be used to evaluate lung function in asthmatic subjects, and ventilation defect scores were shown to correlate with PFT parameters (41).

Overall, CT has the ability to achieve a very high spatial resolution and it has the ability to obtain quantitative functional lung information. However, a significant disadvantage of CT is its use of ionizing radiation, which limits the potential for longitudinal studies, especially in children. The lung is a particularly radiosensitive organ, and the radiation dose delivered during a CT scan of the chest has historically been very high (42). Recent efforts have focused on reducing the CT radiation dosage through the development of novel reconstruction techniques (43) and efficient imaging protocols (44). CT will likely continue to be an important component of clinical pulmonary imaging; however, future developments in CT will have to leverage the quantitative and functional aspects against the need to use ionizing radiation.

1.4.2 Nuclear Medicine

Nuclear medicine refers to techniques that use radioactive tracers for diagnostic purposes, such as SPECT and PET. Both of these techniques can potentially be used to obtain functional lung information; however, the use of nuclear medicine in pulmonary imaging is not as ubiquitous as CT. In SPECT, the regional distribution of ventilation can be studied using the inhalation of technetium-99m (^{99m}Tc)-labelled graphite particles. This technique has been successfully used to study airflow limitation in patients with asthma (45) and emphysema (46). In addition to ventilation-related information, SPECT can also be used to measure the regional distribution of perfusion using an injection of indium-113m (^{113m}In)-labelled albumin. The use of both radioactive tracers, ^{99m}Tc and ^{113m}In , allows for the measurement of the regional ventilation-perfusion ratio (V/Q), which is an important parameter in pulmonary physiology (47). V/Q is directly related to gas exchange, and a ratio of unity indicates a good “matching” between ventilation and perfusion in the lungs (12). On the other hand, V/Q ratios greater or less than 1 are indicative of gas exchange impairment and disease.

Similar to SPECT, PET is an imaging modality that also requires the injection or inhalation of radioactive tracers. The isotopes used for PET imaging, such as ^{11}C , ^{18}F or ^{15}O , emit a positron through β^+ decay. Once the positron encounters an electron, the two particles will annihilate and emit two gamma rays in opposite directions. The final PET image is then reconstructed from measurements of coincident photon detections. Numerous studies have used PET to investigate lung structure and function, including techniques that can determine the tissue volume, blood volume and alveolar gas volume

(48). PET can be used to assess regional ventilation by quantifying the wash-in and wash-out of ^{13}N gas (49). This method can help to identify air trapping in lung compartments that empty slowly. The injection of ^{13}N dissolved in saline also enables the measurement of perfusion with PET, and the wash-out of the dissolved ^{13}N can be used to calculate the V/Q ratio (50,51). These approaches have been used to study ventilation and perfusion in animals models of acute lung injury (52) and pulmonary embolism (53), as well as in humans with methacholine-induced bronchoconstriction (51).

Like CT, nuclear medicine techniques also use significant levels of ionizing radiation, which limits longitudinal studies of lung function (54). Although PET and SPECT have a very high sensitivity, these techniques suffer from a relatively poor spatial resolution compared to CT (47). Furthermore, there are significant problems in the supply chain of radioactive isotopes (55). The National Research Universal nuclear reactor in Chalk River, Ontario produces a substantial fraction of the world's supply of nuclear medicine isotopes, and shifting government priorities have led to an uncertain future for this facility. Therefore, there has been a renewed push to develop alternative methods for isotope production, including the use of cyclotrons.

1.4.3 Magnetic Resonance Imaging

MRI was first demonstrated by Paul Lauterbur in a 1973 *Nature* article (56). In this seminal publication, two-dimensional MR imaging was performed by applying magnetic field gradients to a conventional nuclear magnetic resonance (NMR) system. Crude images were obtained from water-filled capillaries placed inside a tube of heavy water.

In the presence of a magnetic field gradient, the NMR signal is essentially a one-dimensional projection of the sample. A 2D image can then be reconstructed by applying back-projection techniques that are commonly used in CT imaging. Paul Lauterbur proposed that this technique be referred to as “zeugmatography”, meaning the joining of magnetic fields. For these discoveries, Paul Lauterbur won the Nobel Prize in 2003, shared with Peter Mansfield. Despite the fact that Paul Lauterbur’s moniker for this technique didn’t catch on, MRI has revolutionized medical imaging with its ability to provide images with high spatial resolution, good soft tissue contrast, and without the need for ionizing radiation.

Conventional MRI is generally sensitive to thermally polarized hydrogen nuclei (often referred to as protons or ^1H) in water molecules. (The physics of MRI will be discussed in greater detail in Sections 1.6 and 1.7.) Conventional ^1H MRI of the lung has historically been very challenging, owing primarily to a low tissue density that yields a smaller signal than other proton-rich tissues (57). Pulmonary MRI is further confounded by high magnetic susceptibility differences at air/tissue interfaces, which leads to short transverse relaxation times and a short signal lifetime. Furthermore, respiratory and cardiac movement during imaging can lead to motion artifacts. As a result, the lungs generally appear to be a large black signal void in conventional ^1H MR imaging.

Figure 1-4 shows a comparison of conventional ^1H MR lung images acquired in Thunder Bay, Ontario, from a healthy volunteer and a patient with severe COPD. In both of these cases, there is very little MRI signal from inside the lungs, other than the pulmonary

vasculature. The lungs are clearly enlarged in the COPD case, which is to be expected due to a loss of elastic recoil; however, these images in general show very little functional information inside the lungs that might give insight into which portions of the lung are actively participating in ventilation and gas exchange.

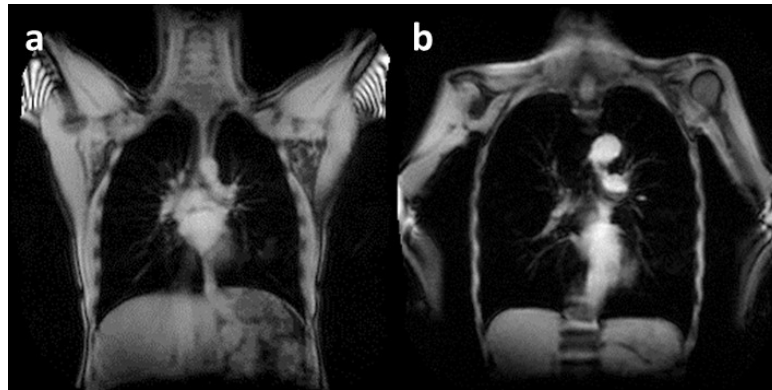


Figure 1-4: Conventional ^1H MR lung images acquired in (a) a healthy volunteer and (b) a patient with severe COPD.

A number of novel and efficient ^1H -based MRI acquisition strategies have been developed for lung imaging, such as balanced steady state free precession (SSFP) (58), ultrashort echo time (UTE) (59), zero echo time (ZTE) (60,61), and pointwise encoding time reduction with radial acquisition (PETRA) (62). These approaches, in combination with respiratory gating, can potentially mitigate all of the traditional shortcomings of conventional ^1H lung MRI; however, the resulting images still provide mainly anatomical details rather than functional information. In spite of this potential disadvantage, these ^1H -based MRI acquisition techniques may still have potential clinical applications, since it has been shown that UTE signal intensity is reproducible, related to tissue density (63), and correlated with PFT parameters and CT metrics in patients with COPD (64).

1.5 Functional Approaches to Pulmonary MRI

1.5.1 ^1H MRI

O_2 -enhanced (OE) ^1H lung MRI is a functional technique that is able to provide ventilation-related information by taking advantage of the ^1H signal enhancement that results from inhaling pure O_2 . Since molecular O_2 is paramagnetic, it tends to shorten the longitudinal relaxation of ^1H in the body and therefore, inhaled O_2 can serve as a contrast agent in pulmonary ^1H MRI. By subtracting an unenhanced MR image obtained during normal air breathing, the resulting signal enhancement is related to the distribution of ventilation. In patients with lung cancer and emphysema, OE MRI is able to detect ventilation defects, which are signal voids that indicate unventilated regions of the lung (65,66). Results from OE MRI have also been shown to agree with nuclear medicine imaging techniques (65).

Dynamic imaging during alternating breathing cycles of air and O_2 can be used to investigate wash-in, wash-out and air trapping (67). A model describing the O_2 wash-in/wash-out kinetics can be used to compute a map of regional ventilation, and this technique yields the expected gravitational gradient in ventilation (68). Regional V/Q ratio measurements have also been demonstrated with ^1H MRI using a combination of three techniques: OE MRI to measure specific ventilation, a modified arterial spin labelling (ASL) approach to measure perfusion, and a fast gradient echo method to measure regional lung density (69). This technique has been used to investigate posture-dependent gradients in the V/Q ratio.

OE MRI can potentially be used to assess pulmonary diseases such as CF, since the resulting images are sensitive to ventilation heterogeneity and changes in tissue density (70). OE MRI has the advantage of being able to be performed on virtually any MRI scanner, and O₂ is a readily available and inexpensive contrast agent. Unfortunately, OE MRI has a few potential disadvantages, and in particular, the O₂-induced signal enhancement is very small. It may be possible to improve the quality of OE MRI with efficient acquisition strategies, such as UTE, but OE MRI may still suffer from a misalignment of enhanced and unenhanced images (i.e. misregistration) (71). Furthermore, it is also unclear whether the O₂-enhancement truly represents ventilation of the air spaces, since the signal change arises from interactions between ¹H in tissue and O₂ (57).

Fourier decomposition (FD) is another ¹H-based MRI technique that is able to obtain functional lung information without the use of a contrast agent (72). This method rapidly acquires free-breathing images at a rate of 3.33 images s⁻¹. Since no form of gating is used during image acquisition, a non-rigid registration algorithm is required to compensate for respiratory motion. A pixel-by-pixel FD of the signal intensity yields spectral peaks corresponding to cardiac and respiratory frequencies, allowing for the calculation of perfusion- and ventilation-weighted images. FD MRI has been shown to be reproducible (73), and it has also been validated with a comparison to SPECT and CT imaging in porcine lungs (74).

FD MRI has been successfully used to image a porcine model of pulmonary embolism (75), and recent work in human lungs has demonstrated the expected ventilation defects

in COPD (76). Ultra-fast SSFP techniques have recently been applied to FD MRI, and significantly improved image quality has been demonstrated (77). Like OE MRI, this technique can be performed on virtually any MRI scanner; however, FD MRI also has a few potential limitations. For example, FD MRI is an indirect method for the acquisition of ventilation and perfusion information. That is, the ventilation and perfusion related “signal” essentially arises from the regional change in ^1H density due to the motion of the chest, and this technique cannot directly image the air space of the lung or blood flow.

1.5.2 Hyperpolarized Noble Gas MRI

The advent of hyperpolarized (HP) noble gas MRI, using helium-3 (^3He) and xenon-129 (^{129}Xe), has substantially improved the ability of MRI to measure anatomical and functional changes in the lung due to disease progression and response to therapy. HP gas MRI of the lung was first demonstrated by Albert et al. in a 1994 *Nature* publication, where HP ^{129}Xe imaging was performed in excised mouse lungs at 9.4 T (78). HP gas MRI can overcome the limitations of conventional ^1H lung MRI by directly visualizing the distribution of the inhaled gases (79). Since 1994, various research groups around the world have performed HP ^3He and ^{129}Xe MRI studies in the lungs of animals (80-82) and humans (83-87).

In conventional ^1H MRI, the signal arises from a net magnetization due to a small population difference of nuclear spins in the presence of an externally applied magnetic field. This population difference is referred to as thermal polarization, and ^1H has a polarization of approximately 9.9×10^{-6} at body temperature and in a clinical magnetic

field strength of 3 T. (Thermal polarization is quantitatively defined in section 1.6.2.) In HP gas MRI, ^3He or ^{129}Xe is pre-polarized outside of the imaging system, yielding a polarization that is 4 – 5 orders of magnitude greater than thermal equilibrium levels (88). Therefore, the available polarization in HP gas MRI is independent of the imaging field strength (89). The hyperpolarization process generally uses a non-equilibrium optical pumping technique, called spin-exchange optical pumping (SEOP) (90). Other hyperpolarization techniques include dynamic nuclear polarization (DNP) (91) and metastability exchange optical pumping (MEOP) (92); however, it should be noted that MEOP can only be used to hyperpolarize ^3He .

The SEOP process begins with circularly polarized laser light that is absorbed by an alkali metal vapour, such as Rubidium (Rb) (90). The circularly polarized laser light excites specific Rb electronic transitions, and the Rb becomes polarized. The angular momentum is then transferred to the noble gas nuclei by collisions. This process is typically performed at high pressure (up to 10 atm) and in the presence of a magnetic field (~a few mT). ^{129}Xe is efficiently polarized at low partial pressure (1 – 3%) and in a continuous flow mode, while pure ^3He is typically polarized in a batch mode for several hours inside a sealed glass vessel. Literature values for the final gas polarization vary considerably depending on the instrumentation as well as temperature and pressure parameters; however, ^3He and ^{129}Xe polarization values up to 50% are typical. Once polarized, imaging can be performed on an MRI scanner that has broadband multinuclear capabilities (i.e. the system can detect nuclei other than ^1H) and dedicated $^3\text{He}/^{129}\text{Xe}$ radio frequency (RF) coils.

HP gas MRI has been used to visualize the lung air spaces in humans with a high degree of reproducibility (93), and image-derived biomarkers show a good correlation with PFTs (94), OE MRI (71) and FD MRI (75,76). HP gas MRI has also been successfully compared to established CT ventilation metrics (95), and it has been shown that HP gas MRI can potentially provide additional functional information that cannot be obtained from CT (83,96). HP gas MR image-derived biomarkers have the ability to phenotype respiratory diseases, and these measurements have been extensively used to investigate diseases such as asthma (97), COPD (83) and CF (98,99). For example, Figure 1-5 shows HP ^3He MR images that were obtained in Thunder Bay, Ontario from a healthy volunteer and three patients with pulmonary diseases: asthma, moderate COPD, and severe COPD.

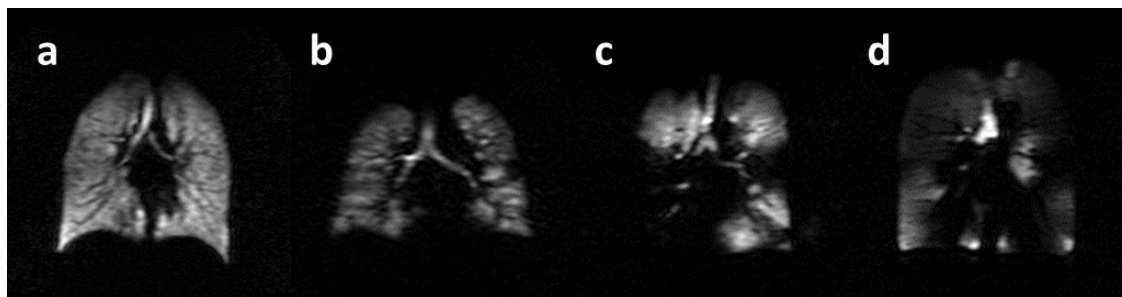


Figure 1-5: HP ^3He MR images acquired from four individuals: (a) healthy, (b) asthma, (c) moderate COPD, and (d) severe COPD. Images were reproduced with permission (100).

The HP ^3He signal is relatively homogeneous in the healthy volunteer, although there is some structure inside the lungs due to the pulmonary vasculature. Similar to OE MRI and FD MRI, ventilation defects can be observed in patients with pulmonary diseases, which are signal voids that indicate the presence of airway obstructions and unventilated lung regions. By co-registering HP gas images with a conventional ^1H lung image, the total ventilated volume (VV), ventilation defect volume (VDV) and ventilation defect percent (VDP) can be measured (101). It has been demonstrated that these metrics can potentially

help to evaluate the severity of COPD, which makes this a very sensitive technique for diagnostic purposes (102).

In addition to static breath-hold ventilation imaging, HP gas MRI can also be used to obtain functional information from the lung, such as the measurement of the apparent diffusion coefficient (ADC), which has been correlated with tissue destruction and emphysema (103-105). By measuring changes in longitudinal relaxation due to the presence of O₂, the regional alveolar partial pressure of O₂ (P_AO₂) can be probed (106-108). Air trapping and the distribution of ventilation dynamics can be assessed by acquiring multiple images at a high temporal resolution throughout a single inspiration, breath-hold and forced expiration (96). These studies have quantified the heterogeneous nature of obstructive lung diseases, demonstrating that HP gas MRI has the ability to provide regional information that is not available from traditional PFTs. Measurements of the regional V/Q ratio obtained from HP gas MRI have the potential to yield a greater spatial resolution than what is currently achievable with SPECT and PET (109). Overall, HP ³He and ¹²⁹Xe MRI have the ability to obtain anatomical and functional information from the lungs using a non-invasive technique that does not require ionizing radiation.

1.5.3 Inert Fluorinated Gas MRI

The first demonstration of gas phase MRI was reported in the 1980s by Edwin Heidelberg and Paul Lauterbur, where pulmonary fluorine-19 (¹⁹F) MR imaging was performed using tetrafluoromethane (CF₄). Heidelberg and Lauterbur were able to acquire crude images in phantoms, excised rabbit lungs (110), and in healthy dog lungs

(111,112) at a field strength of 0.1 T. ^{19}F MR images were obtained during a 25 minute acquisition that resulted in a $65 \times 65 \times 65$ matrix with a resolution of 2 – 3 mm. Unlike HP gases, inert fluorinated gases are imaged without hyperpolarization, which leads to an inherently lower signal-to-noise ratio (SNR). Therefore, little progress was made in the development of inert fluorinated gas MRI for many years, as investigators focused on developing HP gas MRI.

In 1998, Kuethe et al. demonstrated high resolution 3D ^{19}F MR imaging of rat lungs, and images were obtained during continuous breathing of a mixture of hexafluoroethane (C_2F_6) and O_2 (113). These images had an isotropic resolution of 700 μm , and the acquisition took 4.3 hours to complete. It is interesting to note that Kuethe et al. used an image acquisition approach that was very similar to Paul Lauterbur's original demonstration of MRI in 1973, except the image reconstruction used a 3D inverse Fourier transform rather than a back projection approach (56). In the same 1998 paper, Kuethe et al. hypothesized that human lung imaging with inert fluorinated gas MRI would be possible with a similar SNR efficiency as ^1H MRI. This hypothesis was based on two assumptions: that the short longitudinal relaxation of fluorinated gases allows for more averaging than ^1H MRI, and a relatively coarse matrix size of 64×64 would increase the number of ^{19}F nuclei per voxel (113).

Inert fluorinated gas MRI of human lungs was first demonstrated by Wolf and Schreiber et al., and this work was reported at the 2008 annual meeting of the International Society for Magnetic Resonance in Medicine (ISMRM) (114). In this brief report, 2D whole lung

projection images were acquired in a healthy volunteer using a mixture of sulfur hexafluoride (SF_6) and O_2 . These initial images were rather poor in quality, and the SNR was approximately 9. This low SNR was perhaps due to the exceedingly short transverse relaxation of SF_6 in the lungs. Nevertheless, this initial human imaging work was an important benchmark that opened the doors to new developments in this lung imaging modality.

In 2013, inert fluorinated gas 3D UTE MRI was reported in healthy volunteers (115). Figure 1-6 shows a comparison of conventional ^1H MRI and ^{19}F 3D UTE MRI acquired in the lungs of a healthy volunteer. This imaging was performed under breath-hold conditions, following several breaths of a mixture of 79% perfluoropropane (PFP) and 21% O_2 . Similar to HP gas MRI, the ^{19}F signal is fairly bright and homogeneous throughout the lungs of this healthy volunteer. This work was performed at the Thunder Bay Regional Research Institute (TBRRI) in Thunder Bay, Ontario, and it represents the major focus of this thesis. Chapters 2 through 5 discuss the development of inert fluorinated gas MRI in Thunder Bay, Ontario, including imaging performed in both human and animal lungs.

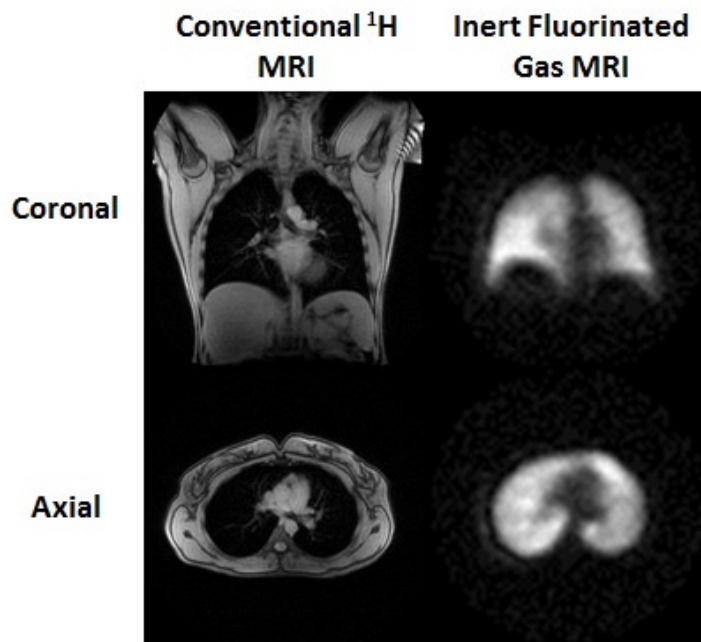


Figure 1-6: Comparison of centre slice ^1H localizer and ^{19}F UTE images acquired in the coronal and axial planes.

In 2013, 3D inert fluorinated gas MRI was also reported in patients with COPD, asthma, and post-lung transplantation (116). This work was performed by Halaweish and Charles et al. at Duke University, and the same inhaled gas mixture of 79% PFP and 21% O_2 was used. Figure 1-7(a) shows an example of 3D ^{19}F MR imaging in the lungs of a COPD patient with emphysema. Although the image quality was rather poor, Halaweish et al. showed that inert fluorinated gas MRI has the ability to detect ventilation defects in patients with COPD, in a manner that is similar to HP gas MRI. Figure 1-7(b) shows the same 3D ^{19}F MR image overlaid in greyscale on a conventional ^1H MR image. Similar to HP gas MRI, this approach can be used to analyze volumetric parameters, such as the VV, VDV, and VDP (101).

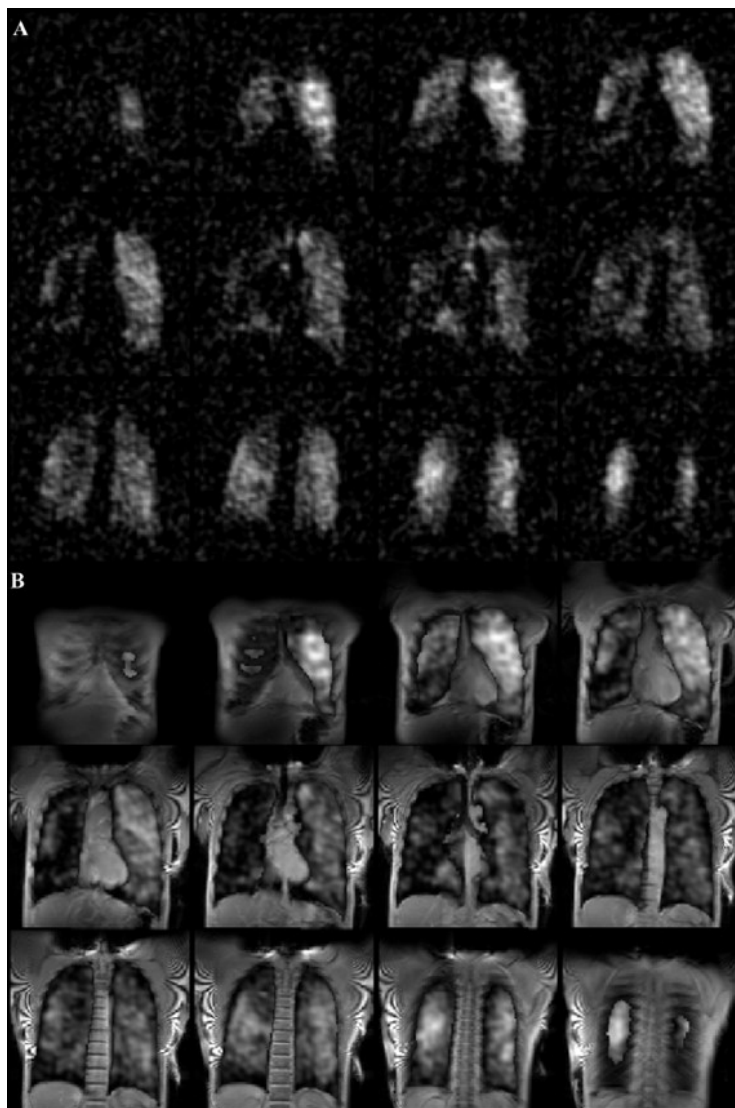


Figure 1-7: (a) Coronal ^{19}F 3D MR images obtained in a COPD patient with emphysema. (b) ^{19}F MR lung images overlaid in greyscale on conventional ^1H MR images. Images were reproduced with permission from Halaweish et al. (116).

Halaweish et al. also developed a custom-built MR-safe gas delivery system to deliver the PFP/O₂ mixture to subjects (117). The computer-controlled delivery system was able to switch between air, O₂, and the fluorinated gas mixture, as well as provide additional information in real-time, such as heart rate, O₂ saturation, O₂/CO₂ concentration, and flow rate. Ideally, a robust gas delivery system can potentially improve patient

compliance, repeatability, as well as provide additional information to aid in the interpretation of inert fluorinated gas images.

Overall, the work to date has demonstrated that inert fluorinated gas MRI is a safe and well-tolerated technique (118), and that it can be performed in volunteers and patients with severe pulmonary diseases. Like HP gas MRI, inert fluorinated gas MRI can be performed on any MRI scanner that has broadband multinuclear capabilities and dedicated RF coils. Moving forward, researchers will focus on validating inert fluorinated gas MRI with rigorous comparisons to existing diagnostic techniques, such as HP gas MRI, CT, and PFTs. This work will help to determine if inert fluorinated gas MRI is able to provide clinically meaningful information that can benefit individuals with pulmonary diseases.

1.6 Nuclear Magnetic Resonance

In order to facilitate a discussion of MRI acquisition techniques for pulmonary imaging in this thesis, the basic principles of nuclear magnetic resonance (NMR) are described in this section, including the nuclear magnetic moment, magnetization, precession in a static magnetic field, precession in a time-varying magnetic field, spin-lattice relaxation, and spin-spin relaxation. Section 1.7 will continue this discussion, by introducing spatial localization and image formation principles. For more details on the physics of NMR, MRI, and image formation, the interested reader is referred to “*Magnetic Resonance*

Imaging: Physical Principles and Pulse Sequence Design” by Haacke et al. (119) and “*Principles of Magnetic Resonance Imaging*” by Dwight G. Nishimura (120).

1.6.1 Nuclear Magnetic Moment

NMR arises from nuclei with an odd number of protons and/or neutrons. Such nuclei possess spin angular momentum, which is given by:

$$\vec{J} = \hbar I, \quad [1-1]$$

where \hbar is the reduced Planck’s constant, and I is the intrinsic half-integer spin. The spin angular momentum causes the nucleus to behave like a spinning charge, which gives rise to a magnetic dipole moment:

$$\vec{\mu} = \gamma \vec{J} = \gamma \hbar I, \quad [1-2]$$

where γ is the gyromagnetic ratio, which is unique to each nucleus and characterizes the ratio of the magnetic dipole moment to the spin angular momentum. The gyromagnetic ratios for a few spin- $\frac{1}{2}$ nuclei of interest are shown in Table 1-1. Nuclei that have a spin greater than $\frac{1}{2}$ can also be NMR-sensitive, such as ^{83}Kr and ^{131}Xe , however these nuclei have a quadrupole moment that leads to relaxation properties that are not ideal for lung imaging (121).

Table 1-1: Gyromagnetic ratios of a few NMR-sensitive nuclei (122).

Nucleus	Spin, I	γ [MHz·rad·T ⁻¹]	$\gamma/2\pi$ [MHz·T ⁻¹]
^1H	$\frac{1}{2}$	267.519	42.577
^3He	$\frac{1}{2}$	-203.814	-32.438
^{13}C	$\frac{1}{2}$	67.280	10.708
^{19}F	$\frac{1}{2}$	251.818	40.078
^{129}Xe	$\frac{1}{2}$	-74.519	-11.860

1.6.2 Magnetization

When placed in an external magnetic field, spins tend to align with the magnetic field, thus giving rise to a net magnetization density:

$$\vec{M} = \lim_{\Delta V \rightarrow 0} \frac{\sum_i \vec{\mu}_i}{\Delta V}, \quad [1-3]$$

where ΔV is a volume of interest. From a classical perspective, this net magnetization, \vec{M} , can simply be interpreted as a vector sum of all the magnetic dipole moments in a sample. A schematic of the net magnetization vector is shown in Figure 1-8 for an external magnetic field, B_0 , that points in the positive z -direction.

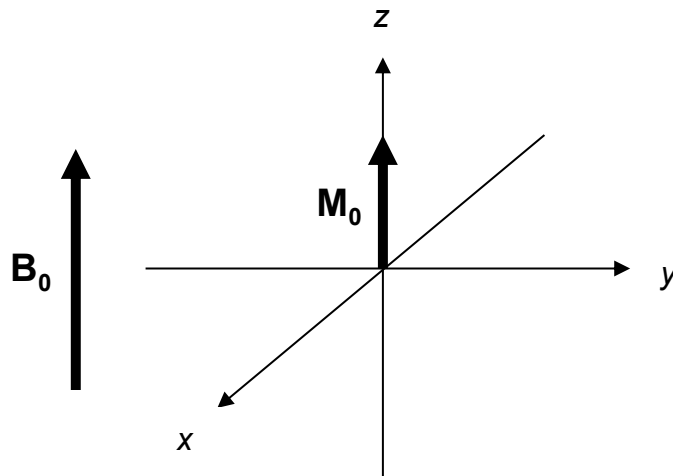


Figure 1-8: Net magnetization of an ensemble of nuclear spins.

A more rigorous treatment from a quantum mechanical perspective will show that the net magnetization vector actually arises from a population difference in energy levels. First, consider the potential energy of a magnetic dipole moment in the presence of a magnetic field, which is defined as the following:

$$E = -\vec{\mu} \cdot \vec{B}_0. \quad [1-4]$$

Using Eq. [1-2], the potential energy can be rewritten to include the spin and gyromagnetic ratio in the following way:

$$E = -\gamma\hbar IB_0. \quad [1-5]$$

Since spin- $1/2$ nuclei can exist in either a “spin-up” or “spin-down” state, the spin has a value of $I = +1/2$ or $I = -1/2$. Therefore, these states are separated by the following quantity of potential energy:

$$\Delta E = \gamma\hbar B_0, \quad [1-6]$$

where the lower energy state is aligned parallel to the magnetic field, and the higher energy state is aligned anti-parallel to the magnetic field. This phenomenon is known as the Zeeman effect (119).

At thermal equilibrium, there will be a slight excess of spins in the $I = +1/2$ state, thereby giving rise to a net polarization, which can be defined with the following expression:

$$P = \frac{N_{\uparrow} - N_{\downarrow}}{N_{\uparrow} + N_{\downarrow}}, \quad [1-7]$$

where N_{\uparrow} is the number of spins aligned with the magnetic field and N_{\downarrow} is the number of spins aligned against the magnetic field. This situation is shown in Figure 1-9 for an ensemble of nuclear spins placed inside a magnetic field, B_0 , and there is a slight excess of spins in the lower energy state.

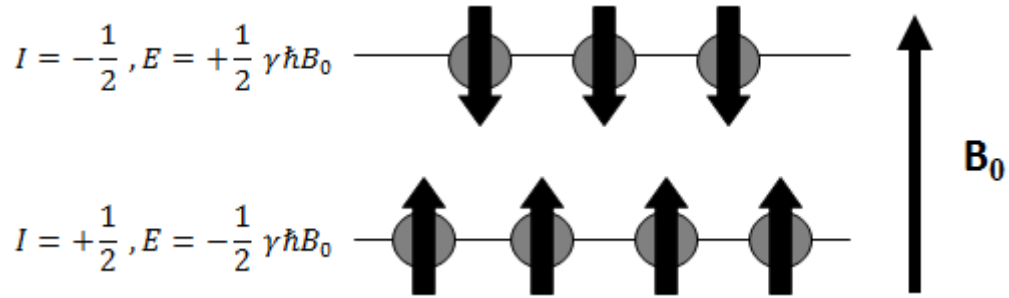


Figure 1-9: Thermal polarization of an ensemble of nuclear spins.

The polarization in Eq. [1-7] can be interpreted as a probability of alignment with the magnetic field, and it can be quantified using the Boltzmann distribution, $e^{-E/kT}$, in the following way:

$$P = \frac{e^{\mu B_0/kT} - e^{-\mu B_0/kT}}{e^{\mu B_0/kT} + e^{-\mu B_0/kT}} = \tanh\left(\frac{\mu B_0}{kT}\right) = \tanh\left(\frac{\hbar\gamma B_0}{2kT}\right). \quad [1-8]$$

Since $2kT$ is typically much greater than $\hbar\gamma B_0$, the polarization in Eq. [1-8] can be approximated in the following way:

$$P \cong \frac{\hbar\gamma B_0}{2kT}. \quad [1-9]$$

If there is no external magnetic field, then the two spin states are degenerate. That is, there is an equal probability of being in either state, leading to a net polarization of zero. At body temperature and in a clinical magnetic field strength of 3 T, the polarization of ^1H is approximately 9.9×10^{-6} . Although this polarization is very small, MR imaging is still possible since there is a large quantity of ^1H nuclei in tissue.

In general, the net magnetization can be related to polarization in the following way:

$$M = N_V \cdot \mu \cdot P, \quad [1-10]$$

where N_V is the number of magnetic dipole moments per unit volume. A final expression for the net magnetization of spin- $\frac{1}{2}$ nuclei can be derived by inserting Eqs. [1-2] and [1-9] into Eq. [1-10]:

$$M_0 = N_V \left(\frac{\hbar\gamma}{2} \right) \left(\frac{\hbar\gamma B_0}{2kT} \right) = \frac{N_V \hbar^2 \gamma^2 B_0}{4kT}, \quad [1-11]$$

where M_0 refers to the thermal equilibrium magnetization.

As noted in Section 1.5.2, HP gas MRI uses ^{129}Xe or ^3He that has been pre-polarized outside of the imaging system via SEOP. The polarization of ^{129}Xe or ^3He can reach 4 – 5 orders of magnitude greater than thermal equilibrium, which yields a greater magnetization density according to Eq. [1-10] and hence a greater MRI signal (88). Therefore, HP media represent a unique case where Eqs. [1-8], [1-9], and [1-11] do not apply. Figure 1-9 shows a schematic diagram of a non-equilibrium hyperpolarized situation, where a much larger fraction of the spins are in the lower energy state and aligned with the magnetic field, B_0 .

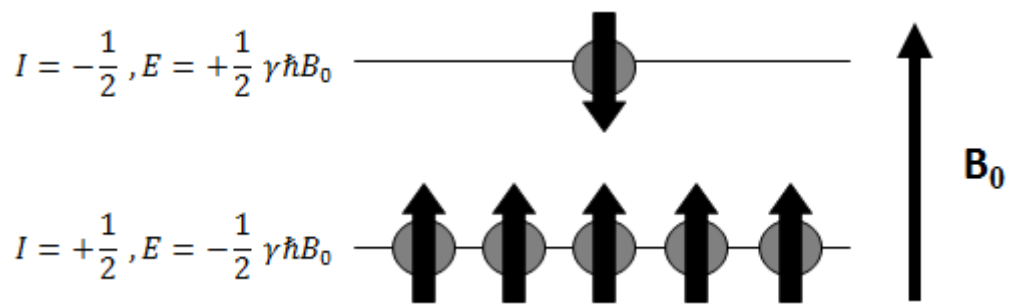


Figure 1-10: Hyperpolarized ensemble of nuclear spins.

1.6.3 Precession in a Static Magnetic Field

At thermal equilibrium, nuclear magnetic moments tend to align with the magnetic field and the net magnetization, \vec{M} , points in the same direction as \vec{B}_0 . If the magnetic moments are perturbed away from the direction of \vec{B}_0 , then they will experience a torque, given by the following expression:

$$\vec{\tau} = \vec{\mu} \times \vec{B}_0. \quad [1-12]$$

By noting that torque is equal to the time derivative of angular momentum, Eq. [1-12] can be rewritten in the following way:

$$\frac{d}{dt} \vec{J} = \vec{\mu} \times \vec{B}_0. \quad [1-13]$$

Multiplying Eq. [1-13] by the gyromagnetic ratio, γ , and inserting Eq. [1-2] yields the following differential equation:

$$\frac{d}{dt} \vec{\mu} = \vec{\mu} \times \gamma \vec{B}_0. \quad [1-14]$$

The nuclear magnetic moment, $\vec{\mu}$, in Eq. [1-14] can be replaced by the net magnetization, \vec{M} , in order to consider the macroscopic behaviour of an ensemble of nuclear spins:

$$\frac{d}{dt} \vec{M} = \vec{M} \times \gamma \vec{B}_0. \quad [1-15]$$

Assuming \vec{B}_0 points in the positive z -direction, the differential equation can be solved to describe the behaviour of the net magnetization vector:

$$M_{xy} = (M_0 \sin \theta) \cdot e^{-i\omega_0 t}, \quad M_z = M_0 \cos \theta, \quad [1-16]$$

where M_{xy} is a rotating vector in the xy -plane composed of $M_x + iM_y$, M_z is the component in the positive z -direction, and θ is the polar angle. Overall, Eq. [1-16] implies

that the net magnetization vector precesses about the magnetic field lines at a frequency of ω_0 . The precessional frequency is also referred to as the Larmor frequency, and it can be calculated using the Larmor equation:

$$\omega_0 = -\gamma B_0. \quad [1-17]$$

Since γ is unique to each nucleus (see Table 1-1), it can be seen from Eq. [1-17] that each nucleus has a unique precessional frequency. The negative factor implies that for positive γ , the magnetization precesses clockwise.

1.6.4 Precession in a Time-Varying Magnetic Field

An NMR signal can be obtained by applying a radio frequency (RF) pulse to a sample. When the RF pulse is applied, there is an additional time-varying magnetic field, denoted as \vec{B}_1 , in a direction perpendicular to the main magnetic field. In general, \vec{B}_1 is a rotating vector in the xy -plane:

$$B_{xy} = |\vec{B}_1| \cdot e^{-i\omega t}, \quad [1-18]$$

where ω is the angular frequency of the RF pulse. Since \vec{B}_1 is a rotating vector, it is convenient to transform the coordinate system to a reference frame rotating about the z -direction at a frequency ω . The total effective field in the rotating reference frame can be described by the following expression:

$$\vec{B}_{eff} = B_1 \hat{i} + \left(B_0 - \frac{\omega}{\gamma} \right) \hat{k}, \quad [1-19]$$

where the \vec{B}_1 field appears stationary along the x -direction, and the longitudinal component appears reduced. If the RF pulse is rotating at exactly the Larmor frequency, then the effective field can be simplified in the following way:

$$\vec{B}_{eff} = B_1 \hat{i} + \left(B_0 - \frac{\omega_0}{\gamma} \right) \hat{k} = B_1 \hat{i}. \quad [1-20]$$

Therefore, the behaviour of the net magnetization vector during an RF pulse can be described by modifying Eq. [1-15] to include \vec{B}_{eff} :

$$\frac{d}{dt} \vec{M} = \vec{M} \times \gamma \vec{B}_{eff} = \vec{M} \times \gamma B_1 \hat{i}, \quad [1-21]$$

where a solution this differential equation would show that the net magnetization vector precesses about the B_1 field in a clockwise fashion at the following frequency:

$$\omega_1 = -\gamma B_1. \quad [1-22]$$

The angle at which the net magnetization vector is rotated away from the z -direction by the RF pulse is referred to as the flip angle. This angle is equal to the magnitude of Eq. [1-22] integrated with respect to time:

$$\theta_1 = \int_0^\tau |\omega_1| dt = \gamma \int_0^\tau B_1 dt. \quad [1-23]$$

After an RF pulse of flip angle θ has been applied, the components of the magnetization vector have the following magnitudes:

$$|M_{xy}| = M_0 \sin \theta, \quad |M_z| = M_0 \cos \theta. \quad [1-24]$$

A schematic diagram of this process is shown in Figure 1-11, where a 90° RF pulse has been applied and the net magnetization has been rotated 90° clockwise about the \vec{B}_1 vector in the rotating reference frame.

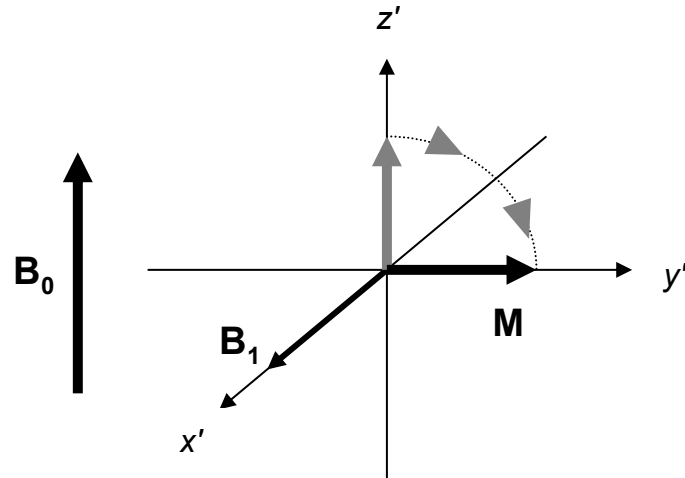


Figure 1-11: Application of a 90° RF pulse in a rotating reference frame (x' , y' , z').

After the RF pulse is turned off, the net magnetization vector continues to precess about the main magnetic field, B_0 , according to Eq. [1-16]. A signal can be detected in the RF coil, since the precessing magnetization produces a changing magnetic flux, Φ , in the coil. Since the RF coil is oriented perpendicular to the main magnetic field, only the transverse component of the magnetization vector, M_{xy} , will induce a signal response. From Eq. [1-24], it can be seen that a 90° RF pulse will yield the highest possible signal.

The detected NMR signal is called a free induction decay (FID), and the electromotive force induced in the coil is given by Faraday's law:

$$S(t) = -\frac{d}{dt} \Phi(t) = -\int_{V_s} dV \left(\frac{d}{dt} \vec{M}(\vec{r}, t) \right) \cdot \vec{B}_1(\vec{r}), \quad [1-25]$$

where $S(t)$ is the received signal in units of volts, $\vec{M}(\vec{r}, t)$ is the magnetization density in the transverse plane at a position \vec{r} , $\vec{B}_1(\vec{r})$ is the magnetic field produced by the RF coil at a position \vec{r} per unit current, and V_s is the volume of the sample. Recognizing that $\vec{M}(\vec{r}, t)$

is a rotating vector of the form $\vec{M}(\vec{r}) \cdot e^{-i\omega_0 t}$, the MRI signal that is received in the RF coil can be rewritten without the explicit time derivative:

$$S(t) = i\omega_0 e^{-i\omega_0 t} \int_{V_s} dV \cdot \vec{M}(\vec{r}) \cdot \vec{B}_1(\vec{r}). \quad [1-26]$$

After the magnetization vector has been perturbed from equilibrium by an RF pulse, the magnetization component in the transverse plane decays via spin-spin relaxation, while the magnetization component in the longitudinal direction re-grows via spin-lattice relaxation. Thus, the net magnetization vector eventually returns to equilibrium. These relaxation mechanisms are described in detail in Sections 1.6.5 and 1.6.6, and they will provide additional factors that affect the received signal that was defined in Eq. [1-26].

1.6.5 Spin-Lattice Relaxation

Spin-lattice relaxation refers to the return to thermal equilibrium along the longitudinal direction. An RF pulse stimulates transitions between the energy states described in Figure 1-9, where the difference between the energy levels is given by $\Delta E = \gamma \hbar B_0$. The system relaxes via interactions with rapidly fluctuating magnetic fields caused by the motion of magnetic dipoles. These time-dependent magnetic fields have frequencies close to γB_0 , causing transitions between the energy states, and returning the system to thermal equilibrium. This relaxation behaves according to the following differential equation:

$$\frac{d}{dt} M_z = -\frac{(M_z - M_0)}{T_1}, \quad [1-27]$$

where M_z is the longitudinal component of the magnetization, M_0 is the thermal equilibrium magnetization, and T_1 is the longitudinal relaxation time constant. Equation [1-27] has the following general solution:

$$M_z(t) = M(0)e^{-t/T_1} + M_0(1 - e^{-t/T_1}), \quad [1-28]$$

where $M(0)$ is the longitudinal magnetization at zero time. If a 90° RF pulse is applied to the sample, then it can be assumed that $M(0) = 0$, and therefore, the magnetization regrows to thermal equilibrium according to the following:

$$M_z(t) = M_0(1 - e^{-t/T_1}). \quad [1-29]$$

The behaviour of the longitudinal magnetization following a 90° RF pulse is shown in Figure 1-12 for three different T_1 values: 10 ms, 250 ms, and 1000 ms.

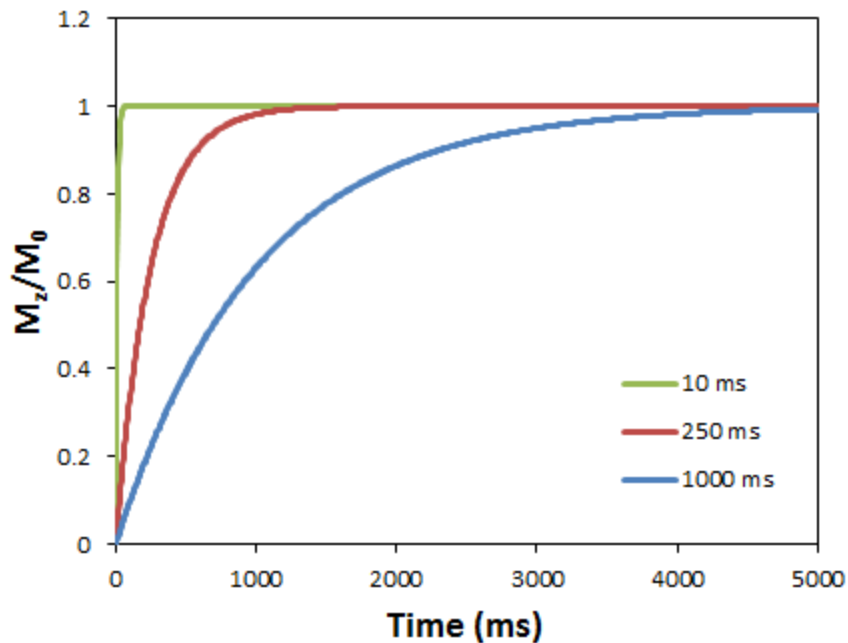


Figure 1-12: Longitudinal relaxation following a 90° RF pulse for three different T_1 values.

A general rule of thumb states that after a duration of $5 \cdot T_1$, the longitudinal magnetization has recovered approximately to thermal equilibrium. Since T_1 can be a function of position, it will be an important factor in determining image quality and contrast. Thus, the signal equation from the preceding section can be modified to include the effects of T_1 :

$$S(t) = i\omega_0 e^{-i\omega_0 t} \int_{V_s} dV \cdot \vec{M}(\vec{r}) \cdot (1 - e^{-t/T_1(\vec{r})}) \cdot \vec{B}_1(\vec{r}). \quad [1-30]$$

The exponential re-growth of longitudinal magnetization applies to conventional ^1H MRI and inert fluorinated gas MRI; however, a few special considerations are required for HP gas MRI. Since HP gases initially have a magnetization that is 4 – 5 orders of magnitude greater than thermal equilibrium levels, the first term in Eq. [1-28] dominates, and the relaxation of the longitudinal magnetization is effectively an exponential decay with a time constant of T_1 . The T_1 of HP gases is environment-dependent, and it can vary from several hours in a strong homogeneous magnetic field to 10s of seconds inside the lungs. Following the application of an RF pulse, the hyperpolarized magnetization does not return to its initially high value. Instead, the longitudinal magnetization continues to decay toward the much smaller M_0 at a rate of $1/T_1$ as indicated by Eq. [1-28].

1.6.6 Spin-Spin Relaxation

Spin-spin relaxation refers to the decay of the magnetization component in the transverse plane. The mechanism for this relaxation is local dipolar interactions, which cause local variations in the z-component of the magnetic field. This leads to a broadening in the

resonance frequency and hence, a dephasing of the transverse magnetization. The decay of the transverse magnetization is governed by the following differential equation:

$$\frac{d}{dt} M_{xy} = -\frac{M_{xy}}{T_2}, \quad [1-31]$$

where M_{xy} is the magnetization in the transverse plane, and T_2 is the transverse relaxation time constant. Equation [1-31] has the following solution:

$$M_{xy}(t) = M(0)e^{-t/T_2}, \quad [1-32]$$

where $M(0)$ is the initial transverse magnetization immediately following the RF pulse. The decay of transverse magnetization following a 90° RF pulse is shown in Figure 1-13 for three different T_2 values: 2 ms, 10 ms, and 100 ms. The T_2 values shown in Figure 1-13 are less than the T_1 values shown in Figure 1-12, and generally speaking, T_2 is always less than or equal to T_1 .

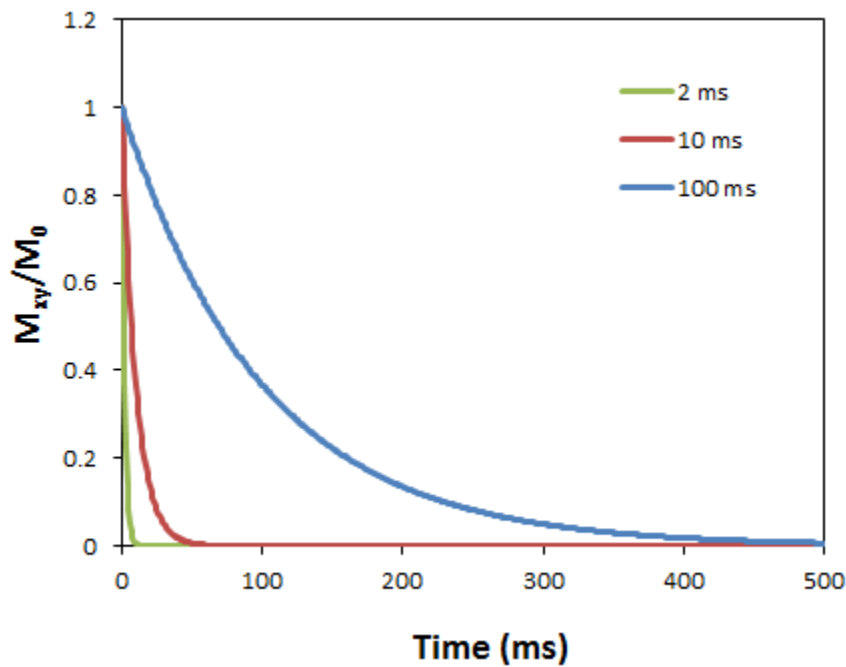


Figure 1-13: Transverse relaxation following a 90° RF pulse for three different T_2 values.

The apparent transverse relaxation time, T_2^* , is shorter than T_2 , since it includes additional components that cause dephasing of the transverse magnetization:

$$\frac{1}{T_2^*} = \frac{1}{T_2} + \frac{1}{T_2'} + \frac{1}{T_{2,susc}}, \quad [1-33]$$

where T_2 is the inherent transverse relaxation due to dipolar interactions, T_2' is the transverse relaxation due to static magnetic field inhomogeneities, and $T_{2,susc}$ is the transverse relaxation due to differences in the magnetic susceptibility of the sample. It should also be noted that diffusion plays a role in modulating spin-spin relaxation arising from magnetic susceptibility differences. The signal expression from Eq. [1-30] can be modified to include T_2^* effects in the following way:

$$S(t) = i\omega_0 e^{-i\omega_0 t} \int_{V_s} dV \cdot \vec{M}(\vec{r}) \cdot (1 - e^{-t/T_1(\vec{r})}) \cdot e^{-t/T_2^*(\vec{r})} \cdot \vec{B}_1(\vec{r}). \quad [1-34]$$

Similar to the T_1 effects described in Section 1.6.5, the T_2^* can vary as a function a position, which can provide a source of image contrast. Furthermore, the T_1 and T_2 effects can be incorporated into Eq. [1-15] in order to fully describe the dynamics of the net magnetization vector:

$$\frac{d}{dt} \vec{M} = \gamma(\vec{M} \times \vec{B}_{eff}) - \frac{M_x \hat{i} + M_y \hat{j}}{T_2} - \frac{(M_z - M_0) \hat{k}}{T_1} \quad [1-35]$$

The x -, y -, and z -components of Eq. [1-35] are often referred to as the phenomenological Bloch equations.

1.7 Magnetic Resonance Imaging

Building on the NMR physics that was introduced in Section 1.6, this section describes the MRI physics of spatial localization and image formation. Spatial localization is first described in general terms, followed by more specific discussions of the MRI data acquisition techniques used in this thesis, including gradient echo imaging, UTE imaging, and x-centric imaging. This section also briefly discusses some SNR considerations that are important for comparing the image quality between different MRI acquisitions.

1.7.1 Spatial Localization

In order to acquire an MR image, the received signal must be spatially localized by applying linear gradient magnetic fields in addition to B_0 . The net magnetic field points in the z -direction, with spatial variations in the x -, y -, or z -directions:

$$\vec{B}(x, y, z) = B_0 \hat{k} + (G_x x + G_y y + G_z z) \hat{k}, \quad [1-36]$$

where $G_x = \frac{dB_z}{dx}$, $G_y = \frac{dB_z}{dy}$ and $G_z = \frac{dB_z}{dz}$. In general, magnetic field gradients can be time-varying, they can be a function of position, \vec{r} , and the combined magnetic field gradient can be written as a single vector in the following way:

$$\vec{G}(\vec{r}, t) = \frac{d}{dx} B_z(t) \hat{i} + \frac{d}{dy} B_z(t) \hat{j} + \frac{d}{dz} B_z(t) \hat{k}. \quad [1-37]$$

The application of a magnetic field gradient has the effect of adding an additional linear phase factor to the signal equation:

$$S(t) = i\omega_0 e^{-i\omega_0 t} \int_{V_s} dV \cdot \vec{M}(\vec{r}) \cdot (1 - e^{-t/T_1(\vec{r})}) \cdot e^{-t/T_2^*(\vec{r})} \cdot \vec{B}_1(\vec{r}) \cdot e^{-i\Delta\varphi(\vec{r},t)}, \quad [1-38]$$

where the phase accumulated during the application of a magnetic field gradient is defined by the following:

$$\Delta\varphi(\vec{r}, t) = \int_0^t dt' \cdot \gamma \cdot \vec{G}(\vec{r}, t') \cdot \vec{r}. \quad [1-39]$$

The accumulated phase in Eq. [1-39] can be simplified by introducing the k -space formalism:

$$\vec{k} = \frac{\gamma}{2\pi} \int_0^t dt' \cdot \vec{G}(t'), \text{ such that } \Delta\varphi(\vec{r}, t) = 2\pi(\vec{k} \cdot \vec{r}). \quad [1-40]$$

Therefore, k -space can be interpreted as a conjugate space where the position in k -space characterizes the amount of phase accumulated by magnetization during the application of magnetic field gradients. Alternatively, k -space can be interpreted as containing information related to spatial frequencies.

The basic objective of spatial localization is to use the received signal to recover a map of the magnetization density, which is inherently modulated by relaxation, the \vec{B}_1 field of the RF coil, and a linear phase factor corresponding to precession.

For the purposes of this discussion, consider an effective magnetization density that incorporates these relaxation, \vec{B}_1 , and phase effects:

$$\hat{M}(\vec{r}) = i\omega_0 e^{-i\omega_0 t} \cdot \vec{M}(\vec{r}) \cdot (1 - e^{-t/T_1(\vec{r})}) \cdot e^{-t/T_2^*(\vec{r})} \cdot \vec{B}_1(\vec{r}). \quad [1-41]$$

Inserting Eqs. [1-40] and [1-41] into [1-38] yields the following signal equation:

$$S(\vec{k}) = \int_{V_s} dV \cdot \hat{M}(\vec{r}) \cdot e^{-i2\pi(\vec{k} \cdot \vec{r})}, \quad [1-42]$$

where the received signal is now a function of the position in k -space and integrated over all of image space. Following data acquisition, with a sufficiently sampled k -space, the effective magnetization density can be recovered by performing an inverse Fourier transform:

$$\hat{M}(\vec{r}) = \int_{k_s} dk \cdot S(\vec{k}) \cdot e^{i2\pi(\vec{k} \cdot \vec{r})}, \quad [1-43]$$

where the effective magnetization density is now a function of the position in image space and integrated over all of k -space.

In order to sufficiently sample k -space prior image reconstruction, MRI uses data acquisition “recipes” called pulse sequences. These pulse sequences use a predetermined set of RF pulses, magnetic field gradient waveforms, and timing parameters. Thus, an MRI scanner is able to excite magnetization, apply the desired phase factors, and acquire data with the desired image contrast. The following sections describe examples of MRI pulse sequences that were used in this thesis, such as 2D gradient echo, 3D gradient echo, UTE, and x-centric.

1.7.2 2D Gradient Echo Imaging

A pulse sequence diagram for a typical 2D gradient echo image acquisition is shown in Figure 1-14. This pulse sequence can be broken down into four main steps, which are described separately below: RF pulse, slice-selection, phase encoding, and frequency encoding. Each time the pulse sequence shown in Figure 1-14 is played out, a single line of data in k -space is acquired. Therefore, the pulse sequence must be repeated many times in order to fully sample k -space, and the duration between each leading RF pulse is defined as the repetition time, TR.

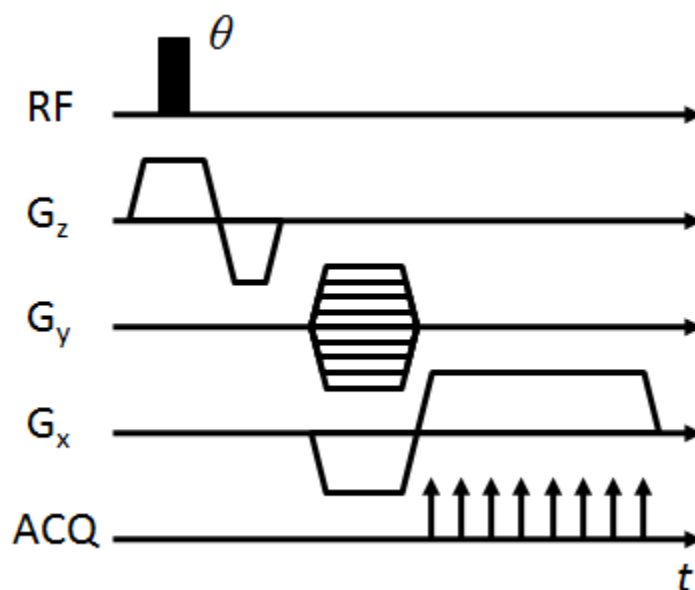


Figure 1-14: Pulse sequence diagram for a 2D gradient echo image acquisition.

1.7.2.1 RF Pulse

The pulse sequence begins with an RF pulse to tip the longitudinal magnetization into the transverse plane. In general, any desired flip angle may be used, and it need not be a constant. Thus, the flip angle and timing parameters are chosen carefully in order to achieve the desired image contrast and to use the available magnetization efficiently. In

conventional ^1H MRI and inert fluorinated gas MRI, there is a trade-off between the between the signal gain from using high flip angles and the available longitudinal magnetization from T_1 relaxation. Therefore, the optimal flip angle for a fixed TR and T_1 is given by the following equation:

$$\theta = \cos^{-1} \left(e^{-\frac{TR}{T_1}} \right), \quad [1-44]$$

where θ is referred to as the Ernst angle, which ensures an optimal SNR efficiency.

As noted in Section 1.6.5, the initially high longitudinal magnetization of HP gases is non-recoverable. Therefore low flip angles are typically used so that the available magnetization can be spread out over the entire data acquisition (123), such that the transverse magnetization following the n th RF pulse is given by the following equation:

$$M_{xy}(n) = M(0) \sin \theta (\cos \theta)^{n-1} e^{-\frac{(n-1) \cdot TR}{T_1}}. \quad [1-45]$$

Eq. [1-45] is often referred to as a constant flip angle (CFA) approach. The disadvantage of using CFA is that the signal strength following each RF pulse will be non-uniform, which has a filtering effect on the final image (i.e. blurring). An alternative technique is to use variable flip angles (VFA), where each successive flip angle is incremented in order to yield a constant signal response as a function of RF pulse number (124).

Each RF pulse has an associated bandwidth, BW_{RF} , or range of precessional frequencies that will be excited. Under the small flip angle approximation (typically less than 30°), the RF bandwidth can be determined by computing the Fourier transform of the RF pulse shape. For simplicity, a rectangular pulse is shown in Figure 1-14, which has a sinc-

shaped profile in the frequency domain. In general, any arbitrary pulse shape may be used, depending on the desired timing parameters and frequency profile.

1.7.2.2 Slice Selection

In order to excite a 2D slice of magnetization, the RF pulse is turned on in the presence of a magnetic field gradient, which is commonly referred to as the slice-select gradient. For illustrative purposes, the slice select gradient is shown in Figure 1-14 in the z -direction. By convention, the z -direction is always in the direction of the magnet bore, and therefore the pulse sequence shown in Figure 1-14 will excite an axial slice of magnetization in the xy -plane. Imaging can also be performed in the axial, coronal or sagittal planes, and a linear combination of gradient magnetic fields can excite any arbitrary plane of magnetization (i.e. an oblique plane).

The thickness of the 2D slice of magnetization is given by the following expression:

$$\Delta z = \frac{BW_{RF}}{\left(\frac{\gamma}{2\pi}\right) G_z}, \quad [1-46]$$

where BW_{RF} is the RF bandwidth, and G_z is the strength of the magnetic field gradient. Since the transverse magnetization accumulates phase while the slice-select gradient is turned on, an additional gradient is applied in the opposite direction to rewind the accumulated phase back to zero. The second gradient lobe has half the area of the first lobe, since most of the magnetization is assumed to be tipped into the transverse plane at the center of the RF pulse.

1.7.2.3 Phase Encoding

Following slice selection, a phase encoding gradient is applied, and this gradient is typically shown in the y -direction for illustrative purposes. While the magnetic field gradient is turned on, the spins precess at a frequency that is a known function of position (i.e. $\omega(y) = \gamma G_y y$). When the gradient is turned off, the spins return to their original precessional frequency, but they retain the phase that was accumulated while the magnetic field gradient was turned on. Therefore, the position in k -space after the phase encoding gradient is turned off is given by the following equation:

$$k_y = \frac{\gamma}{2\pi} T_{PE} \cdot G_y, \quad [1-47]$$

where T_{PE} is the duration of the phase encoding gradient. For simplicity, Eq. [1-47] assumes the integral from Eq. [1-40] was performed over a rectangular gradient waveform, while most gradients actually use a trapezoidal profile.

2D gradient echo imaging samples k -space in a Cartesian fashion, and each repetition of the pulse sequence acquires one line in k -space. Thus, for each line of k -space that is to be acquired, a phase encoding gradient with a slightly different maximum amplitude must be turned on. In other words, each repetition of the pulse sequence moves the acquisition to a different k_y position in k -space. For this reason, multiple overlapping G_y lobes are shown in Figure 1-14. The field of view (FOV) and resolution in the y -direction, Δy , are related to k -space through the following expressions:

$$FOV_y = \frac{1}{\Delta k_y} = \frac{1}{\left(\frac{\gamma}{2\pi}\right) \Delta G_y \cdot T_{PE}}, \quad k_{y,max} = \frac{1}{2\Delta y}, \quad [1-48]$$

where Δk_y is the sampling period in the k_y direction, $k_{y,max}$ is the full extent of k -space coverage in the positive y -direction, and ΔG_y is the difference in the maximum G_y gradient amplitudes for two consecutive lines of k -space.

1.7.2.4 Frequency Encoding and Readout

Following phase encoding, frequency encoding gradients are applied and data acquisition (ACQ) occurs. In Figure 1-14, the frequency encoding gradient is shown in the x -direction. A pre-phasing gradient of negative amplitude is applied first, in order to add phase in the negative k_x -direction. Then a readout gradient with positive amplitude applies phase in the positive k_x -direction, during which data is acquired. The gradient echo is defined as the point during the readout where $k_x = 0$, and the time between the RF pulse and the centre of the gradient echo is called the echo time, TE. If the readout gradient has twice the area of the pre-phasing gradient, then gradient echo occurs at exactly the centre of the readout gradient.

Figure 1-15 shows examples of k -space trajectories for a gradient echo acquisition. Following the RF pulse and slice select gradient, the transverse magnetization has an initial phase of $k_{xy} = 0$. If the pre-phasing gradient is turned on at the same time as the phase-encoding gradient, then the trajectory will move diagonally away from the centre of k -space. When the readout gradient is turned on, the trajectory moves horizontally to the right, and a line of k -space data is collected. Therefore, by repeating the pulse sequence with a slightly different phase encoding gradient, k -space can be uniformly sampled. A 2D inverse Fourier transform of the k -space data yields the image.

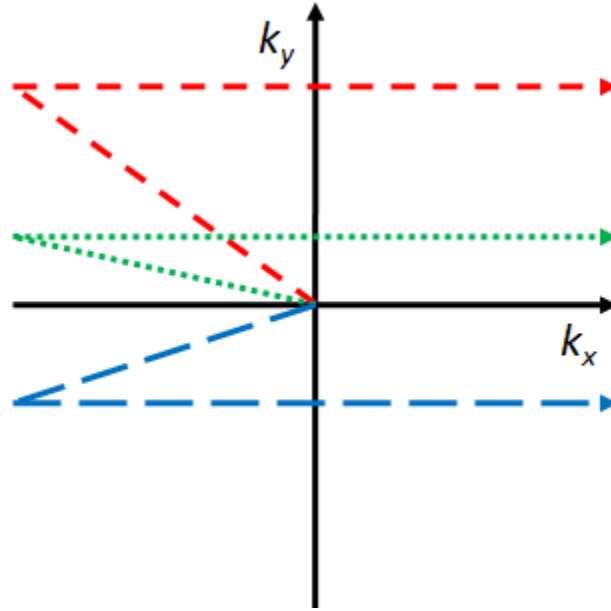


Figure 1-15: Three k -space trajectories in a gradient echo pulse sequence.

In order to reduce the TE and overall scan duration, k -space can be intentionally under-sampled. In such cases, the conjugate symmetry of k -space can be used to reconstruct the correct image. For example, k -space could be under-sampled by only collecting only a fraction of the horizontal lines shown in Figure 1-15. This is achievable by reducing the duration of the pre-phasing gradient, and the fraction of the horizontal line that is actually collected is referred to as the partial echo factor.

Similar to Eq. [1-48], the FOV and resolution in the x -direction, Δx , are related to k -space through the following expressions:

$$FOV_x = \frac{1}{\Delta k_x} = \frac{1}{\left(\frac{\gamma}{2\pi}\right) G_x \cdot \tau_s}, \quad k_{x,max} = \frac{1}{2\Delta x}, \quad [1-49]$$

where G_x is the strength of the readout gradient, and τ_s is the time required to sample each data point. The readout bandwidth is simply the inverse of the sampling time:

$$BW_{read} = \frac{1}{\tau_s}. \quad [1-50]$$

Thus, k -space is adequately sampled when the following Nyquist condition is met (119):

$$n_{kx}n_{ky} \geq 4(k_{max} \cdot FOV)^2, \quad [1-51]$$

where n_{kx} and n_{ky} are the number sampled k -space points in the k_x - and k_y -directions, respectively.

1.7.3 3D Gradient Echo Imaging

With a few modifications, the 2D gradient echo image acquisition described in Section 1.7.2 can be extended to 3D imaging. Figure 1-16 shows a pulse sequence diagram for a typical 3D gradient echo image acquisition. 3D acquisitions generally use “hard” RF pulses, which have a short duration and broad excitation profile in the frequency domain. The magnitude of the slice selection gradient can be reduced in order to excite a thick slab of magnetization, or slice selection can be omitted completely. In Figure 1-16, phase encoding gradients are applied simultaneously in two directions, G_y and G_z , followed by frequency encoding gradients along G_x . The k -space trajectory for a 3D gradient echo is very similar to the 2D case shown in Figure 1-15, except the G_z phase encoding gradients also apply phase in the k_z -direction before the readout in the k_x -direction.

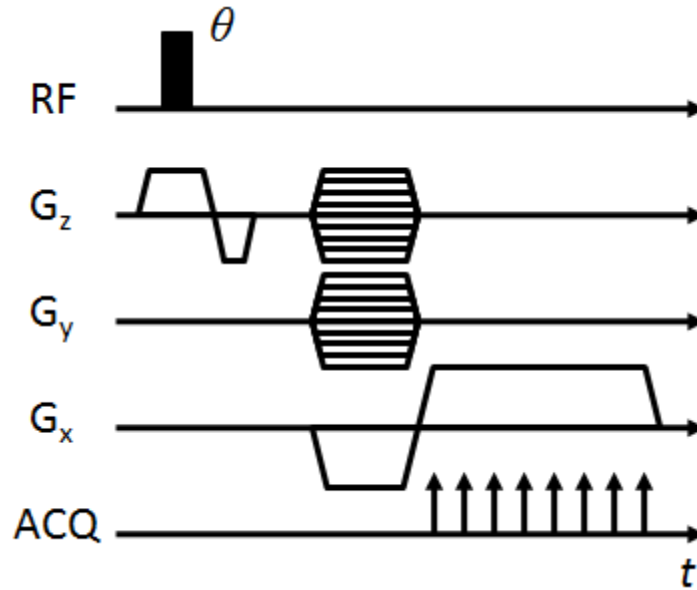


Figure 1-16: Pulse sequence diagram for a 3D gradient echo image acquisition.

It should be noted that since more phase encoding steps are needed to acquire a 3D image, the acquisition time will be significantly increased compared to 2D imaging. Once a 3D k -space dataset has been sufficiently sampled, a 3D inverse Fourier transform can be used to reconstruct the final 3D image.

1.7.4 UTE Imaging

The primary purpose of UTE is to enable imaging of signal sources that have very short T_2^* relaxation times (125). Figure 1-17 shows a pulse sequence diagram of the 3D UTE acquisition used in this thesis. Similar to 3D imaging, UTE uses a hard RF pulse. Instead of using slice or slab selection, a brief phase encoding gradient is played out along G_z . Readout gradients are then played out in both the G_x and G_y directions. Unlike gradient echo imaging, where data acquisition only occurs during the gradient waveform plateau, UTE data acquisition occurs starting at the beginning of the trapezoidal gradient ramp.

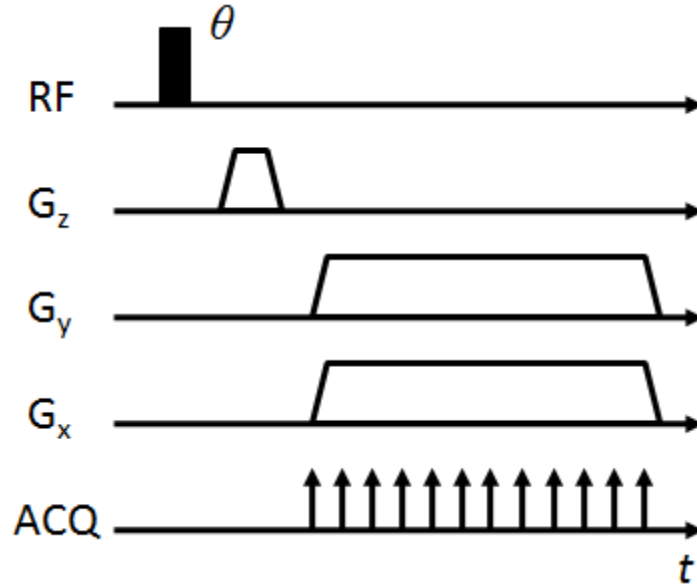


Figure 1-17: Pulse sequence diagram for a 3D ultrashort echo time (UTE) acquisition.

Since the G_x and G_y gradients shown in Figure 1-17 are of equal magnitude, the resulting k -space trajectory will be a radial spoke that starts at the centre of k -space and is 45° from both the k_x - and k_y -axes. For each repetition of the pulse sequence, a different linear combination of G_x and G_y gradients is used to acquire many different radial spokes to fill up k -space. A few examples of these radial k -space trajectories are shown in Figure 1-18. Since UTE uses a polar coordinate system rather than Cartesian sampling, k -space data points are closer together near the center of k -space and further apart near the edge of k -space. As a result, more radial spokes need to be acquired in order to adequately sample k -space. That is, radial k -space trajectories have the following Nyquist condition (119):

$$n_{kr}n_{k\theta} \geq 2\pi(k_{max} \cdot FOV)^2, \quad [1-52]$$

where n_{kr} and $n_{k\theta}$ are the number sampled k -space points in the radial and polar directions, respectively. Therefore, fully sampled UTE acquisitions will likely be longer than gradient echo imaging.

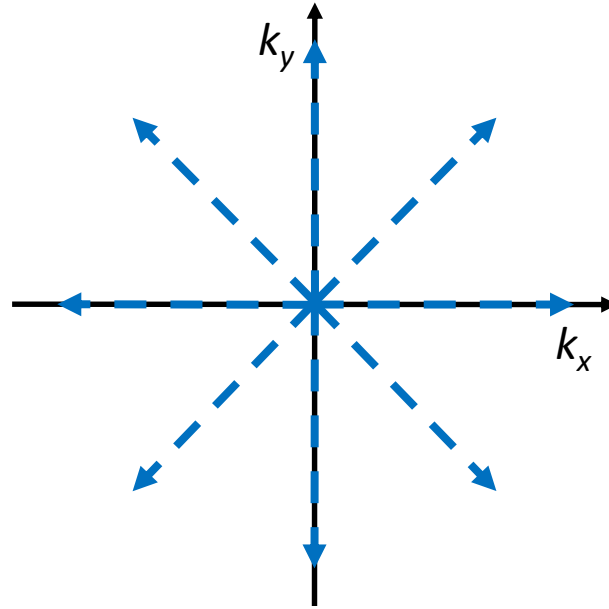


Figure 1-18: Examples of radial k -space trajectories in a UTE image acquisition.

With additional phase encoding in the k_z -direction, the final 3D k -space dataset will look like a “stack of stars”. The k -space data is then gridded onto a Cartesian plane using interpolation techniques, and a 3D inverse Fourier transform is used to reconstruct the 3D final image.

It should also be noted that other variants of UTE appear in the literature, such as ZTE (60), and PETRA (62). Most notably, UTE imaging in the literature generally uses a 3D isotropic approach, where the image resolution is exactly the same in each of the x -, y -, and z -directions (59). This is accomplished by omitting the phase encoding gradient in the z -direction and replacing it with a readout gradient. This modification can substantially reduce the TE, and with many linear combinations of readout gradients in the x -, y -, and z -directions, the resulting k -space trajectories resemble a koosh ball. Similar to the stack of stars UTE approach, image reconstruction requires gridding and a

3D inverse Fourier transform. Based on the timing and geometric parameters that were desired, the stack of stars UTE approach was the primary technique used for ^{19}F human lung imaging in this thesis.

1.7.5 X-Centric Imaging

X-centric imaging is a Cartesian technique that ensures a short TE and short acquisition window, which is especially important for imaging short T_2^* signal sources. The x-centric pulse sequence is essentially a variant of 2D gradient echo imaging with a partial echo factor of 50.5% (123,126). Figure 1-19 shows an example of an x-centric pulse sequence diagram. In this case, the RF pulse, slice select gradient, and phase encoding gradient are the same as for 2D gradient echo imaging; however, the pre-phasing gradient along the x -direction is very small. Thus, the TE will be very short, since k -space trajectories take less time to pass through $k_x = 0$.

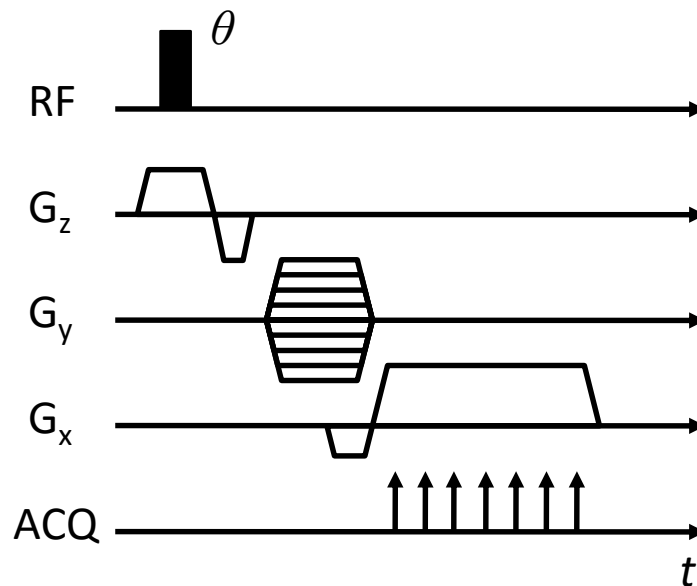


Figure 1-19: Pulse sequence diagram for a 2D x-centric image acquisition.

Each repetition of the x-centric pulse sequence will acquire half of a horizontal line in k -space, plus a few additional points prior to $k_x = 0$. Some examples of x-centric k -space trajectories are shown in Figure 1-20. The gradients shown in Figure 1-19 will produce k -space trajectories that acquire data in the positive x -direction. In order to acquire a complete horizontal line in k -space, the pulse sequence is repeated with the opposite readout gradient polarity. The extra points prior to $k_x = 0$ allow for phase correction prior to joining the two halves of k -space. Similar to 2D gradient echo imaging, a simple 2D inverse Fourier transform of the phase-corrected and joined k -space data yields the final image. Unlike UTE imaging, gridding and interpolation is not required for image reconstruction.

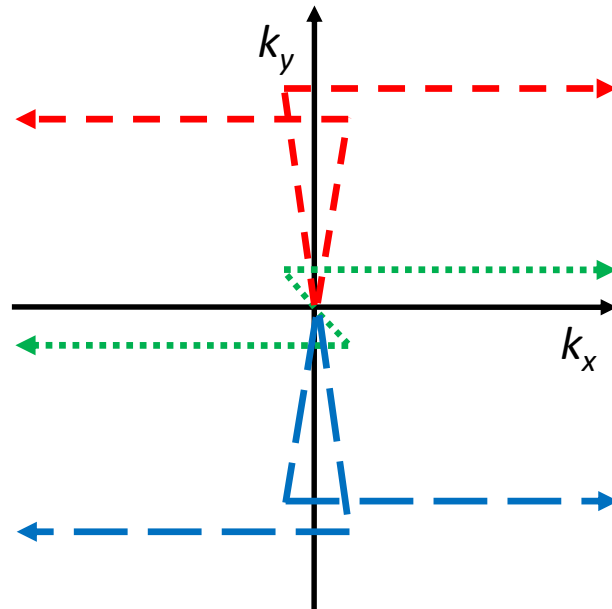


Figure 1-20: k -space trajectories for a 2D x-centric pulse sequence. Since x-centric uses a partial echo factor of 50.5%, the sequence is repeated with the opposite readout gradient polarity. In order to preserve visual clarity, the corresponding horizontal lines are offset slightly.

1.7.6 SNR Considerations

The signal-to-noise ratio (SNR) is a very simple indicator of image quality, and it is generally defined as the mean signal value divided by the standard deviation of the noise. As discussed in Section 1.6, the received signal is dependent on factors such as the available magnetization, flip angle, T_1 , T_2 , and T_2^* . In addition, the choice of pulse sequence and timing parameters have a substantial impact on SNR. For example, if the TR is used to control the amount T_1 recovery and the TE is used to control the amount of T_2^* decay, the SNR is as follows:

$$SNR \propto \left(1 - e^{-\frac{TR}{T_1}}\right) e^{-\frac{TE}{T_2^*}}. \quad [1-53]$$

The above relationship essentially determines the image contrast, which might be T_1 - and/or T_2^* -weighted given a particular TR and TE. In addition, the SNR is also dependent on the voxel size and acquisition time in the following way:

$$SNR \propto (\text{voxel size}) \cdot \sqrt{\text{readout time}} \\ \propto \Delta x \cdot \Delta y \cdot \Delta z \cdot \sqrt{\frac{N_{avg} N_x N_y N_z}{BW}}. \quad [1-54]$$

where Δx , Δy , and Δz are the physical dimensions of the voxel (i.e. resolution); N_{avg} is the number of signal averages; N_x is the number of readout points in the x -direction; N_y and N_z are the number of phase encodes in the y - and z - directions, respectively; and BW is the readout bandwidth (i.e. the inverse of the sampling time).

A major focus of this thesis involves comparing the SNR and image quality from various acquisition strategies, such as UTE and gradient echo, as well as comparing the image

quality from various signal sources, including inert fluorinated gases and HP gases. Given the preceding discussion regarding MRI data acquisition, there are many factors that contribute to image SNR. One approach to comparing the image quality from different acquisitions would be to calculate the SNR efficiency, which corrects for differences in relaxation effects and pulse sequence parameters. Although SNR efficiency can potentially provide a robust and quantitative comparison, this thesis focused more on the pragmatic aspects of lung imaging and its potential applications. In practice, lung imaging is typically constrained by the length of time that a subject is able to hold their breath, and this factor puts an upper limit on how much k -space sampling can occur within a breath-hold (i.e. the readout time in the above SNR equation). Therefore, instead of presenting comparisons of SNR efficiencies, the comparisons presented in this thesis represent the highest possible SNR that can be achieved within a breath-hold for a given set of conditions.

1.8 Comparison of ^{129}Xe , ^3He , and Inert Fluorinated Gases

After discussing basic NMR and MRI principles, these concepts can now be used to understand how the differences in the physical properties of the inhaled gases relate to the imaging parameters and acquisition techniques that are needed for pulmonary imaging. ^{129}Xe , ^3He , PFP, and SF_6 are all non-toxic gases that can safely be used in MR imaging of lungs; however, they have vastly different properties that must be taken into account in order to design an imaging protocol that yields the highest possible signal quality. A

comparison of the physical properties of ^{129}Xe , ^3He , PFP, and SF_6 is shown below in Table 1-2.

Table 1-2: A comparison of the physical properties of ^{129}Xe , ^3He and inert fluorinated gases (100,116,127).

Parameter	^{129}Xe	^3He	^{19}F (PFP)	^{19}F (SF_6)
Nuclear Spin, I	1/2	1/2		1/2
Gyromagnetic ratio, γ , [$\text{MHz}\cdot\text{rad}\cdot\text{T}^{-1}$]	-74.519	-203.814		251.818
Natural Abundance [%]	26.4	1.37×10^{-4}		100
Chemical shift range, $\Delta\delta$ [ppm]	250	0.8		150*
Spin-lattice relaxation time in the lungs, T_1	20 s	25 s	12.4 ms [†]	1.2 ms [†]
Self-diffusion coefficient, D_0 , [$\text{cm}^2\cdot\text{s}^{-1}$]	0.061	2.05	0.023	0.033
Diffusion coefficient in air, D , [$\text{cm}^2\cdot\text{s}^{-1}$]	0.14	0.86	0.071	0.094
Ostwald solubility, L	0.17	0.0085	5.2×10^{-4}	5.4×10^{-3}
Density, [$\text{g}\cdot\text{L}^{-1}$]	5.75	0.134	8.17	6.51

*Approximate chemical shift between PFP and SF_6 resonances. PFP also has two peaks which are separated by ~ 48 ppm.

[†]The reported T_1 values of PFP and SF_6 assume the gas is mixed with $\sim 20\%$ O_2 .

^{129}Xe , ^3He , and ^{19}F are all NMR sensitive nuclei, as they have a nuclear spin of $\frac{1}{2}$. ^3He and ^{19}F have high gyromagnetic ratios compared to ^{129}Xe , which leads to a greater signal strength. At thermal equilibrium, Eq. [1-38] demonstrates that the received signal is proportional to γ^3 , with one factor of γ coming from the precessional frequency and two factors incorporated into the magnetization density (i.e. one from the magnetic moment and one from thermal polarization). For HP gases, the polarization depends on external non-equilibrium factors, and therefore, the received signal scales according to γ^2 .

^3He , PFP, and SF_6 all have a negligible solubility (88,128), whereas ^{129}Xe is able to dissolve into blood and tissue. Due to the large chemical shift range of ^{129}Xe , unique

spectral peaks can be detected that correspond to the lung airspaces, barrier tissues, and red blood cells (RBCs). Therefore, HP ^{129}Xe allows for the measurement of perfusion and gas exchange in the lungs (129-133), as well as sensory stimulation in the brain (134,135). It should also be noted that Xe has anaesthetic properties in high concentrations (136), and therefore safety considerations must be taken into account when developing human breathing protocols (137). Fluorinated gases are non-toxic and safe for human inhalation, as they are commonly used in pulmonary function tests, such as SF_6 (albeit in small concentrations) in the multiple inert gas elimination technique (MIGET) (138). Inert fluorinated gases have other medical imaging applications, such as fluorinated microbubbles that are used as contrast agents in ultrasound (139). Preliminary imaging results have shown that the inhalation of highly concentrated fluorinated gas mixtures has been well tolerated (115,116); however, future work will continue to evaluate safety and tolerability on an ongoing basis. In addition, PFP and SF_6 are very heavy gases compared to ^3He , and the density of ^{129}Xe is slightly less than the density of SF_6 . Future studies will need to determine whether the high density of inert fluorinated gases adversely affects the resulting images and the functional biomarkers that are derived from those images.

The T_1 relaxation times of PFP and SF_6 in the lungs are substantially shorter than HP gases (115,140-142). In HP gas MRI, T_1 characterizes the decay of the HP magnetization back to thermal equilibrium, and therefore a long T_1 (i.e. on the order of tens of seconds) is beneficial for imaging within a single breath-hold. In the context of inert fluorinated gas MRI, a short T_1 is advantageous, since averaging is necessary to overcome a thermal

polarization that has much less available magnetization than HP gases. Therefore, it is possible to use a short TR (i.e. a few ms for SF₆ and a few tens of ms for PFP) and many averages to acquire inert fluorinated gas MR lung images within a single breath-hold.

There are several different fluorinated gases that can potentially be used in ¹⁹F MRI, including PFP, SF₆, CF₄, and C₂F₆. However, the choice of gas for a particular experiment depends on a number of factors, including the number of ¹⁹F nuclei per molecule, differences in relaxation properties, availability, and the need for medical grade mixtures. The human inert fluorinated gas MR imaging presented in this thesis used PFP as the inhaled signal source, while SF₆ was used in the animal work presented in this thesis. Both PFP and SF₆ have six magnetically equivalent ¹⁹F nuclei; however, PFP has two additional ¹⁹F nuclei that contribute to a smaller signal peak that is separated from the main peak by about 48 ppm. The RF excitation bandwidth used in this thesis was less than the chemical shift between the two PFP peaks, and therefore, no substantial chemical shift artifacts are visible in PFP images.

PFP was primarily used in human imaging due to its ideal T₁ relaxation time. PFP has a T₁ of about 12 ms in human lungs, and at a TR of 20 ms, the Ernst angle of 79° would yield the highest possible SNR efficiency. In this thesis, a flip angle of 70° was used for human lung imaging due to RF power limitations. The RF coil used in this thesis had a minimal reflected power (-16 dB or ~2.5%), whereas the transmitting path from the 4 kW RF amplifier suffered from 3 dB losses that resulted in an available RF power of approximately 2 kW at the coil. Since SF₆ has a much shorter T₁, using similar Ernst

angle conditions would require either a shorter TR or a higher flip angle (compared to the PFP settings). Therefore, PFP was ideal for human imaging because it would not have been possible to image SF₆ under Ernst angle conditions, given the limits on the available RF power. However, SF₆ was ideal for animal imaging, since small animal RF coils require less power. SF₆ imaging in animal lungs is possible under near-Ernst angle conditions with a TR of 4 ms and a flip angle of 70°. Therefore, the shorter T₁ of SF₆ is advantageous, because more averaging is possible with SF₆ compared to PFP during the same breath-hold duration.

Since O₂ is paramagnetic, it strongly affects the T₁ of ¹²⁹Xe and ³He. Under ideal conditions (i.e. a perfectly homogeneous external magnetic field), the T₁ of HP ¹²⁹Xe and ³He can be on the order of several hours (88), whereas the T₁ is reduced to a few tens of seconds inside the lungs and in the presence of O₂. In fact, the T₁ of ¹²⁹Xe and ³He is proportional to the concentration of O₂, and this relationship can be exploited to map the alveolar partial pressure of oxygen (p_AO₂) (108). On the other hand, the T₁ relaxation of inert fluorinated gases is dominated by spin rotation interactions (i.e. the coupling of nuclear spins to local magnetic fields produced by the rotation of large molecules) (143), and the T₁ is generally on the order of a few milliseconds. Since the presence of O₂ has a much less dramatic effect on the T₁ of fluorinated gases than it does for HP gases, fluorinated gases can be mixed with O₂ to improve patient safety with little impact on image quality.

The presence of O₂ in inert fluorinated gas mixtures can potentially allow for longer scans than anoxic HP gas inhalations. Whereas HP gas inhalations have historically used a bolus inhalation on the order of 1 L and a 10 – 15 s breath-hold, a mixture of inert fluorinated gases and O₂ can be breathed continuously. After several breaths of the gas mixture, the concentration of inert fluorinated gases will reach a steady state in the lungs, thereby maximizing the available magnetization for imaging. Continuous breathing of inert fluorinated gases also allows for dynamic imaging measurements, such as wash-in and wash-out time constants, and it can potentially allow for the acquisition of more physiologically meaningful information (144-146). Likewise, multiple breath HP gas imaging techniques are now being explored for the measurement physiologically meaningful biomarkers; however, these techniques require additional considerations to account for potential signal losses due to O₂ and T₁ (147,148).

In terms of cost, ³He is an exceedingly rare and expensive isotope, and its only means of production is through the radioactive decay of tritium (88). The high costs of ³He are also partly due to the US government sequestering ³He for use in neutron detectors for national security (149,150). For this reason, investigators are now turning their attention towards HP ¹²⁹Xe imaging, since the source gas is cheaper and more widely available. ¹²⁹Xe arguably has a better chance than ³He of being clinically adopted as a routine pulmonary imaging modality; however, the majority of the ¹²⁹Xe literature uses gas mixtures that have been isotopically enriched with up to 90% ¹²⁹Xe (compared to naturally abundant Xe gas that contains 26% ¹²⁹Xe). Therefore, HP ¹²⁹Xe can also be very

expensive, and investigators are now exploring the feasibility of imaging using naturally abundant Xe gas mixtures (80,151).

SEOP-based polarizers are now commercially available for the production of HP ^3He and ^{129}Xe for clinical studies (Polarean, Inc. and Xemed LLC). Improvements in polarizer technology are ongoing (152), including the development of an “open source” 3D-printed design (153,154); however it should be noted that polarizers require a substantial capital investment, as well as ongoing maintenance costs and specialized personnel. Conversely, inert fluorinated gases do not need to be hyperpolarized prior to their use in MRI, which obviates the need for expensive polarizer technology. Furthermore, inert fluorinated gases are relatively abundant and inexpensive compared to HP gases, as they have numerous industrial applications, such as in semiconductor processing and electrical insulation (155). It should also be noted that fluorinated gases are potent greenhouse gases (156), and therefore, minimizing the environmental impact will be an important consideration. Fortunately, fluorinated gases do not deplete atmospheric ozone (113); however, future developments will continue to investigate gas delivery systems that have the ability to capture and recycle the exhaled gases (117).

1.9 Thesis Outline

Chapter 1 has described the motivation for studying respiratory diseases, basic lung physiology and PFTs. An overview of lung imaging using various functional imaging modalities was presented, including CT, nuclear medicine, conventional ^1H MRI, HP gas

MRI, and inert fluorinated gas MRI. The basic principles of NMR and MRI physics were presented, followed by a comparison of the physical properties of the inhaled gases used in this thesis: ^{129}Xe , ^3He , PFP, and SF_6 .

Chapters 2 through 5 are briefly described below; these chapters represent work that was completed in partial fulfillment of the requirements for the degree of Doctor of Philosophy in Biotechnology at Lakehead University. Chapter 2 describes the first inert fluorinated gas MR imaging study that was performed in Thunder Bay, Ontario. In this work, ^{19}F 3D MR imaging was performed in a group of healthy volunteers using an optimized UTE technique, and images from different gas breathing techniques were quantitatively compared. This work was published in the peer-reviewed journal, *Radiology*, in 2013.

Since inert fluorinated gas MRI is a technique that is still under development, comparisons between various acquisition techniques are required in order to fully optimize the image quality. Chapter 3 describes a quantitative comparison of inert fluorinated gas MR imaging performed using both UTE and gradient echo imaging. In this work, ^{19}F MR imaging was performed in both healthy volunteers and in a resolution phantom. This work is currently in preparation for submission to a peer-reviewed journal as an original research article.

Chapter 4 discusses initial efforts to quantify imaging biomarkers using inert fluorinated gas MRI. This chapter presents a preliminary comparison of inert fluorinated gas MRI

and HP ^3He MRI, along with preliminary measurements of ^{19}F ADC and gravitational gradients of ventilation in healthy volunteers. Portions of Chapter 4 were published in the peer-reviewed journal, *NMR in Biomedicine*, as a review article in 2014.

In order to demonstrate the potential for using image-derived biomarkers to provide quantitative functional information, Chapter 5 presents an inert fluorinated gas MRI ventilation mapping study that was performed in rat models of pulmonary inflammation and fibrosis. Fractional ventilation was compared between disease model rats and healthy controls, and the presence of inflammation was confirmed by histology. This work is currently in preparation for submission to a peer-reviewed journal as an original research article.

Chapter 6 provides a brief summary of this work and discusses possible future directions. Overall, this work may help to demonstrate that inert fluorinated gas MRI has the potential to become a routine clinical imaging modality that can provide diagnostic information that can aid in the management of chronic respiratory diseases.

1.10 References

1. Barnes PJ. Chronic obstructive pulmonary disease. *N Engl J Med* 2000;343(4):269-280.
2. Jemal A, Ward E, Hao YP, Thun M. Trends in the leading causes of death in the United States, 1970-2002. *Jama-J Am Med Assoc* 2005;294(10):1255-1259.
3. O'Donnell DE, Hernandez P, Kaplan A, Aaron S, Bourbeau J, Marciniuk D, Balter M, Ford G, Gervais A, Lacasse Y, Maltais F, Road J, Rucker G, Sin D, Sinuff T, Voduc N. Canadian Thoracic Society recommendations for management of chronic obstructive pulmonary disease - 2008 update - highlights for primary care. *Can Respir J* 2008;15 Suppl A:1A-8A.
4. Vijayan VK. Chronic obstructive pulmonary disease. *Indian J Med Res* 2013;137(2):251-269.
5. Carroll N, Elliot J, Morton A, James A. The structure of large and small airways in nonfatal and fatal asthma. *Am Rev Respir Dis* 1993;147(2):405-410.
6. Celli BR. The importance of spirometry in COPD and asthma: effect on approach to management. *Chest* 2000;117(2 Suppl):15S-19S.
7. Martinez FD, Vercelli D. Asthma. *Lancet* 2013;382(9901):1360-1372.
8. Saag KG, Kline JN. Interstitial Lung Diseases. In: Baum GL, Crapo JD, Celli BR, Karlinsky JB, editors. *Textbook of Pulmonary Diseases*. 6th Edition. Philadelphia, PA: Lippincott-Raven; 1998. p 341-365.
9. Coultas DB, Zumwalt RE, Black WC, Sobonya RE. The epidemiology of interstitial lung diseases. *Am J Respir Crit Care Med* 1994;150(4):967-972.
10. Gribbin J, Hubbard RB, Le Jeune I, Smith CJ, West J, Tata LJ. Incidence and mortality of idiopathic pulmonary fibrosis and sarcoidosis in the UK. *Thorax* 2006;61(11):980-985.
11. Boulet LP, Bourbeau J, Skomro R, Gupta S. Major care gaps in asthma, sleep and chronic obstructive pulmonary disease: a road map for knowledge translation. *Can Respir J* 2013;20(4):265-269.
12. West JB. *Respiratory Physiology*. 9th Edition. Philadelphia: Lippincott Williams & Wilkins; 2012.
13. Weibel ER. What makes a good lung? *Swiss Med Wkly* 2009;139(27-28):375-386.

14. Ochs M, Nyengaard JR, Jung A, Knudsen L, Voigt M, Wahlers T, Richter J, Gundersen HJ. The number of alveoli in the human lung. *Am J Respir Crit Care Med* 2004;169(1):120-124.
15. Hansen JE, Ampaya EP. Human air space shapes, sizes, areas, and volumes. *J Appl Physiol* 1975;38(6):990-995.
16. West JB. *Pulmonary Pathophysiology*. 8th Edition. Philadelphia: Lippincott Williams & Wilkins; 2013.
17. Rabe KF, Hurd S, Anzueto A, Barnes PJ, Buist SA, Calverley P, Fukuchi Y, Jenkins C, Rodriguez-Roisin R, van Weel C, Zielinski J. Global strategy for the diagnosis, management, and prevention of chronic obstructive pulmonary disease: GOLD executive summary. *Am J Respir Crit Care Med* 2007;176(6):532-555.
18. Miller MR, Hankinson J, Brusasco V, Burgos F, Casaburi R, Coates A, Crapo R, Enright P, van der Grinten CP, Gustafsson P, Jensen R, Johnson DC, MacIntyre N, McKay R, Navajas D, Pedersen OF, Pellegrino R, Viegi G, Wanger J. Standardisation of spirometry. *Eur Respir J* 2005;26(2):319-338.
19. Criece CP, Sorichter S, Smith HJ, Kardos P, Merget R, Heise D, Berdel D, Kohler D, Magnussen H, Marek W, Mitfessel H, Rasche K, Rolke M, Worth H, Jorres RA. Body plethysmography--its principles and clinical use. *Respir Med* 2011;105(7):959-971.
20. O'Donnell CR, Bankier AA, Stiebellehner L, Reilly JJ, Brown R, Loring SH. Comparison of plethysmographic and helium dilution lung volumes: which is best for COPD? *Chest* 2010;137(5):1108-1115.
21. Schibler A, Schneider M, Frey U, Kraemer R. Moment ratio analysis of multiple breath nitrogen washout in infants with lung disease. *Eur Respir J* 2000;15(6):1094-1101.
22. Hegewald MJ. Diffusing capacity. *Clin Rev Allergy Immunol* 2009;37(3):159-166.
23. West JB. Regional differences in the lung. *Chest* 1978;74(4):426-437.
24. Bushberg JT, Seibert JA, Jr. EML, Boone JM. *The Essential Physics of Medical Imaging*. Second Edition. Philadelphia: Lippincott Williams & Wilkins; 2002.
25. Brown LR, Muhm JR. Computed tomography of the thorax. Current perspectives. *Chest* 1983;83(5):806-813.
26. Simon BA. Regional ventilation and lung mechanics using X-Ray CT. *Acad Radiol* 2005;12(11):1414-1422.

27. Hoffman EA, Sinak LJ, Robb RA, Ritman EL. Noninvasive quantitative imaging of shape and volume of lungs. *J Appl Physiol Respir Environ Exerc Physiol* 1983;54(5):1414-1421.
28. Hoffman EA. Effect of body orientation on regional lung expansion: a computed tomographic approach. *J Appl Physiol* 1985;59(2):468-480.
29. Hoffman EA, Ritman EL. Effect of body orientation on regional lung expansion in dog and sloth. *J Appl Physiol* 1985;59(2):481-491.
30. Hoffman EA, Acharya RS, Wollins JA. Computer-aided analysis of regional lung air content using three-dimensional computed tomographic images and multinomial models. *Mathematical Modelling* 1986;7(5-8):1099-1116.
31. King GG, Muller NL, Pare PD. Evaluation of airways in obstructive pulmonary disease using high-resolution computed tomography. *Am J Respir Crit Care Med* 1999;159(3):992-1004.
32. Litmanovich D, Boiselle PM, Bankier AA. CT of pulmonary emphysema--current status, challenges, and future directions. *Eur Radiol* 2009;19(3):537-551.
33. Han MK, Agusti A, Calverley PM, Celli BR, Criner G, Curtis JL, Fabbri LM, Goldin JG, Jones PW, Macnee W, Make BJ, Rabe KF, Rennard SI, Sciurba FC, Silverman EK, Vestbo J, Washko GR, Wouters EF, Martinez FJ. Chronic obstructive pulmonary disease phenotypes: the future of COPD. *Am J Respir Crit Care Med* 2010;182(5):598-604.
34. Simon BA. Non-invasive imaging of regional lung function using x-ray computed tomography. *J Clin Monit Comput* 2000;16(5-6):433-442.
35. Chon D, Simon BA, Beck KC, Shikata H, Saba OI, Won C, Hoffman EA. Differences in regional wash-in and wash-out time constants for xenon-CT ventilation studies. *Respir Physiol Neurobiol* 2005;148(1-2):65-83.
36. Marcucci C, Nyhan D, Simon BA. Distribution of pulmonary ventilation using Xe-enhanced computed tomography in prone and supine dogs. *J Appl Physiol* 2001;90(2):421-430.
37. Thieme SF, Hoegl S, Nikolaou K, Fisahn J, Irlbeck M, Maxien D, Reiser MF, Becker CR, Johnson TR. Pulmonary ventilation and perfusion imaging with dual-energy CT. *Eur Radiol* 2010;20(12):2882-2889.
38. Fuld MK, Halaweish AF, Newell JD, Jr., Krauss B, Hoffman EA. Optimization of dual-energy xenon-computed tomography for quantitative assessment of regional pulmonary ventilation. *Invest Radiol* 2013;48(9):629-637.
39. Fuld MK, Halaweish AF, Haynes SE, Divekar AA, Guo J, Hoffman EA. Pulmonary perfused blood volume with dual-energy CT as surrogate for

- pulmonary perfusion assessed with dynamic multidetector CT. *Radiology* 2013;267(3):747-756.
40. Thieme SF, Graute V, Nikolaou K, Maxien D, Reiser MF, Hacker M, Johnson TR. Dual Energy CT lung perfusion imaging-Correlation with SPECT/CT. *Eur J Radiol* 2010.
 41. Chae EJ, Seo JB, Lee J, Kim N, Goo HW, Lee HJ, Lee CW, Ra SW, Oh YM, Cho YS. Xenon ventilation imaging using dual-energy computed tomography in asthmatics: initial experience. *Invest Radiol* 2010;45(6):354-361.
 42. Mayo JR, Jackson SA, Muller NL. High-resolution CT of the chest: radiation dose. *AJR Am J Roentgenol* 1993;160(3):479-481.
 43. Sieren JP, Hoffman EA, Fuld MK, Chan KS, Guo J, Newell JD, Jr. Sinogram Affirmed Iterative Reconstruction (SAFIRE) versus weighted filtered back projection (WFBP) effects on quantitative measure in the COPD Gene 2 test object. *Med Phys* 2014;41(9):091910.
 44. Newell JD, Jr., Sieren J, Hoffman EA. Development of quantitative computed tomography lung protocols. *J Thorac Imaging* 2013;28(5):266-271.
 45. Pellegrino R, Biggi A, Papaleo A, Camuzzini G, Rodarte JR, Brusasco V. Regional expiratory flow limitation studied with Technegas in asthma. *J Appl Physiol* 2001;91(5):2190-2198.
 46. Nagao M, Murase K, Ichiki T, Sakai S, Yasuhara Y, Ikezoe J. Quantitative analysis of technegas SPECT: evaluation of regional severity of emphysema. *J Nucl Med* 2000;41(4):590-595.
 47. Petersson J, Sanchez-Crespo A, Rohdin M, Montmerle S, Nyren S, Jacobsson H, Larsson SA, Lindahl SG, Linnarsson D, Glenny RW, Mure M. Physiological evaluation of a new quantitative SPECT method measuring regional ventilation and perfusion. *J Appl Physiol* 2004;96(3):1127-1136.
 48. Rhodes CG, Hughes JM. Pulmonary studies using positron emission tomography. *Eur Respir J* 1995;8(6):1001-1017.
 49. Senda M, Murata K, Itoh H, Yonekura Y, Torizuka K. Quantitative evaluation of regional pulmonary ventilation using PET and nitrogen-13 gas. *J Nucl Med* 1986;27(2):268-273.
 50. Rhodes CG, Valind SO, Brudin LH, Wollmer PE, Jones T, Hughes JM. Quantification of regional V/Q ratios in humans by use of PET. I. Theory. *J Appl Physiol* (1985) 1989;66(4):1896-1904.

51. Vidal Melo MF, Layfield D, Harris RS, O'Neill K, Musch G, Richter T, Winkler T, Fischman AJ, Venegas JG. Quantification of regional ventilation-perfusion ratios with PET. *J Nucl Med* 2003;44(12):1982-1991.
52. Musch G, Venegas JG. Positron emission tomography imaging of regional pulmonary perfusion and ventilation. *Proc Am Thorac Soc* 2005;2(6):522-527, 508-529.
53. Vidal Melo MF, Harris RS, Layfield D, Musch G, Venegas JG. Changes in regional ventilation after autologous blood clot pulmonary embolism. *Anesthesiology* 2002;97(3):671-681.
54. Stabin MG, Tagesson M, Thomas SR, Ljungberg M, Strand SE. Radiation dosimetry in nuclear medicine. *Appl Radiat Isot* 1999;50(1):73-87.
55. Ruth T. Accelerating production of medical isotopes. *Nature* 2009;457(7229):536-537.
56. Lauterbur PC. Image Formation by Induced Local Interactions - Examples Employing Nuclear Magnetic-Resonance. *Nature* 1973;242(5394):190-191.
57. Mills GH, Wild JM, Eberle B, Van Beek EJ. Functional magnetic resonance imaging of the lung. *Br J Anaesth* 2003;91(1):16-30.
58. Bieri O. Ultra-fast steady state free precession and its application to in vivo H morphological and functional lung imaging at 1.5 tesla. *Magn Reson Med* 2013;70:657-663.
59. Johnson KM, Fain SB, Schiebler ML, Nagle S. Optimized 3D ultrashort echo time pulmonary MRI. *Magn Reson Med* 2013;70(5):1241-1250.
60. Weiger M, Wu M, Wurnig MC, Kenkel D, Jungraithmayr W, Boss A, Pruessmann KP. Rapid and robust pulmonary proton ZTE imaging in the mouse. *NMR Biomed* 2014;27(9):1129-1134.
61. Gibiino F, Sacolick L, Menini A, Landini L, Wiesinger F. Free-breathing, zero-TE MR lung imaging. *Magn Reson Mater Phy* 2014;DOI: 10.1007/s10334-014-0459-y.
62. Dournes G, Grodzki D, Macey J, Girodet PO, Fayon M, Chateil JF, Montaudon M, Berger P, Laurent F. Quiet Submillimeter MR Imaging of the Lung Is Feasible with a PETRA Sequence at 1.5 T. *Radiology* 2015:141655.
63. Togao O, Tsuji R, Ohno Y, Dimitrov I, Takahashi M. Ultrashort echo time (UTE) MRI of the lung: assessment of tissue density in the lung parenchyma. *Magn Reson Med* 2010;64(5):1491-1498.

64. Ma W, Sheikh K, Svenningsen S, Pike D, Guo F, Etemad-Rezai R, Leipsic J, Coxson HO, McCormack DG, Parraga G. Ultra-short echo-time pulmonary MRI: Evaluation and reproducibility in COPD subjects with and without bronchiectasis. *J Magn Reson Imaging* 2014.
65. Ohno Y, Hatabu H, Takenaka D, Adachi S, Van Cauteren M, Sugimura K. Oxygen-enhanced MR ventilation imaging of the lung: preliminary clinical experience in 25 subjects. *Am J Roentgenol* 2001;177(1):185-194.
66. Edelman RR, Hatabu H, Tadamura E, Li W, Prasad PV. Noninvasive assessment of regional ventilation in the human lung using oxygen-enhanced magnetic resonance imaging. *Nat Med* 1996;2(11):1236-1239.
67. Chen Q, Jakob PM, Griswold MA, Levin DL, Hatabu H, Edelman RR. Oxygen enhanced MR ventilation imaging of the lung. *Magn Reson Mater Phy* 1998;7(3):153-161.
68. Sa RC, Cronin MV, Henderson AC, Holverda S, Theilmann RJ, Arai TJ, Dubowitz DJ, Hopkins SR, Buxton RB, Prisk GK. Vertical distribution of specific ventilation in normal supine humans measured by oxygen-enhanced proton MRI. *J Appl Physiol* 2010;109(6):1950-1959.
69. Henderson AC, Sa RC, Theilmann RJ, Buxton RB, Prisk GK, Hopkins SR. The gravitational distribution of ventilation-perfusion ratio is more uniform in prone than supine posture in the normal human lung. *J Appl Physiol* 2013;115(3):313-324.
70. Jakob PM, Wang T, Schultz G, Hebestreit H, Hebestreit A, Hahn D. Assessment of human pulmonary function using oxygen-enhanced T(1) imaging in patients with cystic fibrosis. *Magn Reson Med* 2004;51(5):1009-1016.
71. Kruger SJ, Fain SB, Johnson KM, Cadman RV, Nagle SK. Oxygen-enhanced 3D radial ultrashort echo time magnetic resonance imaging in the healthy human lung. *NMR Biomed* 2014.
72. Bauman G, Puderbach M, Deimling M, Jellus V, Ched'hotel C, Dinkel J, Hintze C, Kauczor HU, Schad LR. Non-contrast-enhanced perfusion and ventilation assessment of the human lung by means of fourier decomposition in proton MRI. *Magn Reson Med* 2009;62(3):656-664.
73. Lederlin M, Bauman G, Eichinger M, Dinkel J, Brault M, Biederer J, Puderbach M. Functional MRI using Fourier decomposition of lung signal: reproducibility of ventilation- and perfusion-weighted imaging in healthy volunteers. *Eur J Radiol* 2013;82(6):1015-1022.
74. Bauman G, Lutzen U, Ullrich M, Gaass T, Dinkel J, Elke G, Meybohm P, Frerichs I, Hoffmann B, Borggreffe J, Knuth HC, Schupp J, Prum H, Eichinger M, Puderbach M, Biederer J, Hintze C. Pulmonary functional imaging: qualitative

- comparison of Fourier decomposition MR imaging with SPECT/CT in porcine lung. *Radiology* 2011;260(2):551-559.
75. Bauman G, Scholz A, Rivoire J, Terekhov M, Friedrich J, de Oliveira A, Semmler W, Schreiber LM, Puderbach M. Lung ventilation- and perfusion-weighted Fourier decomposition magnetic resonance imaging: in vivo validation with hyperpolarized ^3He and dynamic contrast-enhanced MRI. *Magn Reson Med* 2013;69(1):229-237.
 76. Capaldi DP, Sheikh K, Guo F, Svenningsen S, Etemad-Rezai R, Coxson HO, Leipsic JA, McCormack DG, Parraga G. Free-breathing Pulmonary (^1H) and Hyperpolarized (^3He) MRI: Comparison in COPD and Bronchiectasis. *Acad Radiol* 2015;22(3):320-329.
 77. Bauman G, Pusterla O, Bieri O. Ultra-fast Steady-State Free Precession Pulse Sequence for Fourier Decomposition Pulmonary MRI. *Magn Reson Med* 2015.
 78. Albert MS, Cates GD, Driehuys B, Happer W, Saam B, Springer CS, Jr., Wishnia A. Biological magnetic resonance imaging using laser-polarized ^{129}Xe . *Nature* 1994;370(6486):199-201.
 79. Couch MJ, Blasiak B, Tomanek B, Ouriadov AV, Fox MS, Dowhos KM, Albert MS. Hyperpolarized and Inert Gas MRI: The Future. *Mol Imaging Biol* 2015;17(2):149-162.
 80. Couch MJ, Ouriadov A, Santyr GE. Regional ventilation mapping of the rat lung using hyperpolarized ^{129}Xe magnetic resonance imaging. *Magn Reson Med* 2012;68(5):1623-1631.
 81. Thomas AC, Potts EN, Chen BT, Slipetz DM, Foster WM, Driehuys B. A robust protocol for regional evaluation of methacholine challenge in mouse models of allergic asthma using hyperpolarized ^3He MRI. *NMR Biomed* 2009;22(5):502-515.
 82. Emami K, Kadlecsek SJ, Woodburn JM, Zhu J, Yu J, Vahdat V, Pickup S, Ishii M, Rizi RR. Improved technique for measurement of regional fractional ventilation by hyperpolarized ^3He MRI. *Magn Reson Med* 2010;63(1):137-150.
 83. Parraga G, Ouriadov A, Evans A, McKay S, Lam WW, Fenster A, Etemad-Rezai R, McCormack D, Santyr G. Hyperpolarized ^3He ventilation defects and apparent diffusion coefficients in chronic obstructive pulmonary disease: preliminary results at 3.0 Tesla. *Invest Radiol* 2007;42(6):384-391.
 84. Wild JM, Fischele S, Woodhouse N, Paley MN, Kasuboski L, van Beek EJ. 3D volume-localized pO_2 measurement in the human lung with ^3He MRI. *Magn Reson Med* 2005;53(5):1055-1064.

85. Woods JC, Choong CK, Yablonskiy DA, Bentley J, Wong J, Pierce JA, Cooper JD, Macklem PT, Conradi MS, Hogg JC. Hyperpolarized ³He diffusion MRI and histology in pulmonary emphysema. *Magn Reson Med* 2006;56(6):1293-1300.
86. Cleveland ZI, Cofer GP, Metz G, Beaver D, Nouls J, Kaushik SS, Kraft M, Wolber J, Kelly KT, McAdams HP, Driehuys B. Hyperpolarized Xe MR imaging of alveolar gas uptake in humans. *PLoS One* 2010;5(8):e12192.
87. Tustison NJ, Altes TA, Song G, de Lange EE, Mugler JP, 3rd, Gee JC. Feature analysis of hyperpolarized helium-3 pulmonary MRI: a study of asthmatics versus nonasthmatics. *Magn Reson Med* 2010;63(6):1448-1455.
88. Moller HE, Chen XJ, Saam B, Hagspiel KD, Johnson GA, Altes TA, de Lange EE, Kauczor HU. MRI of the lungs using hyperpolarized noble gases. *Magn Reson Med* 2002;47(6):1029-1051.
89. Johnson GA, Cates G, Chen XJ, Cofer GP, Driehuys B, Happer W, Hedlund LW, Saam B, Shattuck MD, Swartz J. Dynamics of magnetization in hyperpolarized gas MRI of the lung. *Magn Reson Med* 1997;38(1):66-71.
90. Walker TG, Happer W. Spin-exchange optical pumping of noble-gas nuclei. *Rev Mod Phys* 1997;69(2):629-642.
91. Comment A, Jannin S, Hyacinthe JN, Mieville P, Sarkar R, Ahuja P, Vasos PR, Montet X, Lazeyras F, Vallee JP, Hautle P, Konter JA, van den Brandt B, Ansermet JP, Gruetter R, Bodenhausen G. Hyperpolarizing Gases via Dynamic Nuclear Polarization and Sublimation. *Phys Rev Lett* 2010;105(1):018104.
92. Suchanek K, Cieslar K, Olejniczak Z, Palasz T, Suchanek M, Dohnalik T. Hyperpolarized He-3 gas production by metastability exchange optical pumping for magnetic resonance imaging. *Optica Applicata* 2005;35(2):263-276.
93. Mathew L, Evans A, Ouriadov A, Etemad-Rezai R, Fogel R, Santyr G, McCormack DG, Parraga G. Hyperpolarized ³He magnetic resonance imaging of chronic obstructive pulmonary disease: reproducibility at 3.0 tesla. *Acad Radiol* 2008;15(10):1298-1311.
94. Fain SB, Panth SR, Evans MD, Wentland AL, Holmes JH, Korosec FR, O'Brien MJ, Fountaine H, Grist TM. Early emphysematous changes in asymptomatic smokers: detection with ³He MR imaging. *Radiology* 2006;239(3):875-883.
95. Fain SB, Gonzalez-Fernandez G, Peterson ET, Evans MD, Sorkness RL, Jarjour NN, Busse WW, Kuhlman JE. Evaluation of structure-function relationships in asthma using multidetector CT and hyperpolarized He-3 MRI. *Acad Radiol* 2008;15(6):753-762.
96. Holmes JH, O'Halloran RL, Brodsky EK, Bley TA, Francois CJ, Velikina JV, Sorkness RL, Busse WW, Fain SB. Three-dimensional imaging of ventilation

- dynamics in asthmatics using multiecho projection acquisition with constrained reconstruction. *Magn Reson Med* 2009;62(6):1543-1556.
97. de Lange EE, Altes TA, Patrie JT, Battiston JJ, Juersivich AP, Mugler JP, 3rd, Platts-Mills TA. Changes in regional airflow obstruction over time in the lungs of patients with asthma: evaluation with ^3He MR imaging. *Radiology* 2009;250(2):567-575.
 98. Sun Y, O'Sullivan BP, Roche JP, Walvick R, Reno A, Baker D, Mansour JK, Albert MS. Using hyperpolarized ^3He MRI to evaluate treatment efficacy in cystic fibrosis patients. *J Magn Reson Imaging* 2011;34(5):1206-1211.
 99. O'Sullivan B, Couch M, Roche JP, Walvick R, Zheng S, Baker D, Johnson M, Botfield M, Albert MS. Assessment of repeatability of hyperpolarized gas MR ventilation functional imaging in cystic fibrosis. *Acad Radiol* 2014;21(12):1524-1529.
 100. Couch MJ, Ball IK, Li T, Fox MS, Ouriadov AV, Biman B, Albert MS. Inert fluorinated gas MRI: a new pulmonary imaging modality. *NMR Biomed* 2014;27(12):1525-1534.
 101. Kirby M, Heydarian M, Svenningsen S, Wheatley A, McCormack DG, Etemad-Rezai R, Parraga G. Hyperpolarized ^3He magnetic resonance functional imaging semiautomated segmentation. *Acad Radiol* 2012;19(2):141-152.
 102. Mathew L, Kirby M, Etemad-Rezai R, Wheatley A, McCormack DG, Parraga G. Hyperpolarized (^3He) magnetic resonance imaging: preliminary evaluation of phenotyping potential in chronic obstructive pulmonary disease. *Eur J Radiol* 2011;79(1):140-146.
 103. Evans A, McCormack DG, Santyr G, Parraga G. Mapping and quantifying hyperpolarized ^3He magnetic resonance imaging apparent diffusion coefficient gradients. *J Appl Physiol* 2008;105(2):693-699.
 104. Kirby M, Svenningsen S, Kanhere N, Owrangi A, Wheatley A, Coxson HO, Santyr GE, Paterson NA, McCormack DG, Parraga G. Pulmonary ventilation visualized using hyperpolarized helium-3 and xenon-129 magnetic resonance imaging: differences in COPD and relationship to emphysema. *J Appl Physiol* 2013;114(6):707-715.
 105. Ouriadov A, Farag A, Kirby M, McCormack DG, Parraga G, Santyr GE. Lung morphometry using hyperpolarized (^{129}Xe) apparent diffusion coefficient anisotropy in chronic obstructive pulmonary disease. *Magn Reson Med* 2013;70(6):1699-1706.
 106. Yu J, Law M, Kadlecsek S, Emami K, Ishii M, Stephen M, Woodburn JM, Vahdat V, Rizi RR. Simultaneous measurement of pulmonary partial pressure of oxygen

and apparent diffusion coefficient by hyperpolarized ^3He MRI. *Magn Reson Med* 2009;61(5):1015-1021.

107. Hamedani H, Kadlecck SJ, Emami K, Kuzma NN, Xu Y, Xin Y, Mongkolwisetwara P, Rajaei J, Barulic A, Wilson Miller G, Rossman M, Ishii M, Rizi RR. A multislice single breath-hold scheme for imaging alveolar oxygen tension in humans. *Magn Reson Med* 2012;67(5):1332-1345.
108. Deninger AJ, Eberle B, Ebert M, Grossmann T, Heil W, Kauczor H, Lauer L, Markstaller K, Otten E, Schmiedeskamp J, Schreiber W, Surkau R, Thelen M, Weiler N. Quantification of regional intrapulmonary oxygen partial pressure evolution during apnea by (^3He) MRI. *J Magn Reson* 1999;141(2):207-216.
109. Rizi RR, Baumgardner JE, Ishii M, Spector ZZ, Edvinsson JM, Jalali A, Yu J, Itkin M, Lipson DA, Gefter W. Determination of regional VA/Q by hyperpolarized ^3He MRI. *Magn Reson Med* 2004;52(1):65-72.
110. Heidelberg E, Lauterbur PC. Gas Phase ^{19}F -NMR Zeugmatography: A New Approach to Lung Ventilation Imaging. In Proc 1st Annual Meeting Society of Magnetic Resonance in Medicine, 1982. p 70-71.
111. Rinck PA, Petersen SB, Lauterbur PC. NMR-Imaging von fluorhaltigen Substanzen. ^{19}F Fluor-Ventilations- und -Perfusionsdarstellungen. *Fortschr Röntgenstr* 1984;140(3):239-243.
112. Rinck PA, Peterson SB, Heidelberg E, Acuff V, Reinders J, Bernardo ML, Hedges LK, Lauterbur PC. NMR ventilation imaging of the lungs using perfluorinated gases. *Magn Reson Med* 1984;1(2):237-237.
113. Kuethe DO, Caprihan A, Fukushima E, Waggoner RA. Imaging lungs using inert fluorinated gases. *Magn Reson Med* 1998;39(1):85-88.
114. Wolf U, Scholz A, Terekhov M, Muennemann K, Kreitner K, Werner C, Dueber C, Schreiber WG. Fluorine-19 MRI of the lung: first human experiment. In Proc 16th Annual Meeting of ISMRM, 2008. p 3207.
115. Couch MJ, Ball IK, Li T, Fox MS, Littlefield SL, Biman B, Albert MS. Pulmonary ultrashort echo time ^{19}F MR imaging with inhaled fluorinated gas mixtures in healthy volunteers: feasibility. *Radiology* 2013;269(3):903-909.
116. Halaweish AF, Moon RE, Foster WM, Soher BJ, McAdams HP, MacFall JR, Ainslie MD, MacIntyre NR, Charles HC. Perfluoropropane gas as a magnetic resonance lung imaging contrast agent in humans. *Chest* 2013;144(4):1300-1310.
117. Halaweish AF, Charles HC. Physiorack: An integrated MRI safe/conditional, Gas delivery, respiratory gating, and subject monitoring solution for structural and functional assessments of pulmonary function. *J Magn Reson Imaging* 2014;39(3):735-741.

118. Charles C, Moon RE, MacIntyre NR, Halaweish AF, Choudhury KR, Ainslie MD, Womack SJ, Mcadams HP, Foster WM. Cardio-Respiratory Tolerability of Perfluoropropane-Enhanced MRI of Pulmonary Ventilation. *Am Respir Crit Care Med* 2015;191:A3509.
119. Haacke EM, Brown RW, Thompson MR, Venkatesan R. *Magnetic Resonance Imaging: Physical Principles and Pulse Sequence Design*. New York: John Wiley & Sons; 1999.
120. Nishimura DG. *Principles of Magnetic Resonance Imaging*. lulu.com; 2010.
121. Meersmann T, Pavlovskaya GE. Beyond Spin $I = 1/2$; Hyperpolarized ^{131}Xe and ^{83}Kr Magnetic Resonance In: Meersmann T, Brunner E, editors. *Hyperpolarized Xenon-129 Magnetic Resonance: Concepts, Production, Techniques and Applications*. Cambridge, UK: Royal Society of Chemistry; 2015.
122. Nuclear Spins, Moments, and Other Data Related to NMR Spectroscopy. *CRC Handbook of Chemistry and Physics*, 95th ed, 2014-2015. <http://www.hbcernetbase.com>.
123. Santyr GE, Lam WW, Parra-Robles JM, Taves TM, Ouriadov AV. Hyperpolarized noble gas magnetic resonance imaging of the animal lung: Approaches and applications. *J Appl Phys* 2009;105:102004.
124. Zhao L, Mulkern R, Tseng CH, Williamson D, Patz S, Kraft R, Walsworth RL, Jolesz FA, Albert MS. Gradient-echo imaging considerations for hyperpolarized Xe-129 MR. *J Magn Reson Ser B* 1996;113(2):179-183.
125. Robson MD, Gatehouse PD, Bydder M, Bydder GM. Magnetic resonance: an introduction to ultrashort TE (UTE) imaging. *J Comput Assist Tomogr* 2003;27(6):825-846.
126. Ouriadov AV, Fox MS, Couch MJ, Li T, Ball IK, Albert MS. In vivo regional ventilation mapping using fluorinated gas MRI with an x-centric FGRE method. *Magn Reson Med* 2015;74(2):550-557.
127. Kruger SJ, Nagle SK, Couch MJ, Ohno Y, Albert M, Fain SB. Functional imaging of the lungs with gas agents. *J Magn Reson Imaging* 2015;DOI:10.1002/jmri.25002.
128. Sarkar K, Katiyar A, Jain P. Growth and dissolution of an encapsulated contrast microbubble: effects of encapsulation permeability. *Ultrasound Med Biol* 2009;35(8):1385-1396.
129. Abdeen N, Cross A, Cron G, White S, Rand T, Miller D, Santyr G. Measurement of xenon diffusing capacity in the rat lung by hyperpolarized ^{129}Xe MRI and dynamic spectroscopy in a single breath-hold. *Magn Reson Med* 2006;56(2):255-264.

130. Driehuys B, Cofer GP, Pollaro J, Mackel JB, Hedlund LW, Johnson GA. Imaging alveolar-capillary gas transfer using hyperpolarized ^{129}Xe MRI. *Proc Natl Acad Sci U S A* 2006;103(48):18278-18283.
131. Fox MS, Ouriadov A, Thind K, Hegarty E, Wong E, Hope A, Santyr GE. Detection of radiation induced lung injury in rats using dynamic hyperpolarized (^{129}Xe) magnetic resonance spectroscopy. *Med Phys* 2014;41(7):072302.
132. Qing K, Ruppert K, Jiang Y, Mata JF, Miller GW, Shim YM, Wang C, Ruset IC, Hersman FW, Altes TA, Mugler JP, 3rd. Regional mapping of gas uptake by blood and tissue in the human lung using hyperpolarized xenon-129 MRI. *J Magn Reson Imaging* 2014;39(2):346-359.
133. Kaushik SS, Robertson SH, Freeman MS, He M, Kelly KT, Roos JE, Rackley CR, Foster WM, McAdams HP, Driehuys B. Single-breath clinical imaging of hyperpolarized Xe in the airspaces, barrier, and red blood cells using an interleaved 3D radial 1-point Dixon acquisition. *Magn Reson Med* 2015.
134. Mazzanti ML, Walvick RP, Zhou X, Sun Y, Shah N, Mansour J, Gereige J, Albert MS. Distribution of hyperpolarized xenon in the brain following sensory stimulation: preliminary MRI findings. *PLoS One* 2011;6(7):e21607.
135. Zhou X, Sun Y, Mazzanti M, Henninger N, Mansour J, Fisher M, Albert M. MRI of stroke using hyperpolarized ^{129}Xe . *NMR Biomed* 2010;24(2):170-175.
136. Luttrupp HH, Thomasson R, Dahm S, Persson J, Werner O. Clinical experience with minimal flow xenon anesthesia. *Acta Anaesthesiol Scand* 1994;38(2):121-125.
137. Driehuys B, Martinez-Jimenez S, Cleveland ZI, Metz GM, Beaver DM, Nouls JC, Kaushik SS, Firszt R, Willis C, Kelly KT, Wolber J, Kraft M, McAdams HP. Chronic obstructive pulmonary disease: safety and tolerability of hyperpolarized ^{129}Xe MR imaging in healthy volunteers and patients. *Radiology* 2012;262(1):279-289.
138. Wagner PD. The multiple inert gas elimination technique (MIGET). *Intens Care Med* 2008;34(6):994-1001.
139. Alzaraa A, Gravante G, Chung WY, Al-Leswas D, Bruno M, Dennison AR, Lloyd DM. Targeted microbubbles in the experimental and clinical setting. *Am J Surg* 2012;204(3):355-366.
140. Kuethe DO, Caprihan A, Gach HM, Lowe IJ, Fukushima E. Imaging obstructed ventilation with NMR using inert fluorinated gases. *J Appl Physiol* 2000;88(6):2279-2286.

141. Leawoods JC, Yablonskiy DA, Saam B, Gierada DS, Conradi MS. Hyperpolarized He-3 gas production and MR imaging of the lung. *Concept Magnetic Res* 2001;13(5):277-293.
142. Mugler JP, 3rd, Altes TA. Hyperpolarized ^{129}Xe MRI of the human lung. *J Magn Reson Imaging* 2013;37(2):313-331.
143. Chang YV, Conradi MS. Relaxation and diffusion of perfluorocarbon gas mixtures with oxygen for lung MRI. *J Magn Reson* 2006;181(2):191-198.
144. Halaweish AF, Foster WM, Moon RE, MacIntyre NR, MacFall JR, Charles HC. Dynamics of Pulmonary Ventilation Distribution at Steady State via ^{19}F -Enhanced MRI: Initial Experiences and Future Developments. In *Proc 21st Annual Meeting of ISMRM*, 2013. p 4111.
145. Charles C, Soher B, Halaweish AF. Modeling of the Spatio-Temporal Distribution of Pulmonary Ventilation via Perfluoropropane Gas Enhanced MRI. *Am Respir Crit Care Med* 2015:A2125.
146. Charles HC, MacIntyre NR, Moon R, Foster WM, McAdams HP, Ainslie M. In-Vivo Visualization Of Slow To Fast Filling Compartments In Human Lungs Using ^{19}F MRI Of Perfluorinated Gases Mixed With Oxygen. *Am Respir Crit Care Med* 2014;189:A4348.
147. Horn FC, Deppe MH, Marshall H, Parra-Robles J, Wild JM. Quantification of regional fractional ventilation in human subjects by measurement of hyperpolarized ^3He washout with 2D and 3D MRI. *J Appl Physiol* 2014;116(2):129-139.
148. Hamedani H, Kadlecek S, Han B, Emami K, Xin Y, Ishii M, Rossman M, Rizi R. A simultaneous multi-breath scheme for measurement of ADC, $p\text{AO}_2$ and fractional ventilation using ^3He MRI in human. In *Proc 21st Annual Meeting of ISMRM*, 2013. p 1468.
149. Woods JC. Mine the moon for ^3He MRI? Not yet. *J Appl Physiol* 2013;114(6):705-706.
150. Kouzes RT, Ely JH, Erikson LE, Kernan WJ, Lintereur AT, Siciliano ER, Stephens DL, Stromswold DC, Van Ginhoven RM, Woodring ML. Neutron detection alternatives to He-3 for national security applications. *Nucl Instrum Meth A* 2010;623(3):1035-1045.
151. Stewart NJ, Norquay G, Griffiths PD, Wild JM. Feasibility of human lung ventilation imaging using highly polarized naturally abundant xenon and optimized three-dimensional steady-state free precession. *Magn Reson Med* 2015.
152. Hersman FW, Ruset IC, Ketel S, Muradian I, Covrig SD, Distelbrink J, Porter W, Watt D, Ketel J, Brackett J, Hope A, Patz S. Large production system for

- hyperpolarized ^{129}Xe for human lung imaging studies. *Acad Radiol* 2008;15(6):683-692.
153. Nikolaou P, Coffey AM, Walkup LL, Gust BM, Whiting N, Newton H, Barcus S, Muradyan I, Dabaghyan M, Moroz GD, Rosen MS, Patz S, Barlow MJ, Chekmenev EY, Goodson BM. Near-unity nuclear polarization with an open-source ^{129}Xe hyperpolarizer for NMR and MRI. *Proc Natl Acad Sci U S A* 2013;110(35):14150-14155.
 154. Nikolaou P, Coffey AM, Walkup LL, Gust BM, LaPierre CD, Koehnemann E, Barlow MJ, Rosen MS, Goodson BM, Chekmenev EY. A 3D-printed high power nuclear spin polarizer. *J Am Chem Soc* 2014;136(4):1636-1642.
 155. Christophorou LG, Olthoff JK, Van Brunt RJ. Sulfur hexafluoride and the electric power industry. *Electrical Insulation Magazine, IEEE* 1997;13(5):20-24.
 156. Khalil MAK, Rasmussen RA, Culbertson JA, Prins JM, Grimsrud EP, Shearer MJ. Atmospheric perfluorocarbons. *Environ Sci Technol* 2003;37(19):4358-4361.

Chapter 2

Pulmonary Ultrashort Echo Time ^{19}F MR Imaging with Inhaled Fluorinated Gas Mixtures in Healthy Volunteers: Feasibility*

2.1 Abstract

Purpose: The purpose of this study was to perform static breath-hold fluorine-19 (^{19}F) 3D ultra-short echo time (UTE) magnetic resonance imaging (MRI) of the lungs in healthy volunteers using a mixture 79% perfluoropropane (PFP) and 21% O_2 .

Methods: This study protocol was approved by the local research ethics board and by Health Canada. All subjects provided written informed consent prior to their participation in this study. Ten healthy volunteers underwent MR imaging at 3.0 T. ^{19}F 3D UTE images were acquired during a 15 second breath-hold, following one of two breathing protocols: (A) a 1 L inhalation of a mixture of 79% perfluoropropane (PFP) and 21% O_2 , or (B) continuous breathing from a 5 L bag of a mixture of 79% PFP and 21% O_2 , followed by a 1 L inhalation of the same PFP/ O_2 mixture from a separate bag, and subsequent breath-hold. The signal-to-noise ratio (SNR) was measured in the three most central image slices, and compared between breathing protocols using an unpaired t-test.

* This chapter was originally published in Radiology, 2013; 269: 903–909, DOI:10.1148/radiol.13130609, and was co-authored by Marcus J. Couch, Iain K. Ball, Tao Li, Matthew S. Fox, Shalyn L. Littlefield, Birubi Biman, and Mitchell S. Albert.

Results: Overall, the SNR was significantly greater for breathing protocol B (continuous breathing) compared to breathing protocol A (single breath) ($p = 0.018$). The mean SNR (\pm standard deviation) was 18 ± 6 and 32 ± 6 , for images acquired using breathing protocols A and B, respectively. Breathing protocol B improves SNR by washing out the air from the lungs and increasing the PFP concentration prior to ^{19}F imaging.

Conclusion: This feasibility study demonstrates the use of ^{19}F 3D UTE static breath-hold imaging of human lungs with inert fluorinated gases.

2.2 Introduction

Chronic respiratory diseases, such as asthma, chronic obstructive pulmonary disease (COPD) and cystic fibrosis are a significant global health care burden. COPD is currently the fourth leading cause of death in the United States (1), and there is a need in the medical community for functional imaging techniques that can provide regional data on lung function. Available modalities for the assessment of lung function include spirometry, nuclear medicine imaging using radio-isotopes, chest X-ray, computed tomography (CT) and conventional proton (^1H) magnetic resonance imaging (MRI) (2,3). Spirometry has the advantage of being low cost and widely available but provides only information on global lung function. Chest X-rays, nuclear medicine and CT all expose the patient to ionizing radiation.

^1H MRI cannot typically provide high quality images of the lungs due to the low tissue density, high magnetic susceptibility differences at air/tissue interfaces and respiratory motion. The image quality from ^1H MRI can be improved through the use of ultra-short echo time (UTE) pulse sequences, however, this technique can only obtain structural information (4). It is possible to obtain some functional information from the lungs using O_2 enhanced ^1H MRI (5), however, it is unclear whether the O_2 enhancement represents ventilation of the air spaces, since the signal change arises from protons interacting with O_2 dissolved in tissue (3). Hyperpolarized (HP) noble gas MRI, using helium-3 (^3He) and xenon-129 (^{129}Xe), is a non-invasive imaging technique that allows for the direct measurement of lung ventilation, gas exchange, and lung microstructure (6,7). Unfortunately, ^3He is an extremely scarce and expensive isotope. Although ^{129}Xe is more plentiful and less expensive, both ^3He and ^{129}Xe require a polarizer to prepare and process the gases.

An attractive alternative to HP noble gas MRI is functional MRI using inert fluorinated gases, such as sulfur hexafluoride (SF_6), hexafluoroethane (C_2F_6), and perfluoropropane (C_3F_8 or PFP) as inhaled signal sources for MRI. These gases offer the advantages of being nontoxic, abundant, and inexpensive compared to HP noble gases. Furthermore, inert fluorinated gases, due to the high gyromagnetic ratio of fluorine-19 (^{19}F) and short longitudinal relaxation times, do not need to be hyperpolarized prior to their use in MRI. This eliminates the need for an expensive polarizer. 3D inert fluorinated gas MRI was initially reported over 15 years ago, where it was used to acquire 3D images of rat lungs during continuous breathing of a mixture of C_2F_6 and O_2 (8). Investigators quickly saw

the potential for this technique to provide functional measurements in animal lungs, including wash-in/wash-out kinetics of pulmonary ventilation (9), volume measurements throughout the respiratory cycle (10), and the measurement of ventilation/perfusion ratios (11,12). Sub-second imaging has been demonstrated with SF₆ in pigs, which allows for fast and dynamic measurements of gas kinetics (13). Wash-in/wash-out kinetics of pulmonary ventilation agree well with respiratory gas analysis (14). Efforts have been made to perform diffusion-weighted imaging in rat lungs using inert fluorinated gas MRI (15,16), including a study of elastase-induced emphysema in rats (17). Diffusion measurements have also been performed in healthy and emphysematous excised human lungs (18,19).

Recently, Soher et al. demonstrated lung imaging using inert fluorinated gases in a single healthy human subject (20). 3D gradient echo imaging was performed following inhalation of PFP through a gas-delivery system. Although this was a promising development, the image quality was less than what can currently be achieved using HP noble gas MRI. There is a clear need to further develop and improve the image quality of MRI using inert fluorinated gases. Since inert fluorinated gases are known to have short T₂^{*} relaxation times (12), 3D UTE is expected to have a higher signal-to-noise ratio (SNR) than 3D gradient echo imaging. The purpose of this study was to perform static breath-hold ¹⁹F 3D UTE MRI of the lungs in healthy volunteers using a mixture 79% PFP and 21% O₂.

2.3 Methods

2.3.1 Subjects

This study protocol was approved by the local research ethics board and by Health Canada. All subjects provided written informed consent prior to their participation in this study. Ten healthy volunteers (8 female, 2 male) were enrolled with no history of chronic respiratory disease, and a smoking history of less than 10 pack-years. A pack-year was defined as the number of cigarette packs smoked per day multiplied by the number of years the individual smoked. The mean age of all subjects (\pm standard deviation) was 28 ± 11 years. Men had a mean age of 38.5 with a range of 20 to 57. Women had a mean age of 25.3 with a range of 21 to 29. Digital pulse oximetry was used to measure peripheral oxygen saturation (S_pO_2) for all subjects during scanning sessions (Veris, Medrad, Warrendale, PA).

2.3.2 Image Acquisition

Imaging was performed using a 3.0 T Philips Achieva scanner and a flexible wrap-around quadrature transmit/receive coil (Clinical MR Solutions, Brookfield, WI) tuned to the ^{19}F resonance frequency (120.15 MHz at 3.0 T). Since the resonance frequencies of ^{19}F and 1H are relatively close, the ^{19}F coil was actively proton blocked to allow for artifact-free 1H imaging while the subject was lying inside the ^{19}F coil. Active decoupling was achieved by using PIN diodes that are controlled with an external DC power supply. The PIN diodes are able to selectively control which components of the coil are turned on in

order to shift the resonance frequency of the coil away from the ^{19}F frequency during ^1H scanning (21,22). Conventional ^1H MRI was performed prior to ^{19}F MRI with subjects imaged during a 1 L breath-hold of air. ^1H images were acquired using a 2D multi-slice gradient echo acquisition, and were used as reference scans for planning 3D ^{19}F images.

Prior to ^{19}F imaging, the flip angle was calibrated for each participant. Due to differences in subject size (and hence different coil loading conditions), the RF power required to produce a given flip angle may vary slightly. To calibrate the flip angle, subjects inhaled a 1 L Tedlar bag (Jensen Inert Products, Coral Springs, FL) of a mixture of 79% PFP and 21% O_2 (Air Liquide, Plumsteadville, PA) and held their breath for 15 seconds. During this breath-hold, a series of whole-lung spectroscopic acquisitions were performed with increasing RF power (23). 20 FIDs were collected with the following settings: TR = 750 ms, TE = 0.83 ms, 2048 points, bandwidth = 8 kHz, starting flip angle = 10° , and flip angle spacing = 10° . Figure 2-1 shows an ideal ^{19}F flip angle calibration acquired in a fluorinated gas-filled phantom. As expected, the 90° RF pulse yields the maximum signal intensity, while the 180° RF pulse yields the minimum signal intensity. If the flip angle was overpowered, the curve in Figure 2-1 would shift to the left; conversely, the calibration curve would shift to the right if the flip angle was underpowered. Using this spectroscopic approach, the transmitter gain can be adjusted such that the maximum signal intensity occurs in the 90° bin, which ensures a correct calibration.

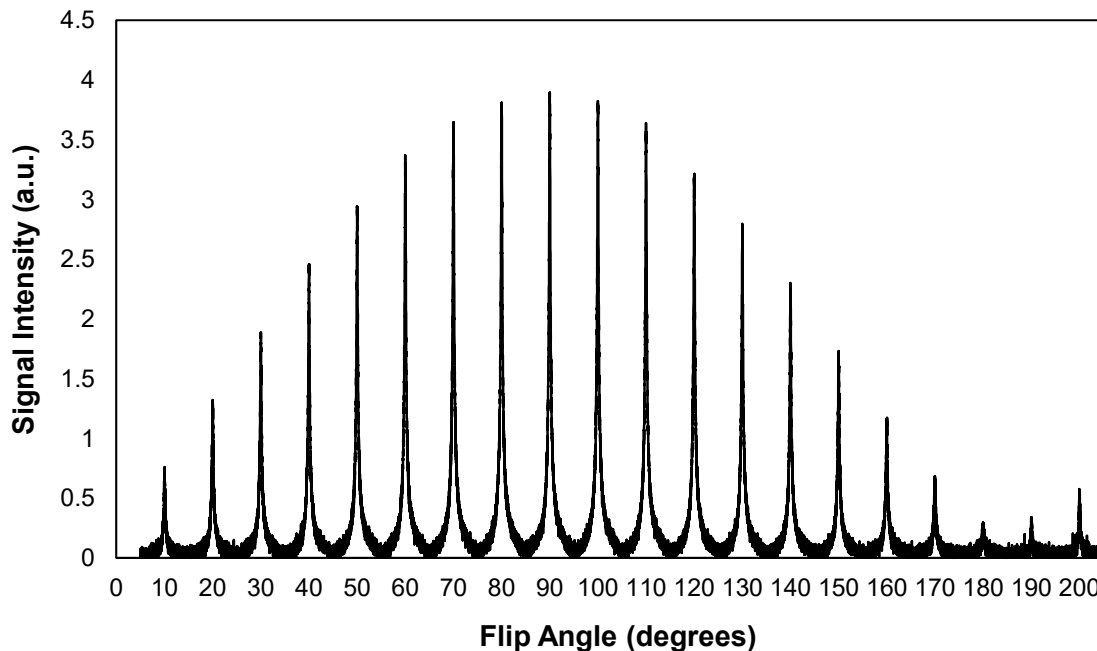


Figure 2-1: Ideal flip angle sweep consisting of 20 spectra with increasing flip angles. ^{19}F spectra were acquired in a fluorinated gas-filled phantom. As expected, a 90° RF pulse yields the highest possible signal intensity.

Following calibration, ^{19}F lung images were acquired following one of two breathing protocols: (A) a 1 L inhalation of a mixture of 79% PFP and 21% O_2 from a single Tedlar bag followed by a 15 s breath-hold, or (B) continuous breathing from a 5 L Tedlar bag of a mixture of 79% PFP and 21% O_2 , followed by a 1 L inhalation of the same PFP/ O_2 mixture from a separate Tedlar bag, and a 15 s breath-hold. Subjects were instructed to inhale a normal tidal volume of gas from the 5 L bag, and exhale around the tube, and to continue this procedure until the bag was empty. The second Tedlar bag filled with 1 L of gas allowed the subsequent image to be acquired at a reproducible lung inflation state.

^{19}F 3D UTE images were acquired with the following settings: TR = 20 ms, TE = 0.2 ms, matrix = 64 x 64, in-plane FOV = 450 x 450 mm², flip angle = 70° , non-selective excitation, and bandwidth = 140 Hz/pixel. For both breathing protocols, half echoes were

acquired at 750 different angles starting from the center of k-space. Due to scanner and hardware limitations, 0.2 ms was the shortest possible TE. The T_1 of PFP was measured to be 12.4 ms in the lungs at 3.0 T, which is close to previously reported *in vitro* T_1 values (24). Therefore, a flip angle of 70° was close to the Ernst angle (78.5°) for a TR of 20 ms. For breathing protocol A, 8 slices were reconstructed in the coronal or axial plane with a thickness of 22 mm, while in breathing protocol B, 12 slices were reconstructed in the coronal or axial plane with a thickness of 15 mm. The signal-to-noise ratio (SNR) was measured by finding the mean signal value from a rectangular region of interest (ROI) in the right lung, and dividing by the standard deviation of noise from a similar ROI and in the background. The SNR values from the two breathing protocols were compared using an unpaired t-test in Graphpad Prism (GraphPad Software, La Jolla, CA), and $p < 0.05$ was considered significant.

2.4 Results

Table 2-1 summarizes the subject demographics, oxygen saturation, and image SNR for all ^{19}F UTE acquisitions. SNR was measured from coronal images, and the error represents the standard deviation of SNR measurements in 3 central slices. For breathing protocol A, the mean SNR (\pm standard deviation) was 18 ± 6 , while for breathing protocol B, the mean SNR was 32 ± 6 . Overall, the SNR was significantly different for breathing protocols A and B ($p = 0.018$ by an unpaired t-test).

Table 2-1: Subject demographics, oxygen saturation, and SNR (\pm standard deviation) from all available coronal ^{19}F 3D UTE images. The breathing protocol used for each subject is indicated.

Subject	Sex	Age	Breathing Protocol	BMI (kg/m ²)	Resting S _p O ₂ (%)	Breath-hold S _p O ₂ (%)	Image SNR
1	f	26	A	18.90	99	96	22 \pm 3
2	m	20	A	18.62	99	94	18 \pm 2
3	f	29	A	19.03	99	98	11 \pm 1
4	f	27	A	21.45	99	93	21 \pm 2
5	f	21	A	19.63	99	95	27 \pm 2
6	f	23	A	18.16	99	96	11 \pm 1
7*	f	29	-	19.47	99	98	24 \pm 4
8	f	24	B	28.43	99	93	38 \pm 4
9	m	57	B	23.13	99	97	32 \pm 2
10	f	23	B	23.61	99	96	26 \pm 2

*For this subject only, the 1 L inhalation of the PFP/O₂ mixture was preceded by a 1 L washout from a separate Tedlar bag of the PFP/O₂ mixture.

Figure 2-2 shows eight slices from a ^{19}F 3D UTE lung image in the coronal plane that was acquired in subject #4. This static breath-hold image effectively visualizes the distribution of the PFP gas inside the lungs of the subject. This image was acquired using breathing protocol A, where a 15 s breath-hold followed a single 1 L inhalation of the PFP/O₂ mixture. The SNR in the centre slices was 21 \pm 2. Figure 2-3 shows eight slices of a ^{19}F 3D UTE lung image that was acquired in the axial plane from subject #5, also using breathing protocol A. In this case, the SNR in the centre slices was 30 \pm 6.

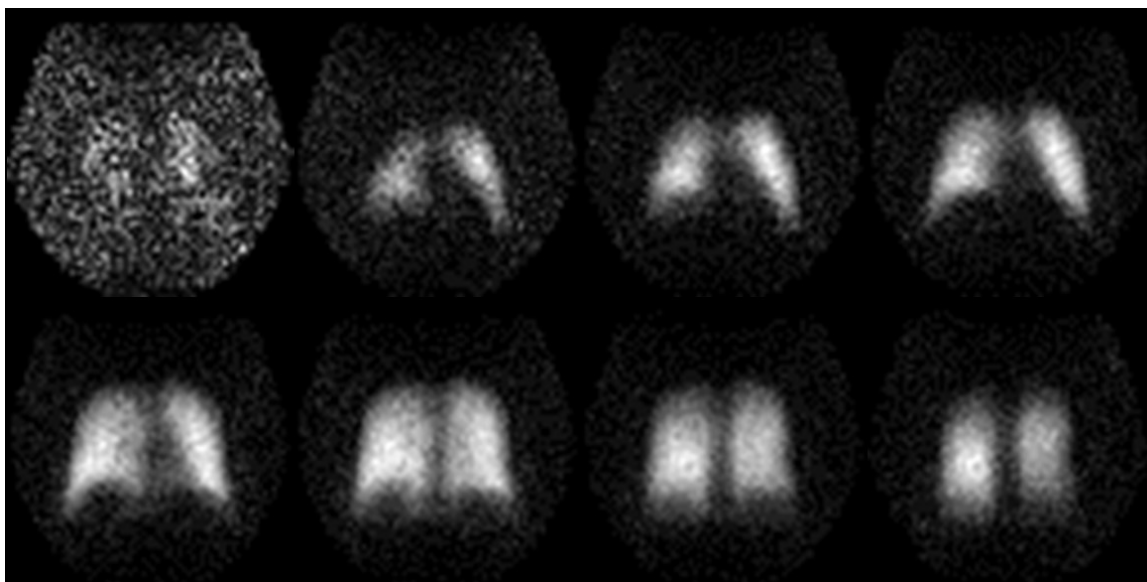


Figure 2-2: ^{19}F 3D UTE lung images acquired in the coronal plane from subject #4 during a 15 s breath-hold, following inhalation of a 1 L mixture of 79% PFP and 21% O_2 from a Tedlar bag. Images were reproduced with permission (25).

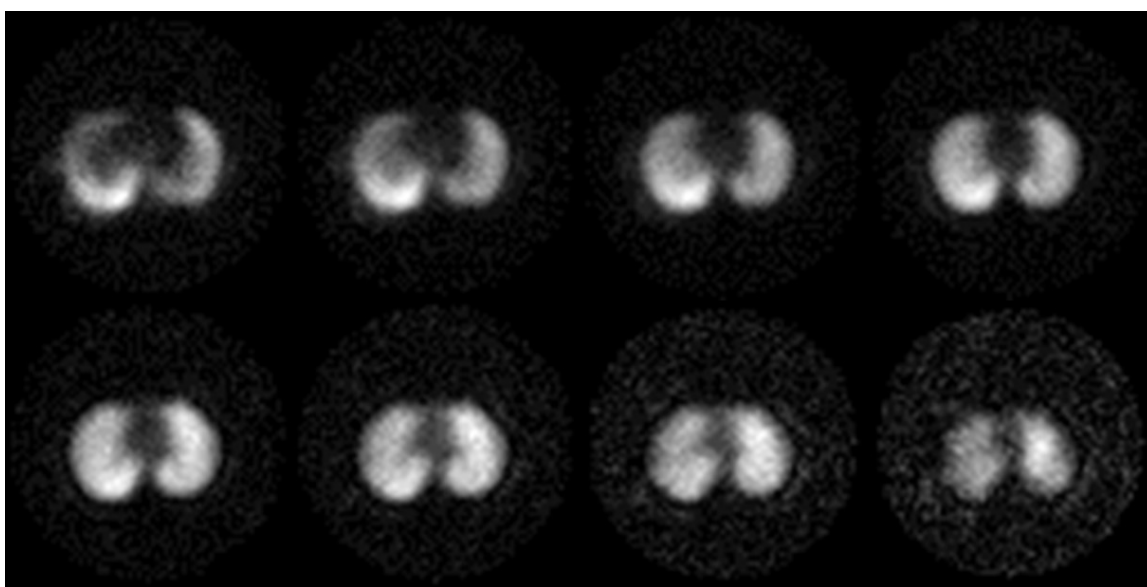


Figure 2-3: ^{19}F 3D UTE lung images acquired in the axial plane from subject #5 during a 15 s breath-hold, following inhalation of a 1 L mixture of 79% PFP and 21% O_2 from a Tedlar bag. Images were reproduced with permission (25).

Figure 2-4 shows 12 slices from a ^{19}F 3D UTE lung image in the coronal plane that was acquired during a 15 second breath-hold in subject #9 using breathing protocol B: continuous breathing from a 5 L Tedlar bag of the PFP/ O_2 mixture, followed by a 1 L inhalation of the PFP/ O_2 mixture from a separate Tedlar bag. There was sufficient signal in the lungs to increase the number of slices from 8 to 12, and decrease the slice thickness from 22 mm to 15 mm, while maintaining full lung coverage. The SNR in the centre slices of Figure 2-4 was 32 ± 2 .

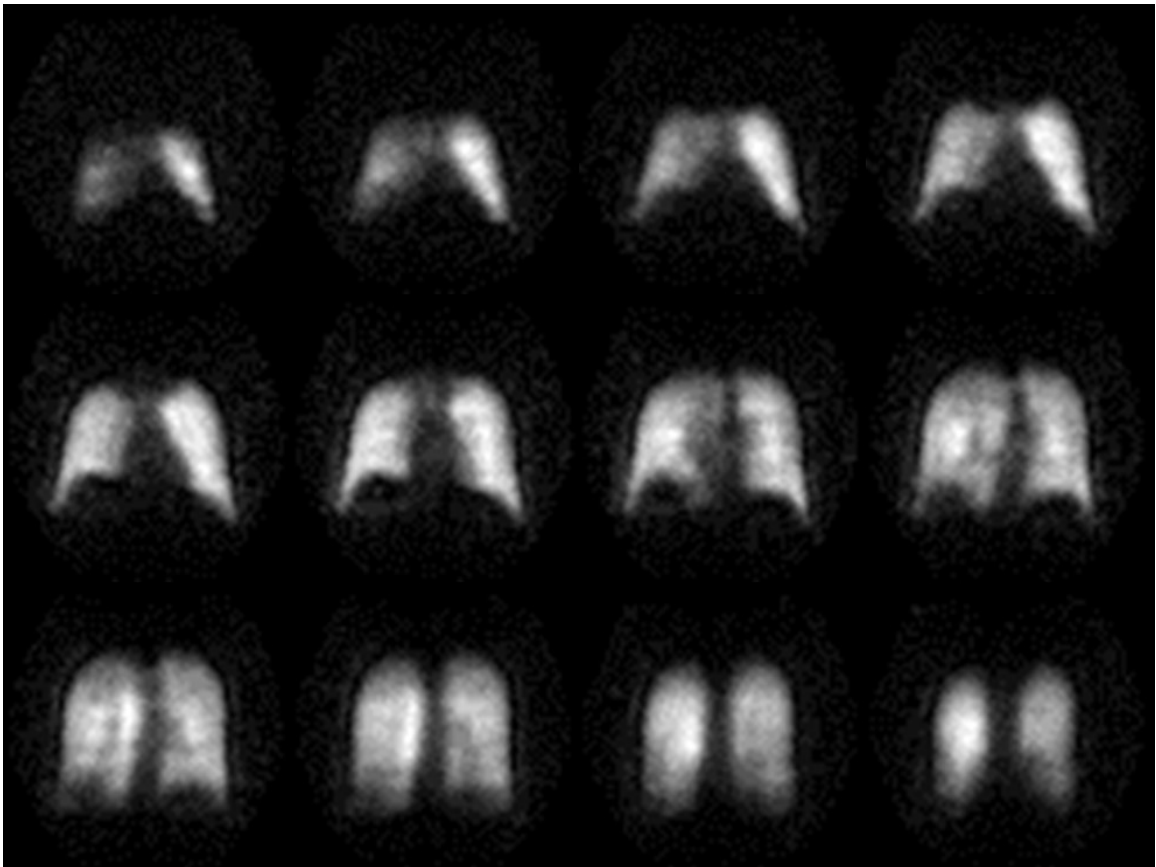


Figure 2-4: ^{19}F 3D UTE lung images acquired in the coronal plane from subject #9 during a 15 s breath-hold, following continuous breathing from a 5 L mixture of 79% PFP and 21% O_2 and a 1 L inhalation of the same mixture. Images were reproduced with permission (25).

Figure 2-5 shows 12 slices from a ^{19}F 3D UTE lung image in the axial plane that was acquired during a 15 second breath-hold in subject #8. Breathing protocol B was also used in Figure 2-5, and yielded an SNR in the center slices of 44 ± 4 .

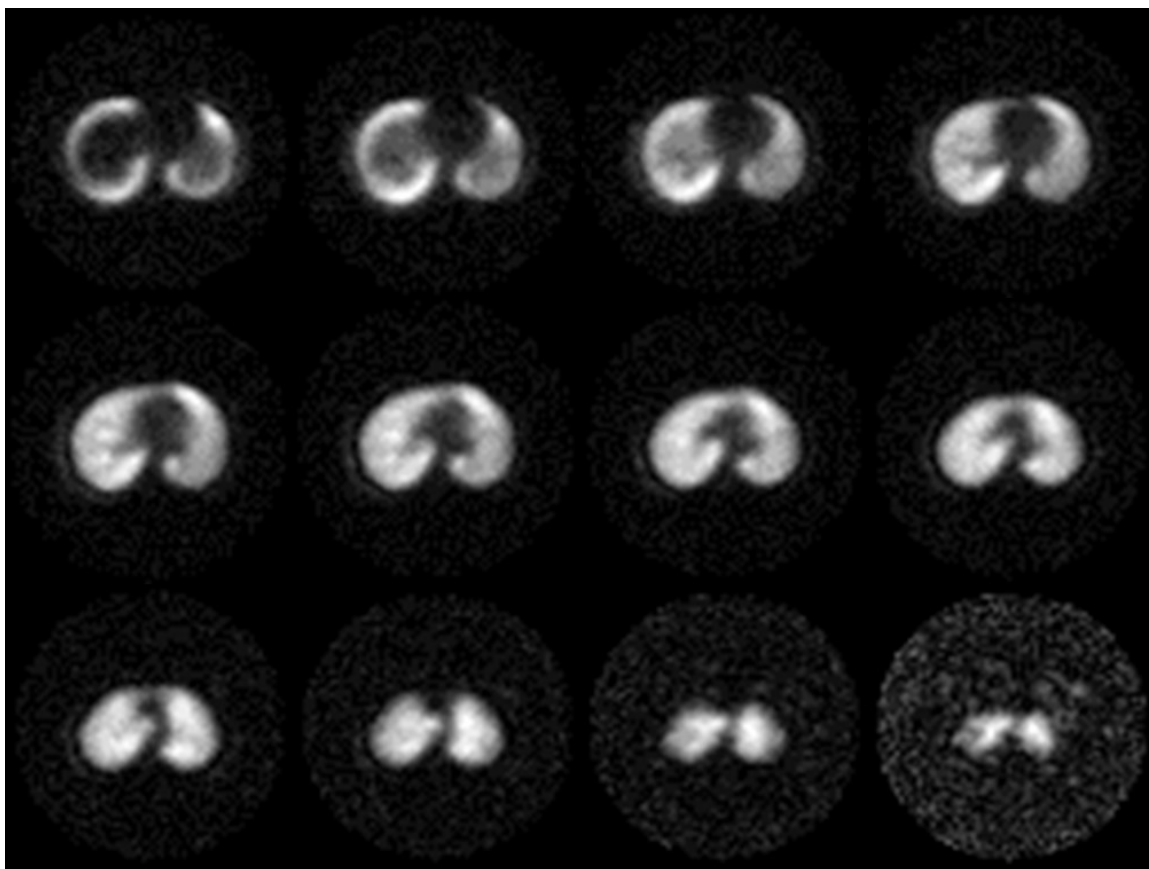


Figure 2-5: ^{19}F 3D UTE lung images acquired in the axial plane from subject #8 during a 15 s breath-hold, following continuous breathing from a 5 L mixture of 79% PFP and 21% O_2 and a 1 L inhalation of the same mixture. Images were reproduced with permission (25).

2.5 Discussion

This feasibility study demonstrates the potential of ^{19}F 3D UTE for imaging of human lungs with inert fluorinated gases. The images obtained using the single breath protocol had a reasonable SNR, which serves as a baseline for comparison since a similar

breathing protocol is generally used for HP ^3He or ^{129}Xe MRI. These images show substantial blurring and lack of edge detail due to the fact that radial acquisitions oversample the center of k-space while sparsely sampling the edges, effects which are compounded by the short T_2^* of PFP. The true potential of this technique can be realized in the use of continuous breathing protocols. Subjects typically breathed the entire 5 L bag of the PFP/ O_2 mixture in 5-7 breaths, which effectively washes out most of the air from the lungs. The entire continuous breathing protocol, including the 15 second breath-hold, was performed in less than one minute. In all subjects, the measured SpO_2 never fell below 88%, which would be considered an adverse event (26), and therefore inhalation of the PFP/ O_2 mixture was well-tolerated in healthy subjects.

With continuous breathing, there is a greater density of ^{19}F nuclei in the lungs to provide a signal, and the PFP gas is able to reach the periphery of the lungs. The greater available magnetization leads to a higher image quality, and allows for more slices to be acquired at smaller slice thicknesses. The SNR from the center slices of images obtained using the continuous breathing protocol was a factor of 2 greater than the SNR from similar slices reported by Soher et al. (20). A number of factors contribute to this difference, including the shorter echo time used in UTE compared to 3D gradient echo, the low bandwidth used in this study (140 Hz/pixel compared to 200 Hz/pixel used by Soher et al.), and the use of continuous breathing.

We recognize that there are a few limitations regarding the imaging technique and breathing protocols. There is a slight ‘halo’ artifact that appears around the lungs, which

is a consequence of the UTE technique, and points to the need for optimization of the trajectory and gradient delays to compensate for eddy currents. In general, UTE yields a high SNR for species that are known to have a short T_2^* , such as inert fluorinated gases. The T_2^* of PFP in human lungs was 2.2 ms, as measured from a single FID following a 90° pulse. SF_6 may benefit even more from a UTE acquisition, since it is expected to have a shorter T_2^* than PFP (12). Another potential limitation to this imaging technique is the ability of patients with lung diseases to perform the breathing protocols, and this needs further investigation. Since it is possible to mix inert fluorinated gases with O_2 , this technique has an advantage over HP noble gases. Therefore, it is possible to maintain an acceptable P_{AO_2} without a significant loss of image quality.

2.6 Conclusion

In this initial proof of concept study, static breath-hold imaging of inert fluorinated gases was performed in healthy subjects only. It may be possible to improve the image SNR through the use of respiratory-gated imaging as opposed to static breath-hold imaging. It will be of great interest to measure additional functional biomarkers, such as wash-in/wash-out kinetics and the apparent diffusion coefficient (ADC), both of which have already been demonstrated in animals (9,16). ^{19}F 3D UTE imaging may also be a useful tool for imaging the lungs of patients with chronic respiratory diseases, such as asthma, COPD, and cystic fibrosis. Overall, this feasibility study demonstrates the potential of ^{19}F 3D UTE MR imaging for visualizing the distribution of inert fluorinated gases in human lungs, and this technique has the advantages of being inexpensive and non-invasive.

2.7 References

1. Jemal A, Ward E, Hao YP, Thun M. Trends in the leading causes of death in the United States, 1970-2002. *Jama-J Am Med Assoc* 2005;294(10):1255-1259.
2. Miller MR, Hankinson J, Brusasco V, Burgos F, Casaburi R, Coates A, Crapo R, Enright P, van der Grinten CP, Gustafsson P, Jensen R, Johnson DC, MacIntyre N, McKay R, Navajas D, Pedersen OF, Pellegrino R, Viegi G, Wanger J. Standardisation of spirometry. *Eur Respir J* 2005;26(2):319-338.
3. Mills GH, Wild JM, Eberle B, Van Beek EJ. Functional magnetic resonance imaging of the lung. *Br J Anaesth* 2003;91(1):16-30.
4. Johnson KM, Fain SB, Schiebler ML, Nagle S. Optimized 3D ultrashort echo time pulmonary MRI. *Magn Reson Med* 2013;70(5):1241-1250.
5. Ohno Y, Chen Q, Hatabu H. Oxygen-enhanced magnetic resonance ventilation imaging of lung. *Eur J Radiol* 2001;37(3):164-171.
6. Albert MS, Cates GD, Driehuys B, Happer W, Saam B, Springer CS, Jr., Wishnia A. Biological magnetic resonance imaging using laser-polarized ^{129}Xe . *Nature* 1994;370(6486):199-201.
7. Altes TA, Salerno M. Hyperpolarized gas MR imaging of the lung. *J Thorac Imaging* 2004;19(4):250-258.
8. Kuethe DO, Caprihan A, Fukushima E, Waggoner RA. Imaging lungs using inert fluorinated gases. *Magn Reson Med* 1998;39(1):85-88.
9. Schreiber WG, Eberle B, Laukemper-Ostendorf S, Markstaller K, Weiler N, Scholz A, Burger K, Heussel CP, Thelen M, Kauczor HU. Dynamic ^{19}F -MRI of pulmonary ventilation using sulfur hexafluoride (SF_6) gas. *Magn Reson Med* 2001;45(4):605-613.
10. Kuethe DO, Behr VC, Begay S. Volume of rat lungs measured throughout the respiratory cycle using ^{19}F NMR of the inert gas SF_6 . *Magn Reson Med* 2002;48(3):547-549.
11. Kuethe DO, Caprihan A, Gach HM, Lowe IJ, Fukushima E. Imaging obstructed ventilation with NMR using inert fluorinated gases. *J Appl Physiol* 2000;88(6):2279-2286.
12. Adolphi NL, Kuethe DO. Quantitative mapping of ventilation-perfusion ratios in lungs by ^{19}F MR imaging of T1 of inert fluorinated gases. *Magn Reson Med* 2008;59(4):739-746.

13. Wolf U, Scholz A, Heussel CP, Markstaller K, Schreiber WG. Subsecond fluorine-19 MRI of the lung. *Magn Reson Med* 2006;55(4):948-951.
14. Scholz AW, Wolf U, Fabel M, Weiler N, Heussel CP, Eberle B, David M, Schreiber WG. Comparison of magnetic resonance imaging of inhaled SF₆ with respiratory gas analysis. *Magn Reson Imaging* 2009;27(4):549-556.
15. Ruiz-Cabello J, Perez-Sanchez JM, Perez de Alejo R, Rodriguez I, Gonzalez-Mangado N, Peces-Barba G, Cortijo M. Diffusion-weighted 19F-MRI of lung periphery: Influence of pressure and air-SF₆ composition on apparent diffusion coefficients. *Respir Physiol Neurobiol* 2005;148(1-2):43-56.
16. Perez-Sanchez JM, Perez de Alejo R, Rodriguez I, Cortijo M, Peces-Barba G, Ruiz-Cabello J. In vivo diffusion weighted 19F MRI using SF₆. *Magn Reson Med* 2005;54(2):460-463.
17. Carrero-Gonzalez L, Kaulisch T, Stiller D. In vivo diffusion-weighted MRI using perfluorinated gases: ADC comparison between healthy and elastase-treated rat lungs. *Magn Reson Med* 2013;70(6):1761-1764.
18. Jacob RE, Chang YV, Choong CK, Bierhals A, Zheng Hu D, Zheng J, Yablonskiy DA, Woods JC, Gierada DS, Conradi MS. 19F MR imaging of ventilation and diffusion in excised lungs. *Magn Reson Med* 2005;54(3):577-585.
19. Conradi MS, Saam BT, Yablonskiy DA, Woods JC. Hyperpolarized 3He and perfluorocarbon gas diffusion MRI of lungs. *Progr NMR Spectr* 2006;48:63-83.
20. Soher BJ, Ainslie M, MacFall J, Hashoian R, Charles HC. Lung Imaging in Humans at 3T using Perfluorinated Gases as MR Contrast Agents. In Proceedings of the 18th Annual Meeting ISMRM, Stockholm, Sweden, 2010. p 3389.
21. Lim H, Thind K, Martinez-Santesteban FM, Scholl TJ. Construction and evaluation of a switch-tuned (13) C - (1) H birdcage radiofrequency coil for imaging the metabolism of hyperpolarized (13) C-enriched compounds. *J Magn Reson Imaging* 2014;40(5):1082-1090.
22. Doganay O, Wade T, Hegarty E, McKenzie C, Schulte RF, Santyr GE. Hyperpolarized Xe imaging of the rat lung using spiral IDEAL. *Magn Reson Med* 2015.
23. Goette MJ, Lanza GM, Caruthers SD, Wickline SA. Improved quantitative (19) F MR molecular imaging with flip angle calibration and B1 -mapping compensation. *J Magn Reson Imaging* 2015;42(2):488-494.
24. Chang YV, Conradi MS. Relaxation and diffusion of perfluorocarbon gas mixtures with oxygen for lung MRI. *J Magn Reson* 2006;181(2):191-198.

25. Couch MJ, Ball IK, Li T, Fox MS, Littlefield SL, Biman B, Albert MS. Pulmonary ultrashort echo time 19F MR imaging with inhaled fluorinated gas mixtures in healthy volunteers: feasibility. *Radiology* 2013;269(3):903-909.
26. West JB. *Respiratory Physiology*. 9th Edition. Philadelphia: Lippincott Williams & Wilkins; 2012.

Chapter 3

Optimized Strategies for Pulmonary ^{19}F MRI Using Inert Fluorinated Gases and Comparison of Ultrashort Echo Time and Gradient Echo Imaging

3.1 Abstract

Purpose: Pulmonary fluorine-19 (^{19}F) magnetic resonance imaging (MRI) using inert fluorinated gases is a technique that can potentially provide high quality images of lung structure and function; however, optimization studies are required in order to achieve the highest possible image quality with this relatively new technique. In this study, ^{19}F 3D MRI of inert fluorinated gases was performed in both a resolution phantom and in the lungs of healthy volunteers. ^{19}F lung images obtained in the same imaging session using ultrashort echo time (UTE) and gradient echo techniques were quantitatively compared.

Methods: Five healthy volunteers were imaged at 3.0 T following continuous breathing of a mixture of 79% perfluoropropane (PFP) and 21% O_2 . 3D UTE and gradient echo images were acquired during separate 15 second breath-holds. Similar imaging was performed in a custom-built resolution phantom filled with either 100% sulphur hexafluoride (SF_6) or 79% PFP and 21% O_2 .

Results: The mean whole-lung signal-to-noise ratio (SNR) in healthy volunteers was significantly greater for UTE than for gradient echo imaging ($p = 0.04$). The mean SNR was 27 ± 12 for UTE, and 16 ± 6 for gradient echo imaging. This trend was also confirmed by phantom imaging.

Conclusion: Although the SNR was higher in 3D UTE images, 3D gradient echo lung images qualitatively appeared to show more detail and had better edge definition. Overall, this preliminary study demonstrates that high quality ^{19}F MR images of inert fluorinated gases in human lungs can be obtained using either a UTE or gradient echo method.

3.2 Introduction

Pulmonary fluorine-19 (^{19}F) magnetic resonance imaging (MRI) using inert fluorinated gases has recently received increased attention, as it can potentially be applied to patients with lung diseases for non-invasive and longitudinal imaging (1). Inert fluorinated gases may be able to provide functional lung information that is similar to hyperpolarized noble gas MRI, without the need for expensive polarizer equipment (2). Inert fluorinated gases, such as tetrafluoromethane (CF_4), sulphur hexafluoride (SF_6), hexafluoroethane (C_2F_6), and perfluoropropane (C_3F_8 or PFP) are nontoxic, abundant, and inexpensive. Due to the high natural abundance (100%) and high gyromagnetic ratio of ^{19}F , there is sufficient thermally polarized signal for imaging. The T_1 of PFP has been previously measured to be 12.4 ms in human lungs at 3 T, which allows for the use of fast repetition times and

averaging within a single breath-hold (3). The first demonstration of inert fluorinated gas MRI was reported over 30 years ago by Heidelberger, Lauterbur and colleagues, and this technique initially used CF_4 to acquire ^{19}F MR images of excised rabbit lungs (4) and healthy dog lungs (5,6). In 1998, Kuethe et al. demonstrated high resolution 3D imaging of rat lungs (7), and since that time, the measurement of various functional biomarkers has been explored, such as wash-in/wash-out kinetics (8-12), volume measurements (13), apparent diffusion coefficients (ADCs) (14-16), and ventilation/perfusion ratios (17,18).

Inert fluorinated gas MR imaging in human lungs was first demonstrated using SF_6 , when Wolf et al. reported 2D whole lung projection images with a relatively low signal-to-noise ratio (SNR) (19). More recently, Halaweish et al. reported 3D gradient echo MR images using inhaled PFP in healthy volunteers, and patients with chronic obstructive pulmonary disease (COPD), asthma, or post lung transplantation (20). Recently, Couch et al. demonstrated substantial improvements in the image signal-to-noise ratio (SNR) using static breath-hold 3D ultrashort echo time (UTE) imaging of healthy volunteers following continuous breathing of a PFP/ O_2 mixture, and a subsequent 15 s breath-hold (3). Since the T_2^* of PFP was measured to be 2.2 ms in human lungs at 3T, the use of UTE acquisition techniques may be a promising alternative to gradient echo imaging (3). However, UTE imaging of inert fluorinated gases in the lungs results in significant image blurring and lack of edge detail (3), whereas gradient echo imaging tends to provide superior edge detail but suffers from a lower SNR due to the longer TE (20). Since the preliminary work published thus far has involved stand-alone studies using different image acquisition techniques, it remains to be determined what type of image acquisition

will provide the highest image quality. The purpose of this study was to perform ^{19}F 3D MR imaging using inert fluorinated gases in both a resolution phantom and in the lungs of healthy volunteers, and to compare the image quality from images that were obtained using UTE and gradient echo acquisitions in the same imaging session (21).

3.3 Methods

3.3.1 Phantom Measurements

All phantom and human lung imaging was performed at 3 T (Philips Achieva, Best, The Netherlands) using a flexible wrap-around quadrature transmit/receive coil (Clinical MR Solutions, Brookfield, WI) tuned to the ^{19}F resonance frequency (120.15 MHz at 3 T). A hollow custom-built resolution phantom was filled with either 100% SF_6 or a mixture of 79% PFP and 21% O_2 (Air Liquide, Plumsteadville, PA). A schematic diagram of the resolution phantom is shown in Figure 3-1. The resolution phantom had an outer diameter of 126 mm and five circular obstructions with various diameters of 19, 10, 6.5, 5 and 3 mm.

T_2^* was measured in the resolution phantom for both gas types using a single free induction decay (FID) following a 90° pulse. The real component of the FID was phase corrected and fitted to an exponential decay function using a non-linear least squares approach to extract the T_2^* .

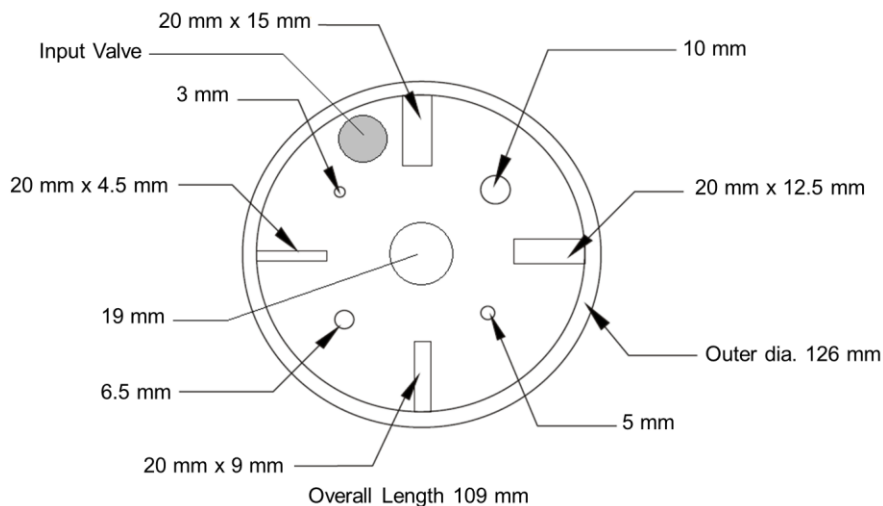


Figure 3-1: Schematic diagram of the resolution phantom that was used for SF₆ and PFP imaging. The outer diameter was 126 mm, and the diameters of the circular obstructions are shown.

¹⁹F 3D UTE, gradient echo and radial images were acquired with the following settings: TR = 20 ms, matrix = 128 x 128, 7 slices, in-plane FOV = 200 x 200 mm², 15 mm thickness, flip angle = 90°, and bandwidth = 140 or 200 Hz/pixel. The TE for each case is shown in Table 3-1. Both gradient echo and radial imaging used the same partial echo factor of 62.5%. The number of averages was set to yield similar scan durations for each acquisition: 12 averages for UTE, 49 averages for gradient echo, and 31 averages for radial. SNR was measured in all UTE, gradient echo, and radial images using Matlab R2011a (The Math-Works, Natick, MA). SNR was defined as the mean signal value from the largest possible rectangular region of interest (ROI) inside the phantom, divided by the standard deviation from a similar ROI in the background.

Table 3-1: Echo times used for all PFP and SF₆ resolution phantom measurements.

Bandwidth (Hz/pixel)	TE (ms)		
	UTE	Gradient Echo	Radial
140	0.13	1.63	1.51
200	0.14	1.36	1.25

3.3.2 Subjects

This study protocol was approved by the local research ethics board and by Health Canada. All subjects provided written informed consent prior to their participation in this study. Five healthy volunteers (4 female and 1 male) were enrolled in this study with no history of chronic or current respiratory disease, and no smoking history. The mean age of all volunteers (\pm standard deviation) was 30 ± 15 years. The women had a mean age of 23.5 years, and the male volunteer was 57 years of age. Digital pulse oximetry was used to monitor SpO₂ for all subjects during scanning sessions (Veris, Medrad, Warrendale, PA).

Conventional ¹H MR images were first acquired while the subject was lying in the actively decoupled ¹⁹F coil. 2D multi-slice gradient echo ¹H images were acquired during a 1 L breath-hold of air, and with the following settings: TR = 50 ms, TE = 1.49 ms, matrix = 128 x 128, 12 slices, in-plane FOV = 450 x 450 mm², 15 mm thickness, 1.5 mm slice gap, flip angle = 11.5°, and bandwidth = 500 Hz/pixel. Prior to ¹⁹F imaging, subjects breathed continuously from a 5 L Tedlar bag (Jensen Inert Products, Coral Springs, FL) of a mixture of 79% PFP and 21% O₂. Subjects were instructed to breathe continuously until the bag was empty, by inhaling a normal tidal volume of gas from the 5 L bag, and

exhaling around the tube. Once empty, the 5 L Tedlar bag was immediately replaced with a full 1 L bag of the same mixture of 79% PFP and 21% O₂; from FRC, the subjects were instructed to completely inhale the 1 L bag and hold their breath for 15 s during image acquisition.

For both ¹⁹F 3D UTE and 3D gradient echo imaging, the scan duration was limited to a single 15 s breath-hold. ¹⁹F 3D UTE imaging used the following settings: TR = 20 ms, TE = 0.2 ms, matrix = 64 x 64, 12 slices, in-plane FOV = 450 x 450 mm², 15 mm thickness, flip angle = 70°, 75% radial sampling density, 1 average, bandwidth = 140 or 200 Hz/pixel, and scan duration = 15 s. ¹⁹F 3D gradient echo images were acquired with the following settings: TR = 27 ms, TE = 1.12 ms, matrix = 64 x 64, 12 slices, in-plane FOV = 450 x 450 mm², 15 mm thickness, flip angle = 70°, partial echo factor = 62.5%, 2 averages, bandwidth = 200 Hz/pixel, and scan duration = 15 s. Whole-lung SNR was measured in all 3D lung images, by manually setting a threshold to separate the lungs from the surrounding background and dividing the mean whole-lung signal value by the standard deviation of an ROI in the background. Whole-lung SNR measurements from ¹⁹F 3D UTE and 3D gradient echo lung images were compared using a two-tailed paired t-test performed in GraphPad Prism (GraphPad Software, La Jolla, CA), and p < 0.05 was considered significant.

3.4 Results

Figure 3-2(a) shows ^{19}F MR images for the resolution phantom filled with PFP from gradient echo, UTE, and radial acquisitions at bandwidths of 140 and 200 Hz/pixel. The T_2^* of PFP was measured to be 5.1 ms in the resolution phantom, which led to a similar SNR for gradient echo and UTE imaging. Figure 3-2(b) shows SF_6 resolution phantom images from gradient echo, UTE, and radial acquisitions at bandwidths of 140 and 200 Hz/pixel. The T_2^* of SF_6 was measured to be 1.2 ms in the resolution phantom, which led to a higher SNR for UTE compared to gradient echo imaging.

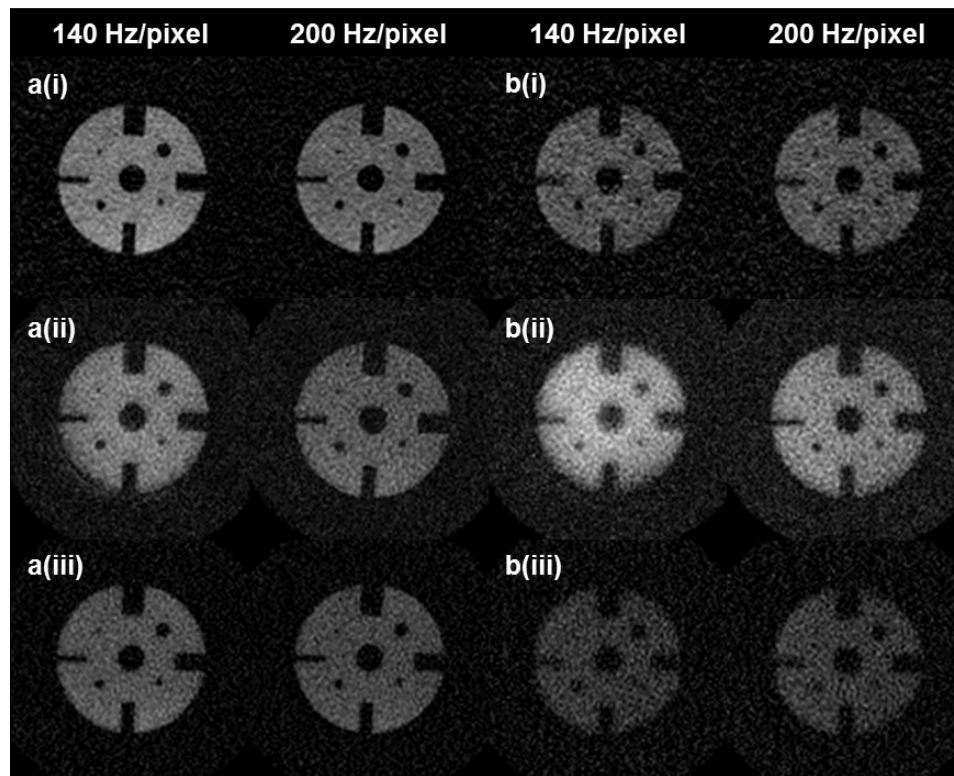


Figure 3-2: Comparison of one slice from 3D images that were obtained in a resolution phantom filled with a mixture of (a) 79% PFP and 21% O_2 or (b) 100% SF_6 . Images were acquired using (i) gradient echo, (ii) UTE and (iii) radial acquisitions, at bandwidths of 140 and 200 Hz/pixel.

Table 3-2 shows the mean SNR measurements for all of the images shown in Figure 3-2. The error in Table 3-2 represents the standard deviation of SNR measurements in the 5 most central slices. In order to make a fair comparison between UTE, gradient echo, and radial imaging, the SNR was normalized by the square root of the scan duration.

Table 3-2: PFP and SF₆ Resolution Phantom Measurements. Mean SNR (\pm standard deviation) from all ¹⁹F 3D UTE, 3D gradient echo, and 3D radial images. The SNR was normalized by the square root of the scan duration.

Bandwidth (Hz/pixel)	PFP SNR			SF ₆ SNR		
	UTE	Gradient Echo	Radial	UTE	Gradient Echo	Radial
140	11.9 \pm 0.4	11.6 \pm 0.5	8.1 \pm 0.3	12.7 \pm 0.7	6.4 \pm 0.3	4.6 \pm 0.2
200	8.3 \pm 0.3	10.1 \pm 0.4	6.7 \pm 0.2	8.9 \pm 0.4	6.5 \pm 0.3	4.8 \pm 0.2

In order to demonstrate the resolving power of PFP and SF₆ imaging in the resolution phantom, Figure 3-3 shows examples of 1D profiles taken from images in Figure 3-2 acquired at a bandwidth of 200 Hz/pixel. Horizontal profiles were chosen such that signal changes due to the 3 mm and 10 mm circular obstructions could be visualized.

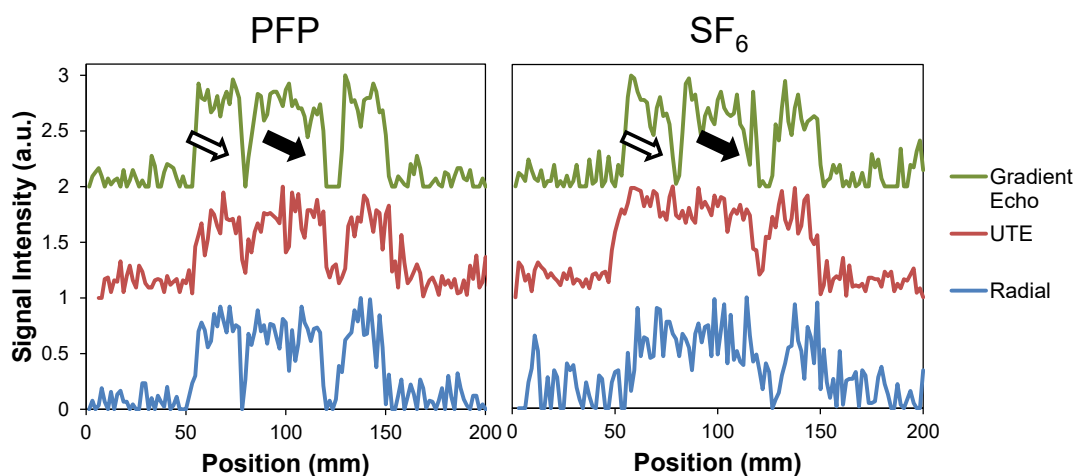


Figure 3-3: 1D profiles taken from PFP (left) and SF₆ (right) images acquired in the resolution phantom at a bandwidth of 200 Hz/pixel. Note that the horizontal signal profiles for gradient echo, UTE, and radial imaging were offset for visual clarity. The white arrow indicates the 3 mm obstruction, and the black arrow indicates the 10 mm obstruction.

In general, PFP appears to visualize small features in the resolution phantom very well, whereas for SF₆ the 3 mm obstruction is only visible in gradient echo imaging.

Table 3-3 summarizes the results from all five healthy volunteers, including the whole-lung SNR measurements from all ¹⁹F UTE and gradient echo images acquired in the coronal plane. For SNR, the error represents the heterogeneity of ¹⁹F signal throughout the entire lungs. Since the imaging parameters for both UTE and gradient echo were adjusted to keep the scan duration to within a 15 s breath-hold, the SNR values were not normalized in Table 3-3.

Table 3-3: Human Lung Imaging. Mean whole-lung SNR (\pm standard deviation) from all available ¹⁹F 3D UTE and gradient echo images that were acquired in the coronal plane.

Subject	Sex	Age	Image SNR		
			UTE (140 Hz/pixel)	UTE (200 Hz/pixel)	Gradient Echo (200 Hz/pixel)
1	f	27	11 \pm 5	9 \pm 3	8 \pm 3
2	f	24	40 \pm 21	-	23 \pm 10
3	m	57	40 \pm 17	-	18 \pm 7
4	f	23	29 \pm 12	20 \pm 8	20 \pm 13 ^a
5	f	20	17 \pm 9 ^b	14 \pm 6 ^b	14 \pm 6 ^c

^a For subject #4, gradient echo images were acquired with TR = 18 ms and NSA = 3.

^b For subject #5, UTE images were acquired with FOV = 400 x 400 mm², TR = 16 ms and 92% angular sampling density.

^c For subject #5, gradient echo images were acquired with FOV = 400 x 400 mm², TR = 16 ms, TE = 1.09 ms and NSA = 3.

For ¹⁹F 3D UTE images at a bandwidth of 140 Hz/pixel, the mean whole-lung SNR was 27 \pm 12, while for 3D gradient echo images, the mean SNR was 16 \pm 6. Overall, the whole lung SNR from UTE images at a bandwidth of 140 Hz/pixel was significantly

higher than gradient echo images at a bandwidth of 200 Hz/pixel ($p = 0.04$). Since UTE images at 200 Hz/pixel were only acquired in three subjects, the SNR was not statistically different from the UTE images at 140 Hz/pixel or the gradient echo images at 200 Hz/pixel.

Figure 3-4 shows a comparison of 4 central slices in the coronal plane from a ^1H localizer, ^{19}F 3D UTE, and ^{19}F 3D gradient echo lung images that were acquired from subject #3. The whole-lung SNR was 40 ± 17 and 18 ± 7 , for the coronal 3D UTE and 3D gradient echo images shown in Figure 3-4, respectively.

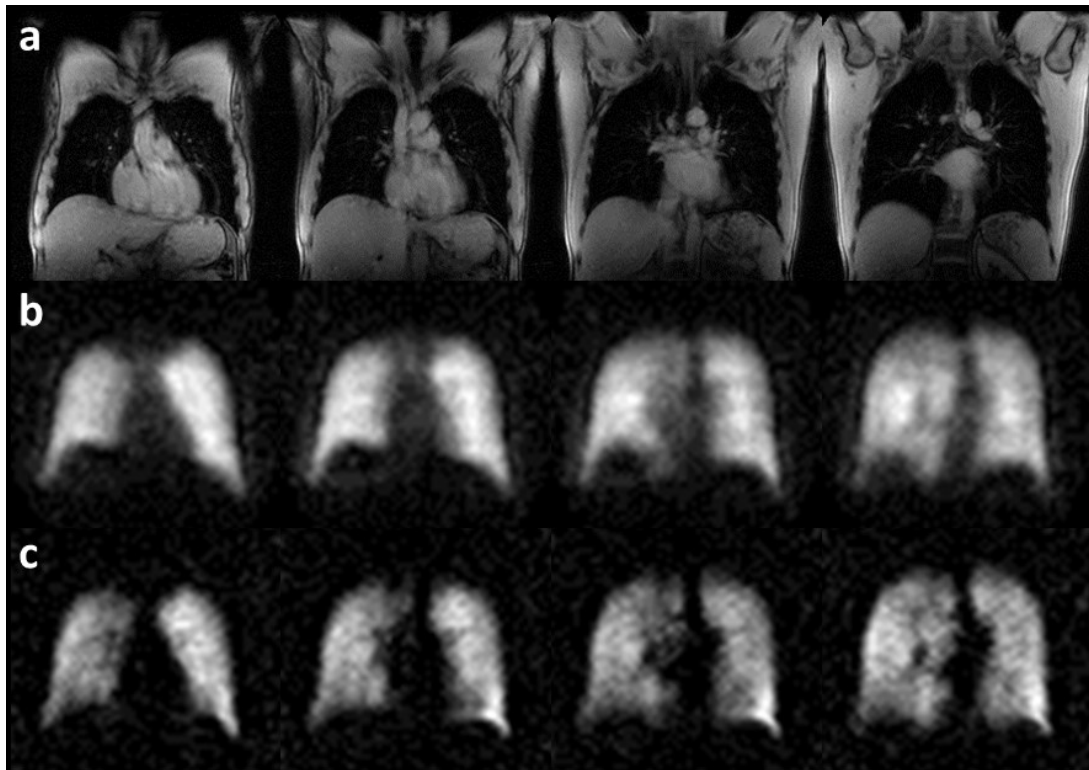


Figure 3-4: Comparison of four central slices from lung images in the coronal plane acquired in subject #3 in the same imaging session: (a) ^1H localizer, (b) ^{19}F 3D UTE, and (c) ^{19}F 3D gradient echo. The UTE images were reproduced with permission (3).

Figure 3-5 shows a similar comparison of 4 central slices in the axial plane from a ^1H localizer, ^{19}F 3D UTE and ^{19}F 3D gradient echo lung images that were acquired from subject #2. The whole-lung SNR was 29 ± 13 and 21 ± 9 , for the axial 3D UTE and 3D gradient echo images shown in Figure 3-5, respectively.

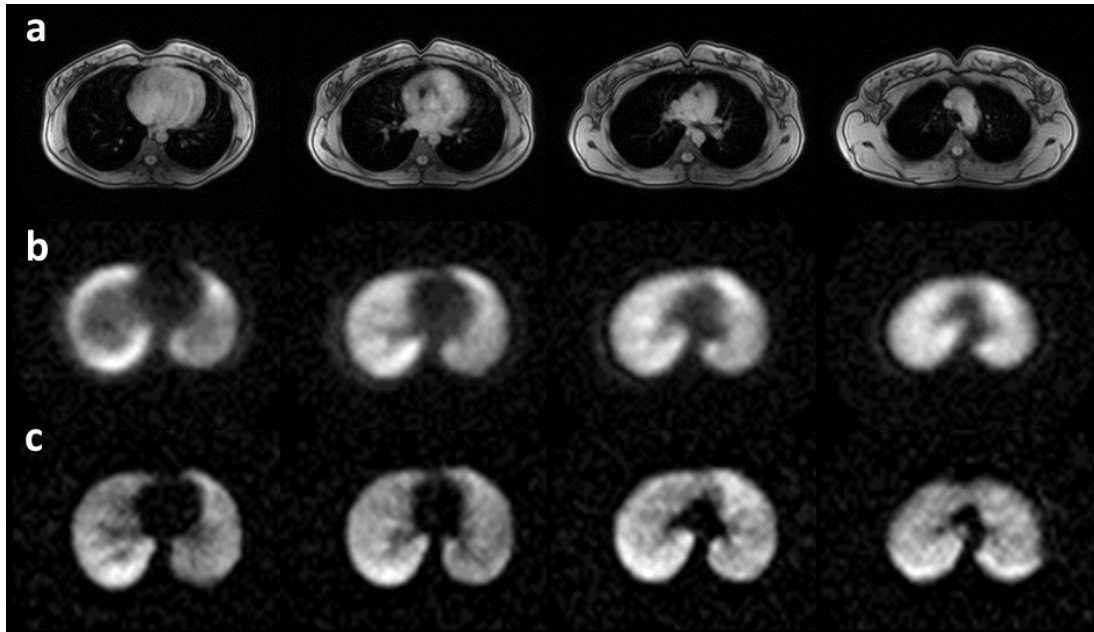


Figure 3-5: Comparison of four central slices from lung images in the axial plane acquired in subject #2 in the same imaging session: (a) ^1H localizer, (b) ^{19}F 3D UTE, and (c) ^{19}F 3D gradient echo. The UTE images were reproduced with permission (3).

Figure 3-6 shows a comparison of center slice coronal and axial images that were acquired using UTE and gradient echo overlaid in colour on ^1H localizer images. Since Figure 3-6 clearly shows the boundary of the thoracic cavity, the blurring effects in UTE imaging are more noticeable.

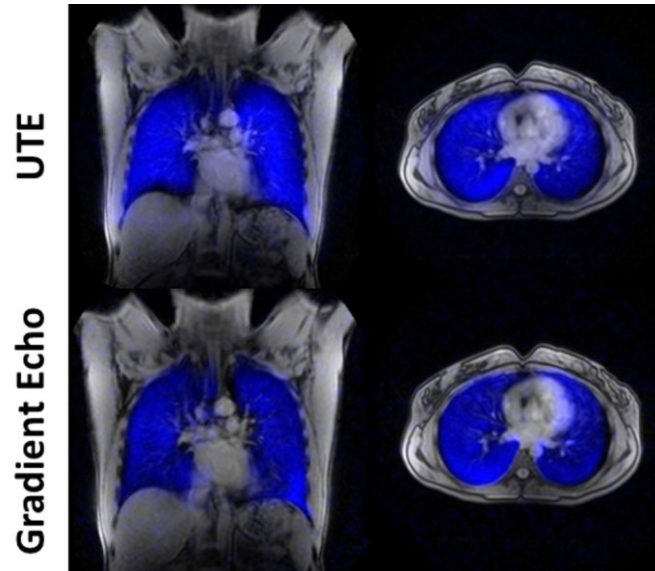


Figure 3-6: Comparison of centre slice coronal (left) and axial (right) MR lung images from ^{19}F 3D UTE (top) and ^{19}F 3D gradient echo (bottom) overlaid in colour on conventional ^1H MR images. The coronal images were acquired in subject #3, while the axial images were acquired in subject #2.

3.5 Discussion

Phantom imaging was initially performed using the same mixture of 79% PFP and 21% O_2 that was used for human lung MR imaging. UTE and gradient echo resolution phantom images had very similar SNRs for PFP, and both techniques had the same resolving power as all five circular obstructions were visible at both 140 and 200 Hz/pixel. However, the T_2^* of PFP in the resolution phantom was substantially longer than the T_2^* of PFP in human lungs (5.1 ms compared to 2.2 ms) (3) and also much longer than any of the TEs used in this study (up to a maximum of 1.63 ms), and therefore, the phantom measurements made using PFP could not be fairly compared to human lung imaging. On the other hand, the T_2^* of SF_6 was measured to be 1.2 ms in the resolution phantom, which was closer to the T_2^* of PFP in the lungs. For the case of SF_6 ,

UTE resolution phantom images had the highest SNR, compared to gradient echo and radial imaging. The UTE SNR also benefited from a lower bandwidth, at the expense of increased blurring due to the short T_2^* and longer acquisition window.

SF₆ gradient echo images at a bandwidth of 200 Hz/pixel had the highest resolving power, as all five circular obstructions were visible (as small as 3 mm in diameter). SF₆ UTE images had a lower resolving power, as only four circular obstructions were visible at both 140 and 200 Hz/pixel (as small as 5 mm in diameter). Since all five circular obstructions were visible in all cases with PFP, the SF₆ phantom images confirm that T_2^* decay is the main reason for blurring in the case of a short T_2^* (such as PFP in human lungs). Radial imaging was also performed in the resolution phantom to provide a point of reference that had similar k-space sampling to UTE, and also had the same partial echo factor as gradient echo imaging (62.5%). Since radial imaging had a lower SNR than both UTE and gradient echo imaging, it is clear that gradient echo benefits from a uniform k-space sampling, and UTE benefits even more from having a very short TE.

Human imaging showed a trend similar to phantom imaging, as the UTE images had a statistically greater SNR than gradient echo images ($p = 0.04$). For subject #2, the SNR in the center slices of coronal 3D UTE images was 43% higher than 3D gradient echo images. An improvement in SNR was expected, since the UTE acquisition had a much shorter TE than gradient echo imaging (0.2 ms compared to 1.12 ms). Assuming a T_2^* of 2.2 ms in the lungs (3), the difference in TE alone should theoretically lead to a 52% difference in SNR. In addition to the increased SNR in UTE images, substantial blurring

was apparent due to the short T_2^* of PFP in combination with a long acquisition window at a bandwidth of 140 Hz/pixel (22). On the other hand, gradient echo images had a lower SNR, but they also had better edge definition than UTE images. For the purposes of comparing image quality for UTE and gradient echo imaging, both acquisitions were limited to a 15 second scan duration. Although the two acquisition techniques had different k-space sampling strategies, the breath-hold length constrained how much sampling could occur within a single image acquisition and holding this parameter constant allowed for a fair comparison to be made between UTE and gradient echo imaging.

3.6 Conclusion

In conclusion, this preliminary study demonstrates that high quality ^{19}F MR images of inert fluorinated gases in human lungs can be obtained using either a 3D UTE or 3D gradient echo method. Although the SNR is higher in UTE images, gradient echo images qualitatively appear to show more detail and have better edge definition. Once fully optimized, this technique may have significant advantages over hyperpolarized noble gas MRI, since it is inexpensive, the gases are abundant, there is a sufficiently high thermal polarization for imaging, and the technique can be performed on any MRI scanner with broadband capability. Overall, inert fluorinated gas MRI has the potential to be a viable clinical imaging modality for non-invasively and longitudinally obtaining functional lung information.

3.7 References

1. Couch MJ, Ball IK, Li T, Fox MS, Ouriadov AV, Biman B, Albert MS. Inert fluorinated gas MRI: a new pulmonary imaging modality. *NMR Biomed* 2014;27(12):1525-1534.
2. Couch MJ, Blasiak B, Tomanek B, Ouriadov AV, Fox MS, Dowhos KM, Albert MS. Hyperpolarized and Inert Gas MRI: The Future. *Mol Imaging Biol* 2015;17(2):149-162.
3. Couch MJ, Ball IK, Li T, Fox MS, Littlefield SL, Biman B, Albert MS. Pulmonary ultrashort echo time ^{19}F MR imaging with inhaled fluorinated gas mixtures in healthy volunteers: feasibility. *Radiology* 2013;269(3):903-909.
4. Heidelberger E, Lauterbur PC. Gas Phase ^{19}F -NMR Zeugmatography: A New Approach to Lung Ventilation Imaging. In Proc 1st Annual Meeting Society of Magnetic Resonance in Medicine, 1982. p 70-71.
5. Rinck PA, Petersen SB, Lauterbur PC. NMR-Imaging von fluorhaltigen Substanzen. ^{19}F -Ventilations- und -Perfusionsdarstellungen. *Fortschr Röntgenstr* 1984;140(3):239-243.
6. Rinck PA, Peterson SB, Heidelberger E, Acuff V, Reinders J, Bernardo ML, Hedges LK, Lauterbur PC. NMR ventilation imaging of the lungs using perfluorinated gases. *Magn Reson Med* 1984;1(2):237-237.
7. Kuethe DO, Caprihan A, Fukushima E, Waggoner RA. Imaging lungs using inert fluorinated gases. *Magn Reson Med* 1998;39(1):85-88.
8. Schreiber WG, Eberle B, Laukemper-Ostendorf S, Markstaller K, Weiler N, Scholz A, Burger K, Heussel CP, Thelen M, Kauczor HU. Dynamic ^{19}F -MRI of pulmonary ventilation using sulfur hexafluoride (SF_6) gas. *Magn Reson Med* 2001;45(4):605-613.
9. Scholz AW, Wolf U, Fabel M, Weiler N, Heussel CP, Eberle B, David M, Schreiber WG. Comparison of magnetic resonance imaging of inhaled SF_6 with respiratory gas analysis. *Magn Reson Imaging* 2009;27(4):549-556.
10. Wolf U, Scholz A, Heussel CP, Markstaller K, Schreiber WG. Subsecond fluorine-19 MRI of the lung. *Magn Reson Med* 2006;55(4):948-951.
11. Wolf U, Scholz A, Terekhov M, Koebrich R, David M, Schreiber LM. Visualization of inert gas wash-out during high-frequency oscillatory ventilation using fluorine-19 MRI. *Magn Reson Med* 2010;64(5):1478-1483.

12. Ouriadov AV, Fox MS, Couch MJ, Li T, Ball IK, Albert MS. In vivo regional ventilation mapping using fluorinated gas MRI with an x-centric FGRE method. *Magn Reson Med* 2015;74(2):550-557.
13. Kuethe DO, Behr VC, Begay S. Volume of rat lungs measured throughout the respiratory cycle using ¹⁹F NMR of the inert gas SF₆. *Magn Reson Med* 2002;48(3):547-549.
14. Carrero-Gonzalez L, Kaulisch T, Stiller D. In vivo diffusion-weighted MRI using perfluorinated gases: ADC comparison between healthy and elastase-treated rat lungs. *Magn Reson Med* 2013;70(6):1761-1764.
15. Jacob RE, Chang YV, Choong CK, Bierhals A, Zheng Hu D, Zheng J, Yablonskiy DA, Woods JC, Gierada DS, Conradi MS. ¹⁹F MR imaging of ventilation and diffusion in excised lungs. *Magn Reson Med* 2005;54(3):577-585.
16. Perez-Sanchez JM, Perez de Alejo R, Rodriguez I, Cortijo M, Peces-Barba G, Ruiz-Cabello J. In vivo diffusion weighted ¹⁹F MRI using SF₆. *Magn Reson Med* 2005;54(2):460-463.
17. Kuethe DO, Caprihan A, Gach HM, Lowe IJ, Fukushima E. Imaging obstructed ventilation with NMR using inert fluorinated gases. *J Appl Physiol* 2000;88(6):2279-2286.
18. Adolphi NL, Kuethe DO. Quantitative mapping of ventilation-perfusion ratios in lungs by ¹⁹F MR imaging of T1 of inert fluorinated gases. *Magn Reson Med* 2008;59(4):739-746.
19. Wolf U, Scholz A, Terekhov M, Muennemann K, Kreitner K, Werner C, Dueber C, Schreiber WG. Fluorine-19 MRI of the lung: first human experiment. In Proc 16th Annual Meeting of ISMRM, 2008. p 3207.
20. Halaweish AF, Moon RE, Foster WM, Soher BJ, McAdams HP, MacFall JR, Ainslie MD, MacIntyre NR, Charles HC. Perfluoropropane gas as a magnetic resonance lung imaging contrast agent in humans. *Chest* 2013;144(4):1300-1310.
21. Couch MJ, Ball IK, Li T, Fox MS, Ouriadov AV, Biman B, Albert MS. Optimized Strategies for ¹⁹F MRI of Human Lungs and Comparison of UTE and Gradient Echo Imaging. In Proc 22nd Annual Meeting of ISMRM, 2014. p 777.
22. Rahmer J, Bornert P, Groen J, Bos C. Three-dimensional radial ultrashort echo-time imaging with T2 adapted sampling. *Magn Reson Med* 2006;55(5):1075-1082.

Chapter 4

Preliminary Measurements of Functional Biomarkers Using ^{19}F MRI of Inert Fluorinated Gases

4.1 Introduction

Chapters 2 and 3 have discussed preliminary developments in inert fluorinated gas MRI, where UTE and gradient echo imaging was performed in healthy volunteers. This imaging was performed during 15 second breath-holds, which provides a static “snapshot” of ventilation function. The resulting images were able to visualize the distribution of the inhaled gas, and future imaging in patients with respiratory diseases is expected to yield the characteristic patterns of ventilation defects. In addition to the static breath-hold imaging that has already been presented, inert fluorinated gas MRI can also be used to measure functional biomarkers that can provide sensitive and quantitative diagnostic information.

This chapter consists of three brief studies that investigated the potential for using inert fluorinated gas MRI to measure functional image-derived biomarkers. The first study performed volume measurements in healthy volunteers to derive the ventilated volume (VV), the ventilation defect volume (VDV), and the ventilation defect percent (VDP). In order to provide a baseline for comparison, these results were compared to similar

volume measurements that were obtained using HP ^3He MRI. Although ventilation defects are expected to be small in healthy volunteers, validating these measurements is an important step towards imaging patients with respiratory diseases.

The second study in this chapter presents preliminary measurements of inert fluorinated gas apparent diffusion coefficients (ADCs) in a single healthy volunteer. The ADC is a biomarker that is sensitive to microstructural changes in the lungs, such as the destruction of alveolar walls in emphysema. The final study in this chapter investigates gravitational gradients in ventilation using inert fluorinated gas MRI. Gravitational gradients were evaluated in a group of healthy volunteers, and these results agreed with expectations based on known patterns in lung physiology. Overall, the image-derived biomarkers presented in this chapter have the potential yield valuable insight into lung function and disease severity. Future studies using these techniques in patients with lung diseases will to help evaluate the diagnostic abilities of inert fluorinated gas MRI.

4.2 Volume Measurements and Comparison to HP ^3He MRI

4.2.1 Introduction

Fluorine-19 (^{19}F) magnetic resonance imaging (MRI) of the lungs using inhaled inert fluorinated gases is a technique currently under development that can potentially provide images of the distribution of pulmonary ventilation, similar to hyperpolarized (HP) noble gas MRI. Inert fluorinated gases, such as sulfur hexafluoride (SF_6) and perfluoropropane

(C₃F₈ or PFP), have several potential advantages over HP gases, as they are nontoxic, abundant, and inexpensive. MR imaging of thermally polarized inert fluorinated gases is made possible due to the high gyromagnetic ratio and high natural abundance of ¹⁹F. Furthermore, the short longitudinal relaxation times of inert fluorinated gases allows for many signal averages within a single breath-hold. Therefore, pulmonary ¹⁹F MRI is possible without the expensive polarizer and scarce isotopes that are required for HP gas MRI.

Inert fluorinated gas MR imaging of the lungs has been previously demonstrated in a number of animal studies (1-3), and more recent work has demonstrated imaging in healthy volunteers (4) and in patients with lung diseases such as chronic obstructive pulmonary disease (COPD), asthma, and lung transplants (5). The work to date has been performed in stand-alone studies using various imaging techniques and different parameters to optimize the image quality. As interest in this new pulmonary imaging technique is growing, validation studies and comparisons to existing pulmonary imaging techniques will be required in order to consider all factors that contribute to image features and image quality, including the physical properties of these heavy fluorinated gases. Therefore, the goal of the present study was to perform a quantitative comparison between lung images obtained using inert fluorinated gas MRI and HP ³He MRI in the same subjects (6).

4.2.2 Methods

This study protocol was approved by the local research ethics board and by Health Canada. All subjects provided written informed consent prior to their participation in this study. Five healthy female volunteers (mean age = 23 ± 3 years) were enrolled in this study with no previous history of lung disease and no previous history of smoking. All imaging in this study was performed using a 3 T scanner (Philips Achieva, Best, The Netherlands) and two flexible wrap-around quadrature transmit/receive coils tuned to either the ^3He or ^{19}F resonance frequencies (Clinical MR Solutions). Conventional ^1H 2D multi-slice gradient echo images were initially acquired using a 1 L breath-hold of air with the following settings: TR = 50 ms, TE = 1.49 ms, matrix = 128 x 128, 12 slices, in-plane FOV = 450 x 450 mm², 15 mm thickness, 1.5 mm slice gap, flip angle = 11.5°, and bandwidth = 500 Hz/pixel. Conventional ^1H images were obtained in both the coronal and axial planes to facilitate planning ^3He and ^{19}F image acquisitions.

^3He was polarized using spin-exchange optical pumping (SEOP) in a custom-built polarizer. After approximately 18 hours of optical pumping, the ^3He polarization was about 15%. HP ^3He MR images were acquired following inhalation of a 1 L bag containing 330 mL of HP ^3He balanced to 1 L with N₂. HP ^3He images were obtained during a 15 s breath-hold using a 2D multi-slice gradient echo method in the coronal plane with the following settings: TR = 56 ms, TE = 1.53 ms, matrix = 128 x 64 reconstructed to 256 x 256, 14 slices, in-plane FOV = 450 x 450 mm², 15 mm thickness, flip angle = 7°, and BW = 500 Hz/pixel.

^{19}F images were obtained during a 25 s breath-hold using either a 3D ultrashort echo time (UTE) or 3D gradient echo acquisition that followed several wash-out breaths of a mixture of 79% PFP and 21% O_2 . ^{19}F 3D UTE imaging used the following settings: TR = 20 ms, TE = 0.2 ms, matrix = 64 x 64, 12 slices, in-plane FOV = 450 x 450 mm², 15 mm thickness, flip angle = 70°, 75% radial sampling density, and BW = 200 Hz/pixel. ^{19}F 3D gradient echo images were acquired with the following settings: TR = 16 ms, TE = 1.08 ms, matrix = 64 x 64, 12 slices, in-plane FOV = 450 x 450 mm², 15 mm thickness, flip angle = 70°, 5 averages, and BW = 200 Hz/pixel.

The signal-to-noise ratio (SNR) was measured for all ^{19}F and ^3He images using custom-built software written in Matlab R2011a (The Math-Works, Natick, MA). The semi-automated segmentation algorithm of Kirby et al. (7) was used to calculate the VV, VDV, and VDP for all ^{19}F and ^3He images. Figure 4-1 shows a schematic diagram of the semi-automated segmentation algorithm. The first step in the algorithm is to segment the ventilation image using k-means clustering, which separates the image into five distinct clusters with gradations in signal intensity from no signal (cluster 1) and low signal (cluster 2) to high signal (cluster 5). Next, the thoracic cavity is segmented from the conventional ^1H MR image using a seeded region-growing method. The ventilation image is then overlaid on the segmented thoracic cavity using a landmark-based registration method. Following image segmentation, the VDV is then calculated by multiplying the number of voxels in cluster 1 by the volume occupied by each voxel. Similarly, the VV is the sum of the voxels in clusters 2 through 5 multiplied by the volume per voxel.

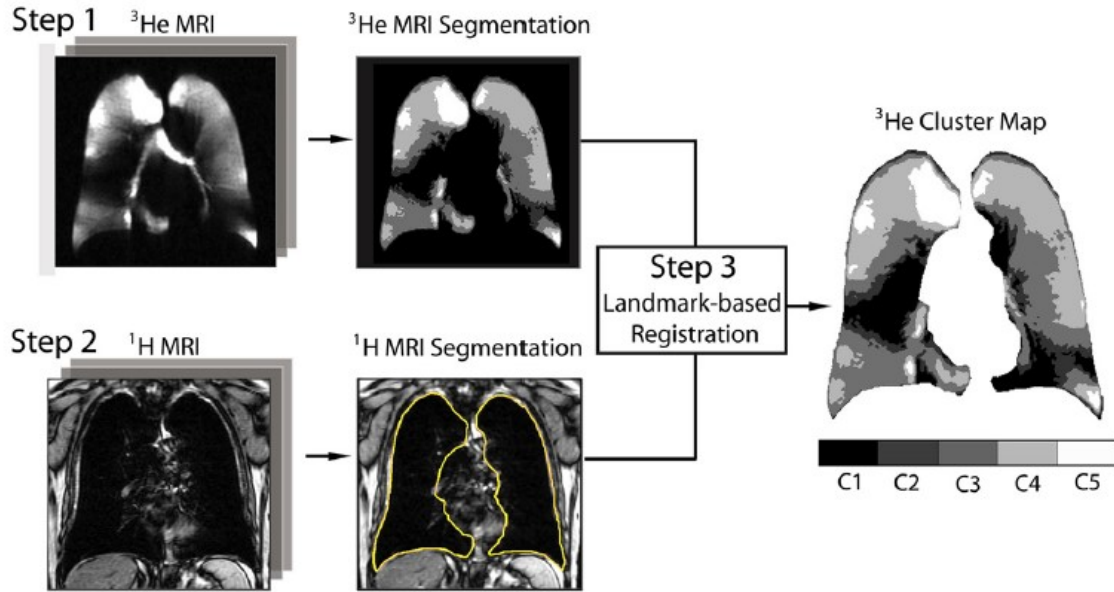


Figure 4-1: Schematic diagram of the semi-automated segmentation algorithm. Images were reproduced with permission from Kirby et al. (7).

The VDP is essentially the VDV normalized to the thoracic cavity volume (TCV), and it is given by the following expression:

$$VDP = \frac{VDV}{TCV} \cdot 100\% = \frac{VDV}{VV + VDV} \cdot 100\% \quad [4-1]$$

The SNR and volume measurements were compared between HP ^3He and ^{19}F imaging using a two-tailed paired t-test in GraphPad Prism (GraphPad Software, La Jolla, CA), where $p < 0.05$ was considered to be significant.

4.2.3 Results

Figure 4-2 shows a comparison of 4 central coronal slices that were obtained using a conventional ^1H localizer, a HP ^3He 2D multi-slice gradient echo, a ^{19}F 3D gradient echo, and a ^{19}F 3D UTE in subject #4. Qualitatively, the HP ^3He images clearly have a superior SNR, and images can easily be acquired at a much higher resolution than the inert

fluorinated gas images. The HP ^3He images also show more fine detail, such as the major airways and pulmonary vasculature. On the other hand, the image quality from inert fluorinated gas imaging appears promising, in spite of the fact that SNR is clearly lower than HP ^3He imaging.

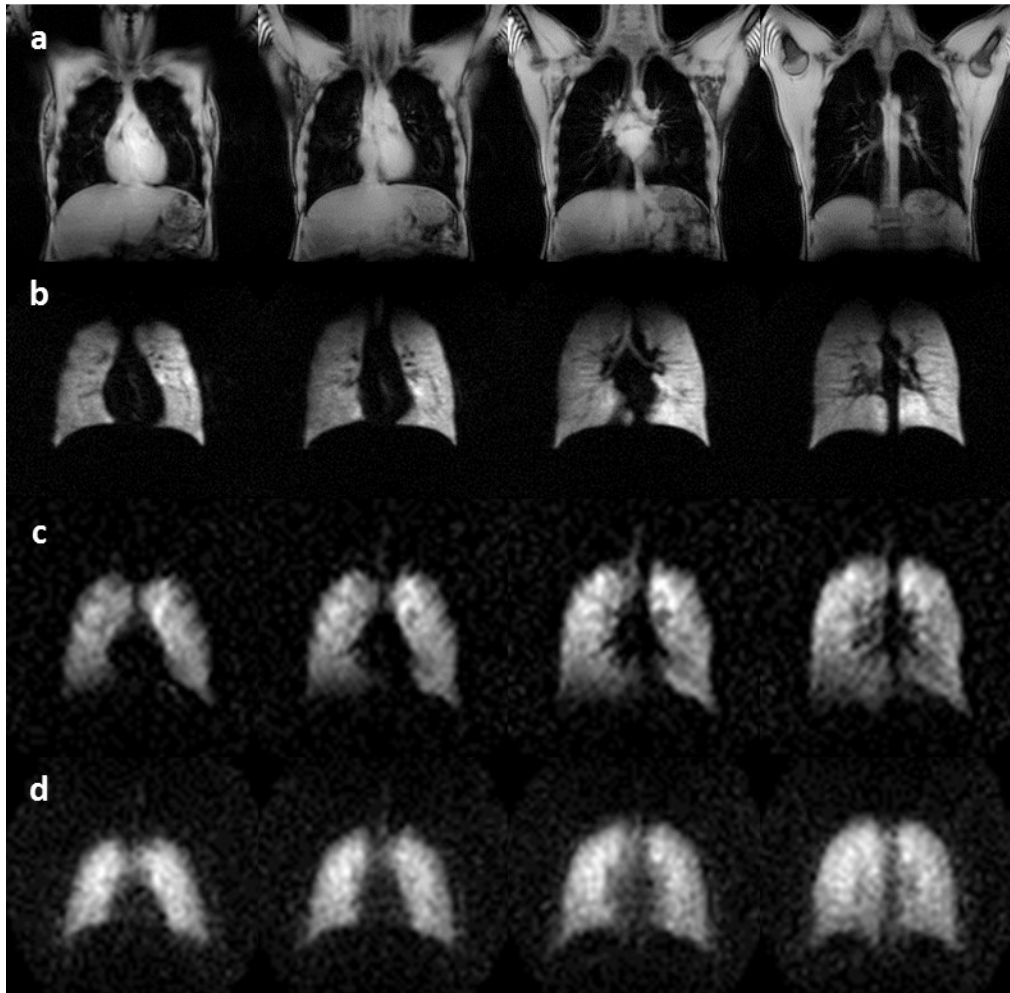


Figure 4-2: Comparison of representative (a) ^1H localizer, (b) ^3He 2D gradient echo, (c) ^{19}F 3D gradient echo, and (d) ^{19}F 3D UTE images acquired in the same healthy volunteer.

A summary of the measured SNR from all HP ^3He and ^{19}F images is shown in Table 4-1. Note that the type of image acquisition used for ^{19}F MRI is indicated. The HP ^3He SNR was significantly greater than the SNR from inert fluorinated gas imaging ($p = 0.01$). The HP ^3He SNR ranged from 39 to 75, while the inert fluorinated gas SNR ranged from 8 to 18. Variability in the HP ^3He SNR can be explained by day-to-day variability in polarizer performance, while variability in the inert fluorinated gas SNR can be explained by variations in coil calibration due to body size as well as subject compliance with regard to taking multiple breaths of the fluorinated gas mixture.

Table 4-1: Comparison of SNR measurements obtained from ^3He and ^{19}F MRI in all subjects.

Subject	^3He SNR	^{19}F SNR	^{19}F Sequence
1	72 ± 37	18 ± 8	3D UTE
2	99 ± 50	8 ± 3	3D UTE
3	75 ± 36	8 ± 2	3D UTE
4	40 ± 18	16 ± 6	3D Gradient Echo
		15 ± 6	3D UTE
5	39 ± 16	9 ± 4	3D Gradient Echo

Table 4-2 summarizes the volumetric measurements that were obtained from three subjects in this study. Two of the five subjects in this study were not included in the volume measurements, since a larger slice thickness was used in those cases (22 mm compared to 15 mm). For the 3 subjects shown in Table 4-2, the VV, VDV, and VDP measurements were not statistically different between HP ^3He MRI and inert fluorinated gas MRI ($p > 0.05$).

Table 4-2: Comparison of VV, VDV and VDP measurements obtained from ^3He and ^{19}F MR imaging in the lungs of three subjects.

Subject	^3He			^{19}F		
	VV (L)	VDV (L)	VDP (%)	VV (L)	VDV (L)	VDP (%)
3	3.8	0.11	2.9	3.34	0.55	14.14
4	4.9	0.28	5.35	6.13	0.55	8.3 (GE)
				5.33	0.24	4.29 (UTE)
5	5.33	0.27	4.83	5.05	0.59	10.5

4.2.4 Discussion

This preliminary study demonstrates, for the first time, a quantitative comparison between HP ^3He MRI and inert fluorinated gas MRI in the same healthy volunteers. In order to assess the images that were produced by these two techniques, SNR and volumetric parameters were measured. As expected, the SNR was significantly larger for HP ^3He MRI compared to inert fluorinated gas imaging. At this point in time, ^{19}F images do suffer from a poor resolution, poorly defined edges, and T_2^* -induced blurring is particularly apparent in the ^{19}F UTE images. The image quality of inert fluorinated gas MRI will continue to be improved with the use of phased array coils (8,9), as well as novel and efficient image acquisition techniques, such as x-centric (3); however, there is a possibility that the current image quality of inert fluorinated gas imaging is sufficient for diagnostic decision making. Future comparisons in patients with pulmonary diseases, such as asthma and COPD, will help to determine the true clinical potential of inert fluorinated gas MRI.

The VV, VDV, and VDP measurements from HP ^3He and inert fluorinated gas imaging were statistically indistinguishable in this preliminary study. As expected, the VV

measurements were similar for both techniques in most cases, since imaging was performed at approximately FRC + 1 L. In most cases, the VDV and VDP were slightly larger for inert fluorinated gas imaging compared to ^3He MRI. This result may be explained by a lower SNR and poorly defined edges, or it may be related to differences in the physical properties of the inhaled gases. That is, the density and diffusivity of PFP will be important in interpreting the size of ventilation defects, as a recent comparison of VDV measurements performed using HP ^3He and HP ^{129}Xe MRI in COPD patients demonstrated a significantly greater VDV as measured from HP ^{129}Xe MRI. It was suggested that these apparent differences in VDV might be related to the higher density and lower diffusivity of ^{129}Xe , which might lead to slower filling in the terminal airways, and hence, larger apparent ventilation defects (10).

Although it may be reasonable to assume that the high density and low diffusivity of inert fluorinated gases will lead to large apparent ventilation defects in patients with pulmonary diseases, it is also possible that the use of continuous breathing might offset these effects. That is, continuous breathing prior to imaging allows for a steady-state concentration of the inert fluorinated gas to be reached, which may compensate for the slow filling of heavy gases and make ventilation defects appear smaller. Ultimately, the context of the measurement will need to be taken into account in order to properly interpret the size of ventilation defects. Furthermore, an accurate measurement of VV and VDV using inert fluorinated gas MRI may require corrections for B_1 inhomogeneity (11). Naturally, many more subjects will be required in order to fully validate inert fluorinated

gas imaging, as well as future comparisons in patients with pulmonary diseases to determine if the volume measurements yield clinically meaningful results.

4.2.5 Conclusions

Although the SNR from inert fluorinated gas MR lung images was less than HP ^3He imaging, the lung volume measurements in this preliminary study were statistically indistinguishable between the two techniques. Therefore, inert fluorinated gas MRI has the potential to yield meaningful functional information that is similar to HP ^3He MRI. Future comparison studies in additional subjects and in patients with pulmonary diseases will determine if inert fluorinated gas MRI can become a viable clinical imaging modality that can aid in diagnostic decision making.

4.3 Diffusion Imaging

4.3.1 Diffusion Physics

Brownian motion refers to the random movement of particles, and this phenomenon was famously described by Einstein in one of his ground-breaking 1905 papers (12). An atom or molecule undergoing a random walk will travel a root mean squared distance, σ , that is given by the following equation in three dimensions:

$$\sigma = \sqrt{6 \cdot D_0 \cdot \Delta}. \quad [4-2]$$

where Δ is the diffusion time and D_0 is the self-diffusion coefficient. For example, a gas such as ^3He has a self-diffusion coefficient of $2.05 \text{ cm}^2\cdot\text{s}^{-1}$, and in 1 ms, it will travel a root mean squared distance of 1.1 mm. In air, ^3He has a lower diffusion coefficient of $0.86 \text{ cm}^2\cdot\text{s}^{-1}$ (due to collisions with larger gas molecules), and it would travel a root mean squared distance of 0.72 mm in 1 ms.

In a restricted environment, such as porous media and lung tissue, the actual distance the atom or molecule travels is limited by the geometry of the container. For example, human alveoli have an approximate diameter of $200 \text{ }\mu\text{m}$ (13), and therefore, this physical boundary would reduce the measured diffusion coefficient of ^3He at diffusion times on the order of a few milliseconds. In this regime, the measured diffusion coefficient is referred to as the *apparent* diffusion coefficient (ADC). ADC can be measured in MRI by encoding the diffusion information with the application of bipolar diffusion-sensitizing gradients prior to the signal readout. For example, Figure 4-3 shows a basic 2D gradient echo acquisition with diffusion sensitization along the phase encoding direction. The time between the leading edges of the bipolar diffusion-sensitizing gradient lobes is defined as the diffusion time, Δ . In principle, diffusion sensitization can be combined with virtually any readout strategy.

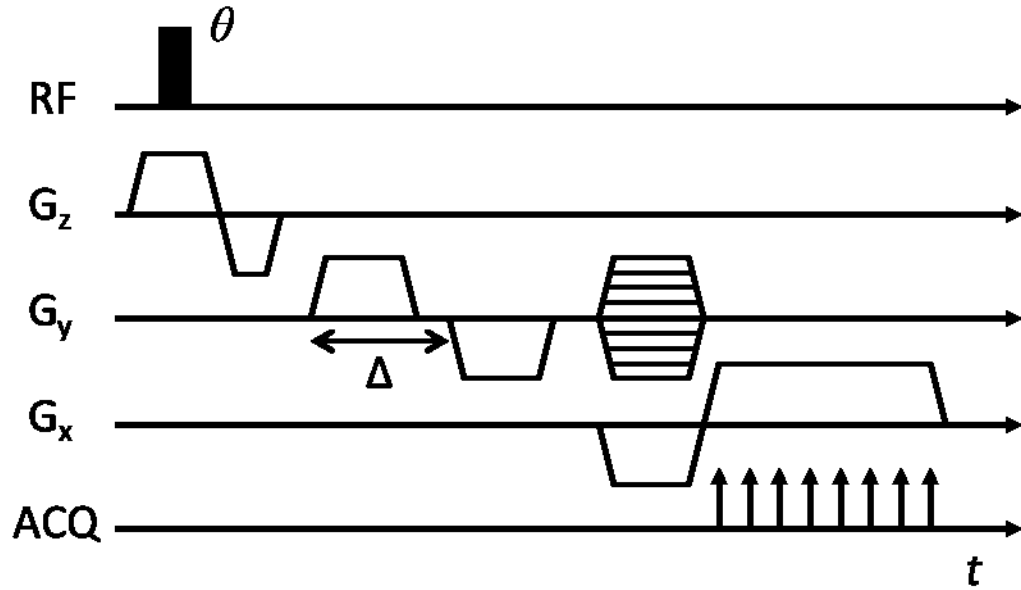


Figure 4-3: Pulse sequence diagram for a 2D gradient echo acquisition with diffusion sensitization along the phase encoding direction.

In Figure 4-3, the total area underneath the bipolar diffusion-sensitizing gradients is zero, which means that any phase accumulated during this time is due to Brownian motion only. Therefore, the diffusion-induced signal decay can be expressed in the following way:

$$S = S_0 \cdot e^{-b \cdot ADC}, \quad [4-3]$$

where S_0 is the original signal without diffusion sensitization, S is the signal with accumulated phase due to diffusion sensitization, and b is a parameter characterizing the amount of diffusion sensitization in units of $\text{s} \cdot \text{cm}^{-2}$. A simple rearrangement of the previous expression can isolate the ADC:

$$ADC = \frac{\ln\left(\frac{S_0}{S}\right)}{b}. \quad [4-4]$$

Therefore, at least two measurements are required in order to calculate the ADC: one image with diffusion sensitization, and one without (i.e. $b = 0$).

4.3.2 Diffusion Measurements in the Lung

In conventional ^1H MRI, diffusion-weighted imaging (DWI) is typically used to measure the ADC of water molecules, and there are numerous applications such as diffusion tensor imaging (DTI) and tractography (14). In the context of the lungs, DWI of gases uses essentially the same basic principles; however, the diffusion coefficients of gases are typically several orders of magnitude larger than the diffusion coefficient of water. Table 4-3 lists the diffusion coefficients of ^3He , ^{129}Xe , PFP and SF_6 , and for comparison, the self-diffusion coefficient of water is approximately $2 \cdot 10^{-5} \text{ cm}^2 \cdot \text{s}^{-1}$ at room temperature (15). Generally speaking, ^3He is a very light gas that has a relatively high diffusion coefficient, while the inert fluorinated gases are very heavy and have the lowest diffusion coefficients. The diffusion coefficient of ^{129}Xe is somewhat between ^3He and the fluorinated gases.

Table 4-3: Diffusion coefficients for ^{129}Xe , ^3He , PFP, and SF_6 , in units of $[\text{cm}^2 \cdot \text{s}^{-1}]$ (16-18).

Parameter	^{129}Xe	^3He	PFP	SF_6
Self-diffusion coefficient, D_0	0.061	2.05	0.023	0.033
Diffusion coefficient in air, D	0.14	0.86	0.071	0.094

HP noble gas ADC measurements performed using ^3He and ^{129}Xe are well-known to be sensitive to the lung microstructure, and these measurements can distinguish between healthy and emphysematous tissue (19,20). That is, a higher ADC can be measured in patients with emphysema, and this difference can be explained by enlarged alveoli caused by the destruction of alveolar walls. HP gas ADC measurements have been shown to be reproducible (21), and ADCs have been correlated with spirometric indices, such as FEV_1

and FVC. ADC measurements have also been successfully validated with a comparison to standard histological measurements, such as the surface to volume ratio (S/V) and mean linear intercept (L_m) (22).

HP gas ADC is also able to measure morphological parameters by acquiring images at multiple b values and fitting to geometrical models, such as the model of Yablonskiy et al. (23,24). The Yablonskiy model is able to measure physical parameters that are related to anisotropic diffusion and the geometry of acinar airways, and this model has also been successfully validated with a comparison to histology (25). Due to the exceedingly high cost and limited availability of ^3He , HP ^{129}Xe MR imaging has received increased attention recently and the literature has focused on developing HP ^{129}Xe ADC (20) and validating these measurements with a comparison to HP ^3He MRI (10,26).

Preliminary inert fluorinated gas ADC measurements are currently underway, and this technique may be able to provide similar information to HP noble gas MRI. The first demonstration of inert fluorinated gas ADC measurements was performed in healthy rats using SF_6 , and the measured ADC was slightly less than the self-diffusion coefficient of SF_6 (18,27). An elastase-induced model of emphysema in rats was employed to help determine whether this technique had a potential to detect pulmonary disease, and elevated C_2F_6 ADC values were detected in emphysematous regions of rat lungs (28). Significant differences in C_2F_6 ADC values were also detected in a study of healthy and emphysematous excised human lungs (29,30), which was an important first step towards translating this technique to human imaging.

4.3.3 Preliminary ^{19}F ADC Measurements in Human Lungs

Despite the challenges of imaging fluorinated gases with very short T_2^* values, it is possible to probe ADCs in humans using a UTE approach in combination with bi-polar diffusion-sensitizing gradients (31). As an example, Figure 4-4 shows two sets of ^{19}F 3D UTE lung images that were acquired in a healthy volunteer during a single 15 second breath-hold of a mixture of 79% PFP and 21% O_2 *. Similar to the ^{19}F 3D UTE images shown in Figure 2-4 and Figure 2-5, imaging followed continuous breathing of the PFP/ O_2 mixture.

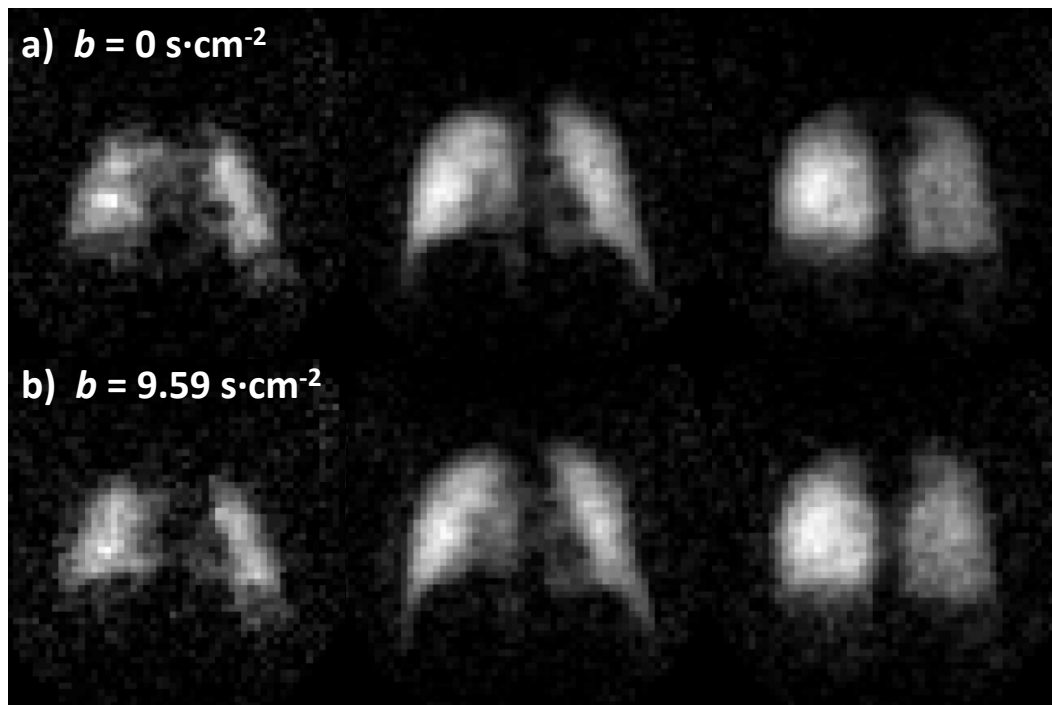


Figure 4-4: Three slices from ^{19}F 3D UTE lung imaging acquired in a healthy volunteer (a) without diffusion weighting ($b = 0 \text{ s}\cdot\text{cm}^{-2}$), and (b) with diffusion weighting ($b = 9.59 \text{ s}\cdot\text{cm}^{-2}$).

* Inert fluorinated gas ADC results are presented for one healthy volunteer only. This work was part of a study protocol that was approved by the local research ethics board and by Health Canada. This subject provided written informed consent prior to participating in this study

Each set of ^{19}F 3D UTE images shown in Figure 4-4 consisted of three slices; images without diffusion weighting ($b = 0 \text{ s}\cdot\text{cm}^{-2}$) are shown in the top row, and images with diffusion weighting ($b = 9.59 \text{ s}\cdot\text{cm}^{-2}$) are shown in the bottom row. In order to achieve a b value of $9.59 \text{ s}\cdot\text{cm}^{-2}$ and diffusion time of 1.5 ms, a TE of 3.8 ms was required. In this case, these settings yielded an SNR in the centre slice image of approximately 22 in the unweighted image and approximately 18 in the diffusion-weighted image.

The top row in Figure 4-5 shows the PFP ADC maps that were calculated using the diffusion-weighted ^{19}F 3D UTE images shown in Figure 4-4. ADC was calculated on a pixel-by-pixel basis using Eq. [4-4]. The histograms for each ADC map are shown in the bottom row in Figure 4-5.

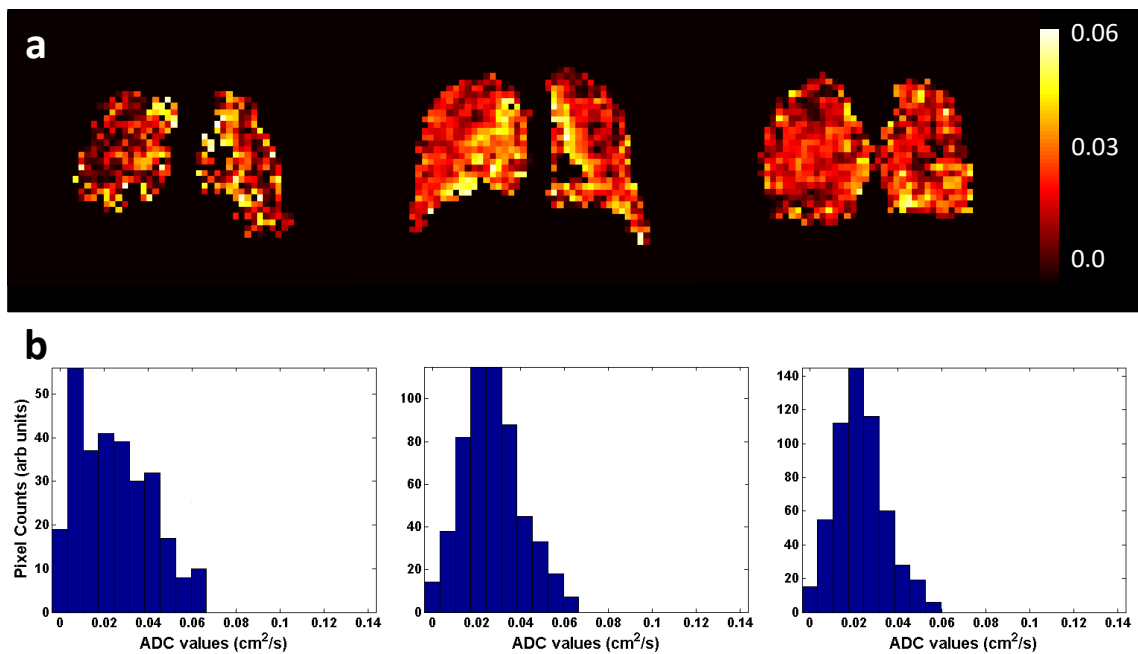


Figure 4-5: (a) PFP ADC maps measured in a healthy volunteer, and (b) the corresponding histograms for each slice.

The mean ADC values from each slice in Figure 4-5 were $0.034 \pm 0.021 \text{ cm}^2 \cdot \text{s}^{-1}$, $0.025 \pm 0.016 \text{ cm}^2 \cdot \text{s}^{-1}$, and $0.023 \pm 0.011 \text{ cm}^2 \cdot \text{s}^{-1}$, respectively, where the error represents the heterogeneity in each respective ADC map. These ADC results were similar to previously published values for the diffusion of PFP mixed with O₂ (16). This was to be expected for a diffusion time of 1 ms and the lightly restricted diffusion length scale that was probed. Assuming an ADC of $0.027 \text{ cm}^2 \cdot \text{s}^{-1}$ for PFP mixed with 21% O₂ (16), a length scale of approximately 0.16 mm will be probed in 1.5 ms, which is less than the diameter of an alveolus ($\sim 0.2 \text{ mm}$) (13). A longer diffusion time would be required to reach the restricted diffusion regime that is normally used for HP noble gas measurements of ADC. Since longer diffusion times necessitate long TEs, and the T₂^{*} of inert fluorinated gases may be prohibitively short, conventional restricted diffusion and lung morphometry measurements may not be possible with inert fluorinated gases (32).

However, by probing multiple diffusion times that are less than or on the order of T₂^{*}, it may be possible to measure the S/V ratio with inert fluorinated gases, which is an important biomarker of lung microstructure. In general, restriction causes the ADC to decrease as a function of diffusion time, as shown in Figure 4-6 (30). By acquiring 2 or more data points in the linear short time-scale regime, the slope from Figure 4-6 can be used to determine S/V according to the following equation (33):

$$\frac{D(t)}{D_0} \cong 1 - \left(\frac{4}{9\sqrt{\pi}} \right) \frac{S}{V} \sqrt{D_0 t}. \quad [4-5]$$

where $D(t)$ is the time-dependent ADC. It is also possible to mix inert fluorinated gases with other inert gases, such as ⁴He, to increase the free diffusivity, and hence the diffusion length scale that will be probed. Although there are a number of potential

difficulties, inert fluorinated gas diffusion measurements have been demonstrated in humans, and there is a possibility for probing the lung microstructure in humans with pulmonary diseases.

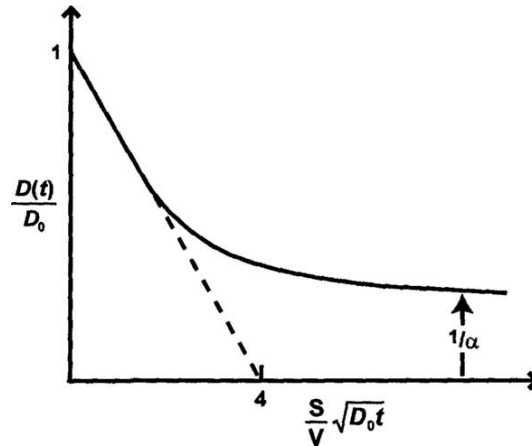


Figure 4-6: ADC normalized to the self-diffusion coefficient, $D(t)/D_0$, is shown plotted as a function of diffusion time, t . Note that the diffusion time is scaled in dimensionless units by making use of the free diffusion length scale and the surface-to-volume ratio (S/V). Image reproduced with permission (30).

4.4 Gravitational Distribution of Ventilation

4.4.1 Introduction

Functional ^{19}F MRI using inert fluorinated gases has already been established as a potentially valuable technique for pulmonary imaging, and the measurement of image-derived biomarkers can provide additional information regarding lung function. One such biomarker is the gradient in pulmonary ventilation, which is a well-known phenomenon that is caused by a gravitationally-dependent gradient in regional compliance. In order to support the weight of the lungs, the intrapleural pressure surrounding the lungs is less negative in dependent regions (i.e. regions of the lung that are closer to the ground),

which leads to a smaller resting volume. Thus, alveoli in dependent lung regions are on a steeper portion of the pressure-volume curve and they are easier to inflate (34). Therefore, ventilation is always greater in more dependent regions of the lung.

Gravitationally dependent gradients in ventilation have been previously demonstrated using a number of lung imaging techniques, including xenon-enhanced CT (Xe-CT) (35), O₂-enhanced ¹H MRI (36), and HP noble gas MRI (37,38). Although one study has investigated ventilation gradients in healthy rats using inert fluorinated gas MRI (3), a gravitational distribution of pulmonary ventilation has not been quantitatively demonstrated using ¹⁹F MRI in humans. In this brief study, ¹⁹F 3D UTE imaging was performed in healthy subjects with inert fluorinated gases, and anterior/posterior (A/P) ventilation gradients were measured (31,39).

4.4.2 Methods

This study protocol was approved by the local research ethics board and by Health Canada. All subjects provided written informed consent prior to their participation in this study. Imaging was performed using a 3.0 T scanner (Philips Achieva, Best, The Netherlands) and a flexible wrap-around quadrature transmit/receive coil tuned to the ¹⁹F resonance frequency of 120.15 MHz (Clinical MR Solutions). Six healthy volunteers (5 female, 1 male) were enrolled in this study with no previous history of lung disease and no previous history of smoking. The mean age of all subjects was 30 ± 13. Subjects were imaged in the supine position during a 15 second breath-hold following inhalation of a gas mixture of 79% PFP and 21% O₂ from a Tedlar bag.

For 4 subjects, ^{19}F 3D UTE MR images were acquired in the axial plane following a 1 L inhalation of the PFP/ O_2 mixture with the following settings: TR = 20 ms, TE = 0.2 ms, matrix = 64 x 64, 8 slices, 22 mm thickness, in-plane FOV = 450 x 450 mm², flip angle = 70°, and bandwidth = 140 Hz/pixel. For 2 subjects, ^{19}F 3D UTE MR images were acquired following continuous breathing from a 5 L bag of the PFP/ O_2 mixture, followed by a 1 L inhalation of the same mixture from a separate bag and 15 s breath-hold. For these 2 subjects only, 12 slices were acquired with a 15 mm thickness.

The resulting images were analyzed in Matlab R2011a using a custom-built graphical user interface (Mathworks, Natick, MA). Each slice in the 3D image was normalized such that all slices had similar noise levels. Next, a threshold was manually set to separate the lungs from the surrounding background and all slices were summed to create a single projection image of the entire lung in the axial plane. The signal intensity was then normalized to the maximum signal value in the 2D projection image. The mean signal intensity from the final projection image was then plotted as a function of distance from the most posterior edge of the lung, and the slope of a linear regression yielded the ventilation gradient.

4.4.3 Results and Discussion

Table 4-4 shows a summary of the measured ventilation gradients from all six healthy volunteers, along with the coefficients of determination (R^2), and percent changes in ventilation along the vertical direction. Qualitatively, there was no apparent difference between the ventilation gradients calculated for subjects that inhaled the PFP/ O_2 mixture

as a 1 L bolus (subjects 1 – 4) and subjects that inhaled the PFP/O₂ mixture using continuous breathing from a 5 L bag followed by a 1 L bolus inhalation and breath-hold (subjects 5 and 6).

Table 4-4: Summary of measured ventilation gradients, coefficients of determination (R^2), and percent changes in ventilation along the vertical direction for all six healthy volunteers. The first four volunteers inhaled the PFP/O₂ mixture as a 1 L bolus, and the last two volunteers inhaled the PFP/O₂ mixture using the continuous breathing method.

Subject #	Ventilation Gradient [cm^{-1}]	R^2	Percent Change [%]
1	-0.03058±0.00006	0.742	-75.4
2	-0.04107±0.00006	0.747	-81.2
3	-0.03315±0.00004	0.635	-80.4
4	-0.02259±0.00004	0.548	-66.6
5	-0.03759±0.00005	0.808	-76.6
6	-0.03325±0.00003	0.928	-84.2

Figure 4-7(a) shows one example of a whole lung axial projection image that was obtained from a representative ¹⁹F 3D UTE image that was acquired in the axial plane in subject #6. Figure 4-7(b) shows the signal intensity from the image shown in Figure 4-7(a) plotted as a function of vertical distance from the dorsal surface of the lung. The solid line in Figure 4-7(b) represents the calculated ventilation gradient, which has a slope of -0.033 cm^{-1} ; this gradient represents an 84% change in signal intensity from the posterior to anterior edges of the lung.

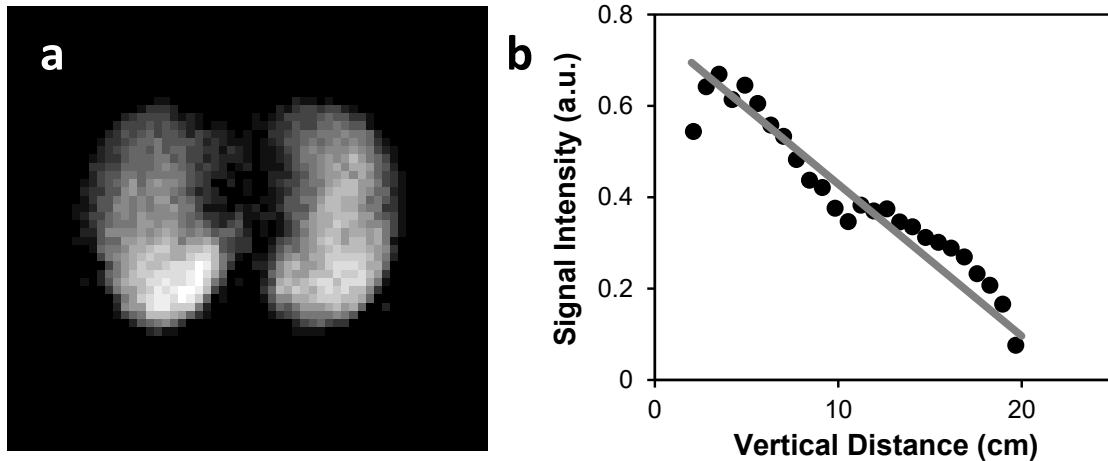


Figure 4-7: (a) Whole lung axial projection ^{19}F MR image acquired in a representative healthy volunteer. (b) Signal intensity as a function vertical distance in the lungs. The solid line represents the calculated gradient. Images were reproduced with permission (31).

Although this preliminary data appears to demonstrate the expected gradient in the ^{19}F signal, it is difficult to compare these results to literature values, which generally quantify fractional ventilation rather than analyze the ^{19}F signal distribution in static breath-hold images. Measuring fractional ventilation requires a wash-in and/or wash-out approach, where dynamic imaging is interleaved with breaths of the inhaled gas that provides signal contrast (i.e. wash-in) followed by breaths of room air (i.e. wash-out) (2,38,40). Therefore, imaging is able to capture the signal enhancement as the inhaled gas washes into and out of the lungs. Fractional ventilation can be determined by fitting the resulting data to a theoretical model, and then gradients in ventilation are calculated in the vertical direction.

It is also important to note that the results of this study might be confounded by B_1 inhomogeneity, which would lead to regional variations in the excitation flip angle. An extra calibration step is required in order to correct for the resulting signal intensity

variations in static breath-hold images (11); however corrections for B_1 inhomogeneity will not be required for fractional ventilation mapping. Since fractional ventilation mapping relies on the breath-to-breath signal changes during wash-in and/or wash-out, any regional variations in the baseline signal will not bias the results. Therefore, fractional ventilation mapping will provide a robust method for obtaining meaningful information regarding ventilation function.

4.4.4 Conclusions

This proof-of-concept study demonstrates that there is a clear gravitational distribution gradient of inert fluorinated gases in human lungs using ^{19}F 3D UTE MRI, and there is a potential for this technique to provide functional and regional information regarding lung physiology. Future work will explore the measurement of fractional ventilation mapping in humans using inert fluorinated gas MRI and a dynamic wash-in/wash-out approach, which will provide additional quantitative information related to the distribution of ventilation, gas kinetics, and air trapping. Furthermore, imaging in patients with pulmonary diseases will help to determine if ventilation gradients measured from dynamic inert fluorinated gas MRI can provide clinically relevant diagnostic information.

4.5 References

1. Kuethe DO, Caprihan A, Fukushima E, Waggoner RA. Imaging lungs using inert fluorinated gases. *Magn Reson Med* 1998;39(1):85-88.
2. Schreiber WG, Eberle B, Laukemper-Ostendorf S, Markstaller K, Weiler N, Scholz A, Burger K, Heussel CP, Thelen M, Kauczor HU. Dynamic 19F-MRI of pulmonary ventilation using sulfur hexafluoride (SF6) gas. *Magn Reson Med* 2001;45(4):605-613.
3. Ouriadov AV, Fox MS, Couch MJ, Li T, Ball IK, Albert MS. In vivo regional ventilation mapping using fluorinated gas MRI with an x-centric FGRE method. *Magn Reson Med* 2015;74(2):550-557.
4. Couch MJ, Ball IK, Li T, Fox MS, Littlefield SL, Biman B, Albert MS. Pulmonary ultrashort echo time 19F MR imaging with inhaled fluorinated gas mixtures in healthy volunteers: feasibility. *Radiology* 2013;269(3):903-909.
5. Halaweish AF, Moon RE, Foster WM, Soher BJ, McAdams HP, MacFall JR, Ainslie MD, MacIntyre NR, Charles HC. Perfluoropropane gas as a magnetic resonance lung imaging contrast agent in humans. *Chest* 2013;144(4):1300-1310.
6. Couch MJ, Ball IK, Li T, Fox MS, Biman B, Albert MS. Comparing Pulmonary MRI using Inert Fluorinated Gases and Hyperpolarized 3He: Is 19F MRI Good Enough? In *Proc 23rd Annual Meeting of ISMRM*, 2015. p 1501.
7. Kirby M, Heydari M, Svenningsen S, Wheatley A, McCormack DG, Etemad-Rezai R, Parraga G. Hyperpolarized 3He magnetic resonance functional imaging semiautomated segmentation. *Acad Radiol* 2012;19(2):141-152.
8. Charles HC, MacIntyre NR, Moon R, Foster WM, McAdams HP, Ainslie M. In-Vivo Visualization Of Slow To Fast Filling Compartments In Human Lungs Using 19F MRI Of Perfluorinated Gases Mixed With Oxygen. *Am Respir Crit Care Med* 2014;189:A4348.
9. Charles HC, Jones RW, Halaweish AF, Ainslie MD. Parallel Imaging for Short Breath Hold Times in Perfluorinated Gas Imaging of the Lung. In *In Proc 23rd Annual Meeting of ISMRM*, 2015. p 3984.
10. Kirby M, Svenningsen S, Owrangi A, Wheatley A, Farag A, Ouriadov A, Santyr GE, Etemad-Rezai R, Coxson HO, McCormack DG, Parraga G. Hyperpolarized 3He and 129Xe MR imaging in healthy volunteers and patients with chronic obstructive pulmonary disease. *Radiology* 2012;265(2):600-610.

11. Miller GW, Altes TA, Brookeman JR, De Lange EE, Mugler JP, 3rd. Hyperpolarized ^3He lung ventilation imaging with B1-inhomogeneity correction in a single breath-hold scan. *Magn Reson Mater Phy* 2004;16(5):218-226.
12. Einstein A. Über die von der molekularkinetischen Theorie der Wärme geforderte Bewegung von in ruhenden Flüssigkeiten suspendierten Teilchen. *Annalen der Physik* 1905;322(8):549-560.
13. Hansen JE, Ampaya EP. Human air space shapes, sizes, areas, and volumes. *J Appl Physiol* 1975;38(6):990-995.
14. Bassler PJ, Mattiello J, LeBihan D. Estimation of the Effective Self-Diffusion Tensor from the NMR Spin Echo. *J Magn Reson Ser B* 1994;103(3):247-254.
15. Tofts PS, Lloyd D, Clark CA, Barker GJ, Parker GJ, McConville P, Baldock C, Pope JM. Test liquids for quantitative MRI measurements of self-diffusion coefficient in vivo. *Magn Reson Med* 2000;43(3):368-374.
16. Chang YV, Conradi MS. Relaxation and diffusion of perfluorocarbon gas mixtures with oxygen for lung MRI. *J Magn Reson* 2006;181(2):191-198.
17. Moller HE, Chen XJ, Saam B, Hagspiel KD, Johnson GA, Altes TA, de Lange EE, Kauczor HU. MRI of the lungs using hyperpolarized noble gases. *Magn Reson Med* 2002;47(6):1029-1051.
18. Ruiz-Cabello J, Perez-Sanchez JM, Perez de Alejo R, Rodriguez I, Gonzalez-Mangado N, Peces-Barba G, Cortijo M. Diffusion-weighted ^{19}F -MRI of lung periphery: Influence of pressure and air-SF₆ composition on apparent diffusion coefficients. *Respir Physiol Neurobiol* 2005;148(1-2):43-56.
19. Parraga G, Ouriadov A, Evans A, McKay S, Lam WW, Fenster A, Etemad-Rezai R, McCormack D, Santyr G. Hyperpolarized ^3He ventilation defects and apparent diffusion coefficients in chronic obstructive pulmonary disease: preliminary results at 3.0 Tesla. *Invest Radiol* 2007;42(6):384-391.
20. Kaushik SS, Cleveland ZI, Cofer GP, Metz G, Beaver D, Nouis J, Kraft M, Auffermann W, Wolber J, McAdams HP, Driehuys B. Diffusion-weighted hyperpolarized ^{129}Xe MRI in healthy volunteers and subjects with chronic obstructive pulmonary disease. *Magn Reson Med* 2011;65(4):1154-1165.
21. Diaz S, Casselbrant I, Piitulainen E, Pettersson G, Magnusson P, Peterson B, Wollmer P, Leander P, Ekberg O, Akeson P. Hyperpolarized ^3He apparent diffusion coefficient MRI of the lung: reproducibility and volume dependency in healthy volunteers and patients with emphysema. *J Magn Reson Imaging* 2008;27(4):763-770.

22. Woods JC, Choong CK, Yablonskiy DA, Bentley J, Wong J, Pierce JA, Cooper JD, Macklem PT, Conradi MS, Hogg JC. Hyperpolarized ^3He diffusion MRI and histology in pulmonary emphysema. *Magn Reson Med* 2006;56(6):1293-1300.
23. Sukstanskii AL, Yablonskiy DA. Effects of restricted diffusion on MR signal formation. *J Magn Reson* 2002;157(1):92-105.
24. Yablonskiy DA, Sukstanskii AL, Leawoods JC, Gierada DS, Bretthorst GL, Lefrak SS, Cooper JD, Conradi MS. Quantitative in vivo assessment of lung microstructure at the alveolar level with hyperpolarized ^3He diffusion MRI. *Proc Natl Acad Sci U S A* 2002;99(5):3111-3116.
25. Yablonskiy DA, Sukstanskii AL, Woods JC, Gierada DS, Quirk JD, Hogg JC, Cooper JD, Conradi MS. Quantification of lung microstructure with hyperpolarized ^3He diffusion MRI. *J Appl Physiol* 2009;107(4):1258-1265.
26. Kirby M, Svenningsen S, Kanhere N, Owringi A, Wheatley A, Coxson HO, Santyr GE, Paterson NA, McCormack DG, Parraga G. Pulmonary ventilation visualized using hyperpolarized helium-3 and xenon-129 magnetic resonance imaging: differences in COPD and relationship to emphysema. *J Appl Physiol* 2013;114(6):707-715.
27. Perez-Sanchez JM, Perez de Alejo R, Rodriguez I, Cortijo M, Peces-Barba G, Ruiz-Cabello J. In vivo diffusion weighted ^{19}F MRI using SF_6 . *Magn Reson Med* 2005;54(2):460-463.
28. Carrero-Gonzalez L, Kaulisch T, Stiller D. In vivo diffusion-weighted MRI using perfluorinated gases: ADC comparison between healthy and elastase-treated rat lungs. *Magn Reson Med* 2013;70(6):1761-1764.
29. Conradi MS, Saam BT, Yablonskiy DA, Woods JC. Hyperpolarized ^3He and perfluorocarbon gas diffusion MRI of lungs. *Progr NMR Spectr* 2006;48:63-83.
30. Jacob RE, Chang YV, Choong CK, Bierhals A, Zheng Hu D, Zheng J, Yablonskiy DA, Woods JC, Gierada DS, Conradi MS. ^{19}F MR imaging of ventilation and diffusion in excised lungs. *Magn Reson Med* 2005;54(3):577-585.
31. Couch MJ, Ball IK, Li T, Fox MS, Ouriadov AV, Biman B, Albert MS. Inert fluorinated gas MRI: a new pulmonary imaging modality. *NMR Biomed* 2014;27(12):1525-1534.
32. Ouriadov A, Farag A, Kirby M, McCormack DG, Parraga G, Santyr GE. Lung morphometry using hyperpolarized (^{129}Xe) apparent diffusion coefficient anisotropy in chronic obstructive pulmonary disease. *Magn Reson Med* 2013;70(6):1699-1706.

33. Mitra PP, Sen PN, Schwartz LM. Short-time behavior of the diffusion coefficient as a geometrical probe of porous media. *Phys Rev B Condens Matter* 1993;47(14):8565-8574.
34. West JB. Regional differences in the lung. *Chest* 1978;74(4):426-437.
35. Lam WW, Holdsworth DW, Du LY, Drangova M, McCormack DG, Santyr GE. Micro-CT imaging of rat lung ventilation using continuous image acquisition during xenon gas contrast enhancement. *J Appl Physiol* 2007;103(5):1848-1856.
36. Sa RC, Cronin MV, Henderson AC, Holverda S, Theilmann RJ, Arai TJ, Dubowitz DJ, Hopkins SR, Buxton RB, Prisk GK. Vertical distribution of specific ventilation in normal supine humans measured by oxygen-enhanced proton MRI. *J Appl Physiol* 2010;109(6):1950-1959.
37. Mansson S, Deninger AJ, Magnusson P, Pettersson G, Olsson LE, Hansson G, Wollmer P, Golman K. ^3He MRI-based assessment of posture-dependent regional ventilation gradients in rats. *J Appl Physiol* 2005;98(6):2259-2267.
38. Couch MJ, Ouriadov A, Santyr GE. Regional ventilation mapping of the rat lung using hyperpolarized ^{129}Xe magnetic resonance imaging. *Magn Reson Med* 2012;68(5):1623-1631.
39. Couch MJ, Ball IK, Li T, Fox MS, Biman B, Albert MS. Gravitational Distribution Gradient of Inert Fluorinated Gases in Human Lungs Using ^{19}F Ultra-Short Echo Time MRI. In Proc 22nd Annual Meeting of ISMRM, 2014. p 2304.
40. Horn FC, Deppe MH, Marshall H, Parra-Robles J, Wild JM. Quantification of regional fractional ventilation in human subjects by measurement of hyperpolarized ^3He washout with 2D and 3D MRI. *J Appl Physiol* 2014;116(2):129-139.

Chapter 5

Fractional Ventilation Mapping using Inert Fluorinated Gas MRI in Rat Models of Inflammation and Fibrosis

5.1 Abstract

Purpose: The purpose of this study was to extend established methods for fractional ventilation mapping using ^{19}F MRI of inert fluorinated gases to rat models of pulmonary inflammation and fibrosis.

Methods: In this study, 5 rats were instilled with lipopolysaccharide (LPS) in the lungs two days prior to imaging, 6 rats were instilled with bleomycin in the lungs two weeks prior to imaging, and an additional 4 rats were used as controls. ^{19}F MR lung imaging was performed at 3T with rats continuously breathing a mixture of sulfur hexafluoride (SF_6) and O_2 . Fractional ventilation maps were obtained using a wash-out approach, by switching the breathing mixture to pure O_2 , and acquiring images following each successive wash-out breath.

Results: The mean fractional ventilation (r) was 0.29 ± 0.05 for control rats, 0.23 ± 0.10 for LPS-instilled rats and 0.19 ± 0.03 for bleomycin-instilled rats. Bleomycin-instilled rats had a significantly decreased mean r value compared to controls ($p = 0.010$).

Although LPS-instilled rats had a slightly reduced mean r value, this trend was not statistically significant ($p = 0.556$). Fractional ventilation gradients were calculated in the anterior/posterior (A/P) direction, and the mean A/P gradient was $-0.005 \pm 0.008 \text{ cm}^{-1}$ for control rats, $0.013 \pm 0.005 \text{ cm}^{-1}$ for LPS-instilled rats, and $0.009 \pm 0.018 \text{ cm}^{-1}$ for bleomycin-instilled rats. Fractional ventilation gradients were significantly different for control rats compared to LPS-instilled rats only ($p=0.016$). The ventilation gradients calculated from control rats showed the expected gravitational relationship, while ventilation gradients calculated from LPS- and bleomycin-instilled rats showed the opposite trend. Histology confirmed that LPS-instilled rats had a significantly elevated alveolar wall thickness, while bleomycin-instilled rats showed signs of substantial fibrosis.

Conclusion: Overall, ^{19}F MRI may be able to detect the effects of pulmonary inflammation and fibrosis using a simple and inexpensive imaging approach that can potentially be translated to humans.

5.2 Introduction

Interstitial lung disease (ILD) refers to a group of pulmonary disorders that are associated with inflammation and fibrosis in the interstitial tissues between the alveoli and capillary blood (1). In many cases the cause of ILD is unknown, and the prognosis is generally very poor. Animal models play an important role in helping to understand the causes and pathophysiology of ILD, and in particular, the instillation of lipopolysaccharide (LPS)

and bleomycin in rodent lungs have been established as models that produce inflammation that is similar to ILD. LPS is a cell wall component of Gram-negative bacteria, and the inflammatory response following LPS inhalation is associated with increased levels of neutrophils, cytokines and chemokines (2). Bleomycin is an antibiotic derived from *Streptomyces verticillus* and it has a long history of use as a chemotherapeutic agent (3). The inhalation of bleomycin causes an acute inflammatory response in the lungs that is followed by fibrosis (4).

Pre-clinical imaging of ILD models can potentially aid in the development of novel therapeutics and diagnostic techniques. Conventional proton (^1H) magnetic resonance imaging (MRI) has been shown to correlate with histology in LPS-instilled rodents, as areas of increased signal intensity correspond to a higher tissue density and the presence of inflammation (5,6). Similar results have been demonstrated in bleomycin-instilled rats (7) and decreases in ^1H MRI signal were detected following treatment with a glucocorticosteroid (8). Other work has suggested that the product of the ^1H signal intensity and the T_2 value is correlated with collagen content, and is therefore a potential biomarker for inflammation and fibrosis (9). The presence of pulmonary inflammation can also be detected using hyperpolarized (HP) noble gas MRI, since the injured and poorly ventilated regions of the lung appear as signal voids known as ventilation defects (10,11). Helium-3 (^3He) or xenon-129 (^{129}Xe) is initially polarized using spin-exchange optical pumping (SEOP) to enhance the MRI signal by up to 100,000 times above thermal equilibrium levels (12). Following inhalation, HP gas MRI is able to provide

high resolution images of the gas distribution and quantitative information related to lung function (13,14).

HP ^{129}Xe MRI is emerging as a particularly sensitive technique for studying LPS and bleomycin-induced inflammation. Following inhalation, xenon readily dissolves into blood and tissue, and the large chemical shift range of ^{129}Xe can be exploited to separately detect the HP ^{129}Xe in the lung airspaces, barrier tissues, and red blood cells (RBCs) (15-17). Time-resolved spectroscopy has been used to demonstrate a reduced ^{129}Xe RBC signal in bleomycin treated rats (18) and those treated with whole lung radiation (19), which was indicative of reduced gas exchange ability due to tissue barrier thickening. With the addition of theoretical models, dynamic ^{129}Xe measurements are able to detect differences in biomarkers such as the surface to volume ratio (S/V) and gas transfer times (20,21). Cleveland et al. recently demonstrated simultaneous imaging of the barrier and RBC ^{129}Xe signal in bleomycin treated rats, and the resulting images effectively visualized the distribution of fibrotic thickening (22).

Unfortunately, HP ^{129}Xe MRI is a technique that has certain disadvantages, which will make translation to routine clinical use difficult. HP ^{129}Xe MRI requires a polarizer and isotopically-enriched xenon gas, both of which contribute to large expenses that are necessary for imaging. One potential alternative to HP ^{129}Xe for functional lung imaging is ^{19}F MRI using inert fluorinated gases (23). Inert fluorinated gas MRI has the advantages of using gases that are nontoxic, abundant, and inexpensive compared to HP gases. Due to the large gyromagnetic ratio of ^{19}F , there is sufficient thermally polarized

signal for imaging at clinical field strengths, and averaging within a single breath-hold is possible due to short longitudinal relaxation times. Therefore, the gases do not need to be hyperpolarized prior to their use in MRI. Inert fluorinated gas MRI has recently been demonstrated in healthy volunteers (24), in patients with pulmonary diseases such as chronic obstructive pulmonary disease (COPD) and asthma, and in patients that received lung transplants (25).

Although human imaging with inert fluorinated gases is currently in the development phase, numerous animal studies have been performed using this technique since 1984 (26). Inert fluorinated gas MRI studies in animals have explored high resolution 3D imaging (27), as well as the measurement of functional biomarkers such as wash-in/wash-out kinetics (28), dynamic volume measurements (29), apparent diffusion coefficients (ADCs) (30,31), and ventilation/perfusion ratios (V/Q) (32,33). Ouriadov et al. recently performed a dynamic lung imaging study where fractional ventilation was measured using ^{19}F MRI in healthy rats that were ventilated with gas mixtures containing sulfur hexafluoride (SF_6) or perfluoropropane (C_3F_8 or PFP) (34). In the present study, we hypothesized that a similar dynamic inert fluorinated gas imaging approach would be able to detect the effects of inflammation and fibrosis in rat lungs. In order to test this hypothesis, rat lung imaging was performed using ^{19}F MRI of SF_6 in LPS- and bleomycin-instilled rats; fractional ventilation maps and ventilation gradients were quantitatively compared between inflammation rats and controls. To our knowledge, fractional ventilation mapping has not been previously performed using ^{19}F MRI in an animal model of lung disease.

5.3 Methods

5.3.1 Animal Preparation

This animal study followed specific animal use protocols approved by the local animal care committee of Lakehead University and the guidelines set forth by the Canadian Council on Animal Care (CCAC). A total of 15 male Sprague Dawley rats (340 ± 31 g, Charles River Laboratories, Saint-Constant, Canada) were imaged in this study. 5 rats were instilled with a dose of 2.5 mg/kg of LPS in the lungs two days prior to imaging (20), while an additional 6 rats were instilled with a dose of 2.5 mg/kg of bleomycin in the lungs 14 days (± 1 day) prior to imaging (18). At these time-points, the LPS model was expected to produce inflammation, while the bleomycin model was expected to produce fibrosis. For intratracheal instillations, the rats were anesthetized using 4.0–5.0% isoflurane (Abbott Laboratories, Saint-Laurent, Canada) and then instilled using a gavage needle and otoscope. In order to create an even distribution of the instilled agent, the rats were gently rotated before being returned to their cages for the prescribed duration. The remaining 4 rats were used as controls.

On the day of imaging, rats were initially anesthetized with 2.0–5.0% isoflurane and $60 \text{ mg}\cdot\text{kg}^{-1}$ ketamine (Baxter Corporation, Mississauga, Canada). A 26G catheter (Hospira, Lake Forest, IL) was placed in the tail vein and an intravenous injection of $3.0 \text{ mg}\cdot\text{kg}^{-1}$ propofol (Astra Zeneca, Mississauga, Canada) was delivered. Rats remained anesthetized by a continuous infusion of a 10:1 mixture of propofol and ketamine in the tail vein at a rate of $50 \text{ mg}\cdot\text{kg}^{-1}\cdot\text{h}^{-1}$. The trachea was exposed by blunt dissection, and a 14G catheter

(BD Angiocath, Sandy, UT) was inserted into the trachea through a small incision. Three loops of 2-0 silk suture (Surgical Specialties Corporation, Vancouver, Canada) were tied around the trachea to ensure an airtight seal. Rats were then ventilated in the supine position with a mixture of 80% sulfur hexafluoride (SF_6) and 20% O_2 using a custom-built MR-compatible ventilator (35). The breathing rate was set to $60 \text{ breaths} \cdot \text{min}^{-1}$ with a tidal volume of $8 \text{ mL} \cdot \text{kg}^{-1}$ and peak inspiratory pressure (PIP) of $20 \text{ cm H}_2\text{O}$. Body temperature was maintained using a heating pad, and a pulse oximetry sensor was taped to the hind paw to monitor blood oxygen saturation and heart rate.

5.3.2 MRI

All imaging in this study was performed at 3.0 T (Philips Achieva, Best, The Netherlands) using a custom-built linear dual-tuned $^1\text{H}/^{19}\text{F}$ transmit/receive birdcage coil (36). Conventional ^1H localizer images were initially acquired using a fast spin echo with the following settings: $\text{TR} = 2000 \text{ ms}$, $\text{TE} = 55 \text{ ms}$, $\text{FOV} = 75 \times 75 \text{ mm}^2$, $\text{matrix} = 256 \times 256$, $\text{FA} = 90^\circ$, $\text{BW} = 370 \text{ Hz pixel}^{-1}$, and 5 averages. Fractional ventilation maps were then obtained in the axial plane using the method of Ouriadov et al. (34). The breathing protocol for fractional ventilation mapping during the wash-out phase was as follows: after at least a 3 minute period of continuous breathing of the SF_6/O_2 mixture, the SF_6 concentration was assumed to be at a steady state in the lungs and a 10 s breath-hold was initiated for the acquisition of a baseline ^{19}F MR image. Breathing was then switched to pure O_2 for 9 consecutive breaths, and a 12 s breath-hold was initiated following each O_2 breath in order to acquire a series of wash-out images. After the wash-out series was complete, breathing was switched back to the SF_6/O_2 mixture.

During each breath-hold, a whole-lung 2D projection ^{19}F MR image was obtained in the axial plane using the x-centric pulse sequence (37). ^{19}F MR image acquisition used Cartesian sampling with the following settings: TR = 4 ms, TE = 0.48 ms, FOV = 75 x 75 mm², matrix = 64 x 64, FA = 70°, BW = 400 Hz pixel⁻¹, 65 averages, and partial echo factor = 0.505. Imaging was manually triggered at the beginning of each breath-hold. Since only half of k-space was collected during each wash-out series, the entire wash-out protocol was repeated using the opposite readout gradient polarity for later combination during post processing (34).

5.3.3 Data Analysis

In order to reconstruct a fully sampled k-space data set, two wash-out series with opposite readout gradient polarities were combined. For each line of k-space data in the readout direction, the half-echoes were phase corrected, any additional points prior to $k_x = 0$ were removed, and the two half-echoes were combined into a full echo. Fully sampled k-space data sets were then averaged three times. An exponential filter was applied just prior to the inverse Fourier transform in order to boost the signal-to-noise ratio (SNR) by a factor of approximately two. The baseline images were manually segmented in order to separate the lungs from the surrounding background and to create a binary mask, which was then applied to all ten images in the wash-out series. The whole-lung SNR was measured by dividing the mean signal in the segmented baseline image by the standard deviation from a background noise sample.

Following image segmentation, ventilation maps were calculated by fitting the final wash-out images on a pixel-by-pixel basis in Matlab R2011a (Mathworks, Natick, MA) with the following equation (34):

$$S(n) = \text{const} \cdot (1-r)^n, \quad [5-1]$$

where S is the available signal at breath number n , and r is the fractional ventilation parameter. r is defined as the volume of fresh gas (V_{new}) entering a volume at each breath, divided by the end inspiratory volume ($V_{total} = V_{old} + V_{new}$) (38):

$$r = \frac{V_{new}}{V_{total}} = \frac{V_{new}}{V_{old} + V_{new}}. \quad [5-2]$$

Fractional ventilation gradients were calculated in the anterior/posterior (A/P) direction (i.e. the vertical direction) from the resulting r maps in the axial plane. That is, 1D profiles were first formed by averaging rows of r map data. The 1D profiles were then fitted with a linear regression, and the slope of the regression yielded the fractional ventilation gradient. The mean r values and fractional ventilation gradients were compared between groups using a Wilcoxon rank sum test in GraphPad Prism (GraphPad Software, La Jolla, CA), where $p < 0.05$ was considered to be statistically significant.

5.3.4 Histology

Rats were euthanized at the end of the experiment using pentobarbital sodium (Schering Canada, Pointe-Claire, Canada). The rat lungs were excised postmortem and fixed in 10% neutral buffered formalin for a minimum of 72 hours. Six representative sections (upper, middle, and lower in each of the left and right lungs) were extracted and embedded in paraffin before being mounted on slides. One set of slides was stained with

hematoxylin and eosin (H&E), while another set of slides was stained with Masson's trichrome. The slides were then analyzed using a 40x objective, and representative photographs were taken at random locations.

The mean alveolar wall thickness was measured from H&E stains using ImageJ (NIH, Bethesda, MD) by overlaying a grid on top of the image and measuring the thickness of each alveolar wall crossing. Since collagen appears blue in trichrome stains, the amount of fibrosis can be quantified by thresholding the image. Trichrome stains were thresholded in ImageJ to produce a binary map, and the resulting maps were analyzed in Matlab to calculate the percent area that consists of fibrosis (22). The mean alveolar wall thicknesses and % fibrosis were compared between groups using a Wilcoxon rank sum test in GraphPad Prism, where $p < 0.05$ was considered to be statistically significant.

5.4 Results

Figure 5-1 shows representative conventional ^1H MR lung images that were obtained in the axial plane from a control rat (Rat #4), an LPS-instilled rat (Rat #8), and a bleomycin-instilled rat (Rat #12). Qualitatively, the ^1H images from the control rat and LPS-instilled rat appear to be normal, while the ^1H image from the bleomycin-treated rat has areas of increased signal intensity throughout the lungs.

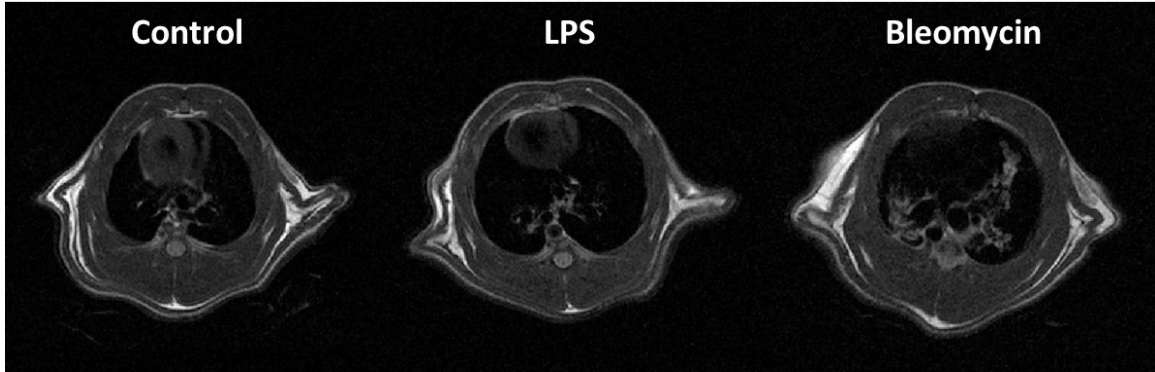


Figure 5-1: Representative conventional ^1H lung images obtained in the axial plane from a control rat (left), an LPS-instilled rat (middle), and a bleomycin-instilled rat (right).

Figure 5-2 shows three representative series of 2D whole-lung projection ^{19}F wash-out images that were obtained in the axial plane from the same rats that were shown in Figure 5-1. As expected, the baseline ^{19}F images have the highest possible SNR, while the subsequent O_2 wash-out images have a steadily decreasing SNR. The mean whole-lung SNR (\pm standard deviation) for the baseline images in Figure 5-2 was 19.8 ± 6.2 for the control rat, 29.8 ± 8.5 for the LPS-instilled rat, and 14.1 ± 5.6 for the bleomycin-instilled rat. In the control rat (Rat #4), the ^{19}F signal was essentially zero by the 5th O_2 wash-out breath, indicating that the gas in the lungs was completely replaced with O_2 . For the LPS-instilled rat (Rat #8), the ^{19}F signal was almost zero by the 6th - 7th wash-out breath, indicating that the SF_6 washout was slightly slower than in the control rat. For the bleomycin-instilled rat (Rat #12), the ^{19}F signal qualitatively appears to wash-out slower than both the control rat and the LPS-instilled rat.

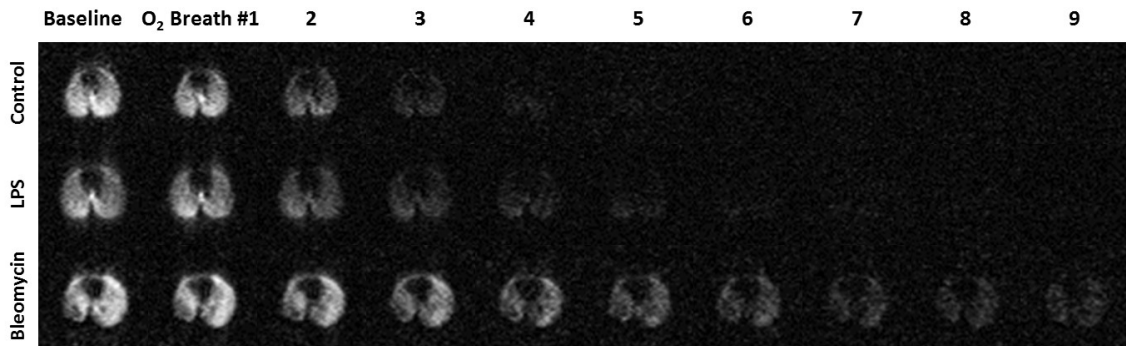


Figure 5-2: Representative series of 2D whole-lung projection ^{19}F wash-out images obtained in the axial plane from a control rat (top row), an LPS-instilled rat (middle row), and a bleomycin-instilled rat (bottom row).

Figure 5-3 shows three representative fractional ventilation maps that were obtained from the ^{19}F washout images shown in Figure 5-2. The mean r values for the fractional ventilation maps shown in Figure 5-3 were 0.32 ± 0.03 for the control rat, 0.31 ± 0.02 for the LPS-instilled rat, and 0.15 ± 0.04 for the bleomycin-instilled rat. The error represents the standard deviation of the r map, which in turn reflects the heterogeneity of the r map.

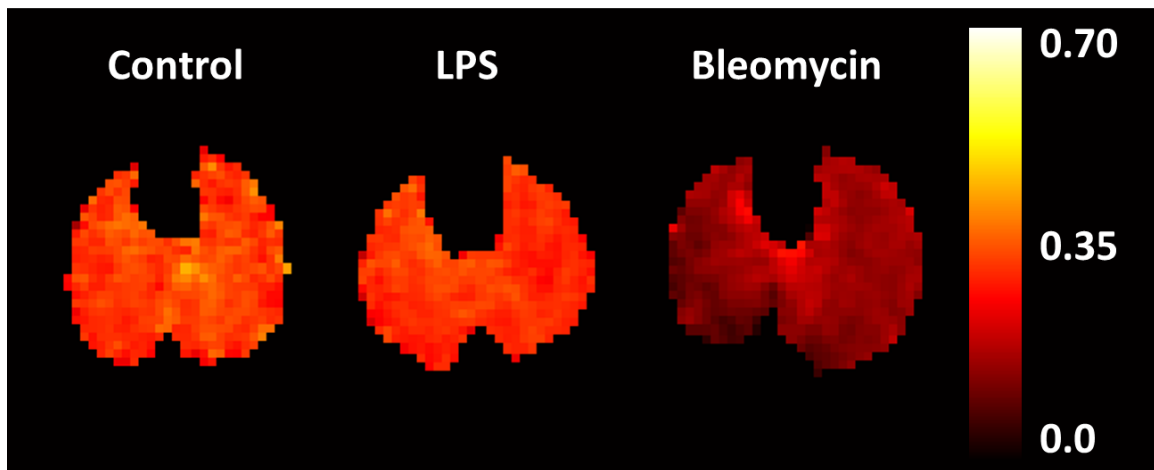


Figure 5-3: Representative fractional ventilation maps obtained in the axial plane from a control rat (left), an LPS-instilled rat (middle), and a bleomycin-instilled rat (right).

Table 5-1 shows the fractional ventilation values calculated for all 15 rats, and these results are shown graphically in Figure 5-4. The mean r value for all control rats was 0.29 ± 0.05 , while the mean r value for all LPS-instilled rats was 0.23 ± 0.10 , and the mean r value for all bleomycin-instilled rats was 0.19 ± 0.03 .

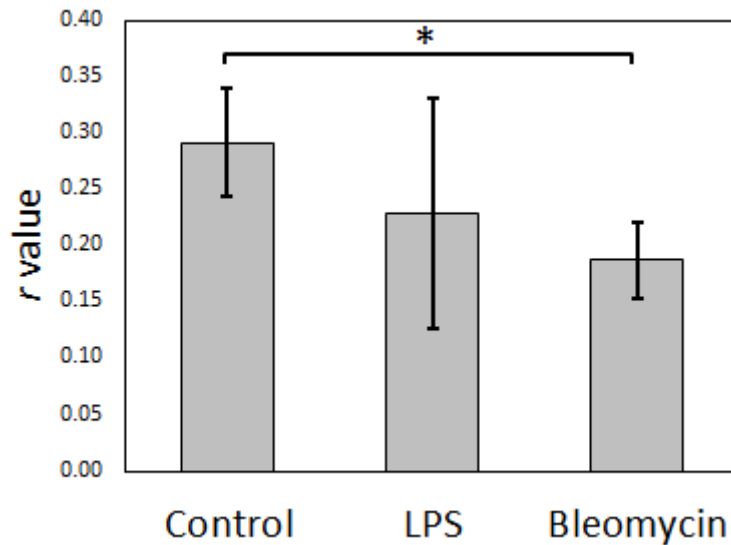


Figure 5-4: Comparison of mean r values from all rats in this study. The r values were only significantly different for bleomycin-instilled rats compared to controls ($p = 0.001$).

Overall, there was a trend towards decreased r values in LPS-instilled rats compared to controls, however, this trend was not statistically significant ($p = 0.556$). On the other hand, the mean r values in bleomycin-instilled rats were significantly decreased compared to controls ($p = 0.001$), but statistically indistinguishable from the LPS-instilled group ($p = 0.699$).

Table 5-1: Summary of the mean r values and fractional ventilation gradients from all rats in this study.

Rat No.	Group	Mass [g]	Mean r value	Ventilation Gradient [cm^{-1}]
1	Control	360	0.27 ± 0.03	-0.00294 ± 0.00003
2	Control	386	0.34 ± 0.02	-0.00113 ± 0.00003
3	Control	348	0.24 ± 0.03	-0.01695 ± 0.00005
4	Control	311	0.32 ± 0.03	0.00089 ± 0.00009
5	LPS	344	0.12 ± 0.03	0.01168 ± 0.00001
6	LPS	377	0.28 ± 0.03	0.02082 ± 0.00003
7	LPS	318	0.12 ± 0.02	0.00809 ± 0.00004
8	LPS	307	0.31 ± 0.02	0.01115 ± 0.00002
9	LPS	365	0.32 ± 0.03	0.01572 ± 0.00002
10	Bleomycin	383	0.21 ± 0.04	-0.02079 ± 0.00008
11	Bleomycin	296	0.14 ± 0.03	0.02469 ± 0.00003
12	Bleomycin	344	0.15 ± 0.04	0.01917 ± 0.00002
13	Bleomycin	343	0.22 ± 0.03	0.02519 ± 0.00003
14	Bleomycin	295	0.22 ± 0.04	0.00933 ± 0.00005
15	Bleomycin	319	0.18 ± 0.05	-0.00414 ± 0.00009

Figure 5-5 shows three representative fractional ventilation gradients calculated in the A/P (i.e. vertical) direction from a control rat (Rat #3), an LPS-instilled rat (Rat #8), and a bleomycin-instilled rat (Rat #12). In the control rat, fractional ventilation decreased as a function of vertical distance in the lungs, leading to a negative ventilation gradient. The LPS-instilled rat in Figure 5-5 showed the opposite trend, where ventilation increased as a function of vertical distance in the lungs and the ventilation gradient was positive. In this case, the mean r value from the LPS-instilled rat was slightly higher than the mean r value from the control rat. The bleomycin-instilled rat in Figure 5-5 also showed a positive ventilation gradient trend, similar to the LPS-instilled rat; however, the intercept of the linear regression was much lower than the LPS-instilled case.

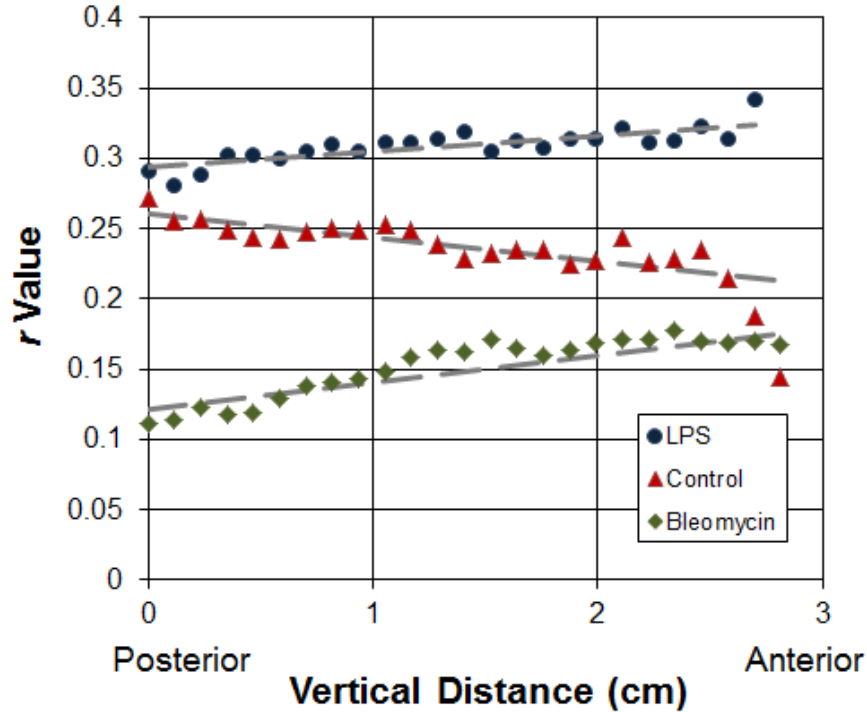


Figure 5-5: Representative fractional ventilation gradients calculated in the anterior/posterior (A/P) direction from a control rat (triangles), an LPS-instilled rat (circles), and a bleomycin-instilled rat (diamonds).

Table 5-1 also summarizes the fractional ventilation gradients calculated for all 15 rats in this study, and these results are shown graphically in Figure 5-6. Overall, there was a statistically significant difference between fractional ventilation gradients calculated from control rats compared to LPS-instilled rats ($p = 0.016$). The mean fractional ventilation gradient was $-0.005 \pm 0.008 \text{ cm}^{-1}$ for control rats, $0.013 \pm 0.005 \text{ cm}^{-1}$ for LPS-instilled rats, and $0.009 \pm 0.018 \text{ cm}^{-1}$ for bleomycin-instilled rats. Although the ventilation gradients for bleomycin-instilled rats were generally positive, there was a large variability between rats, and therefore the ventilation gradients were not statistically different from LPS-instilled rats ($p = 0.699$) or controls ($p = 0.352$).

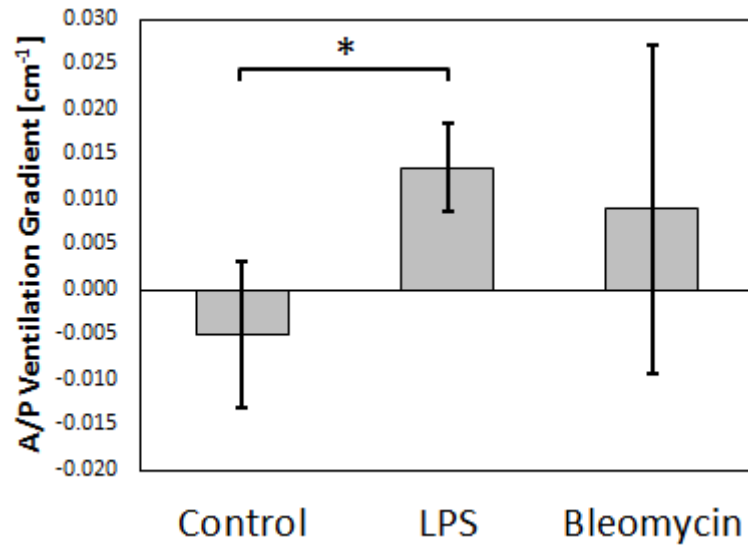


Figure 5-6: Comparison of A/P ventilation gradients from all rats in this study. The ventilation gradients were only significantly different for LPS-instilled rats compared to controls ($p = 0.016$).

Figure 5-7 shows representative H&E-stained micrographs imaged using a 40x objective from a control rat (Rat #1), an LPS-instilled rat (Rat #8), and a bleomycin-instilled rat (Rat #12). In this case, the alveolar wall thickness was noticeably thickened compared to controls in both the LPS- and bleomycin-instilled rats.

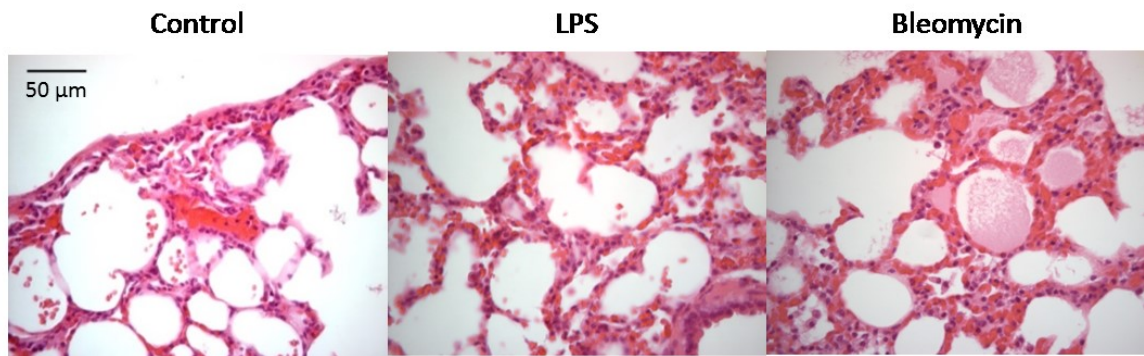


Figure 5-7: Representative H&E-stained micrographs obtained from a control rat (left), and LPS-instilled rat (middle), and a bleomycin-instilled rat (right) imaged using a 40x objective.

Table 5-2 summarizes the mean alveolar wall thickness for all rats in this study, and these results are shown graphically in Figure 5-8. The mean alveolar wall thickness was $5.6 \pm 1.9 \mu\text{m}$ for control rats, $10.0 \pm 2.2 \mu\text{m}$ for LPS-instilled rats, and $9.1 \pm 3.9 \mu\text{m}$ for bleomycin-instilled rats.

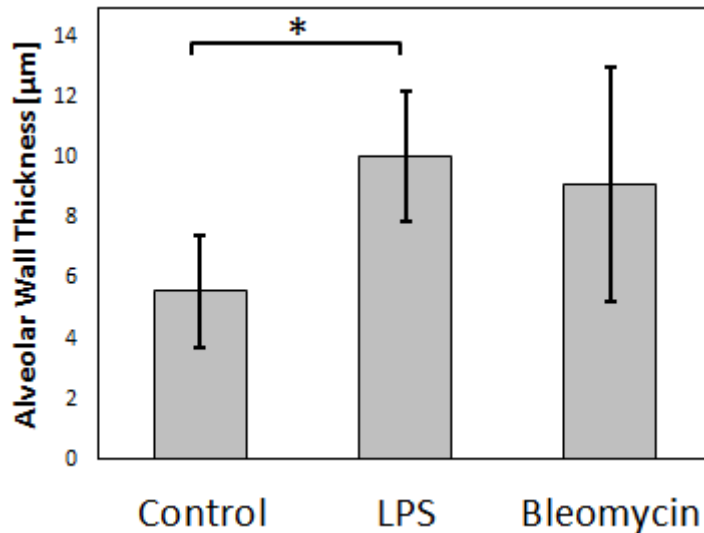


Figure 5-8: Comparison of the mean alveolar wall thickness from all rats in this study. The alveolar wall thickness was significantly different for LPS-instilled rats compared to controls ($p = 0.032$).

Overall, there was a statistically significant difference between the control and LPS-instilled rats ($p = 0.032$). The error associated with the alveolar wall thicknesses in Table 5-2 represents the standard deviation of measurements in the six representative tissue sections. Although the alveolar wall thickness was generally elevated in bleomycin-instilled rats, the wall thickness was not statistically different from LPS-instilled rats ($p = 0.432$) or controls ($p = 0.257$).

Table 5-2: Summary of the mean alveolar wall thickness and fraction of collagen content from all rats in this study.

Rat No.	Group	Alveolar Wall Thickness [μm]	% Fibrosis
1	Control	4.6 ± 0.6	0.46
2	Control	3.4 ± 0.2	0.99
3	Control	6.7 ± 1.5	0.60
4	Control	7.5 ± 1.5	1.05
5	LPS	11.0 ± 2.3	0.69
6	LPS	12.0 ± 3.1	4.06
7	LPS	8.8 ± 1.2	1.61
8	LPS	11.5 ± 4.4	2.31
9	LPS	6.8 ± 0.5	0.12
10	Bleomycin	13.5 ± 5.8	19.74
11	Bleomycin	7.2 ± 0.9	4.16
12	Bleomycin	14.6 ± 6.4	19.09
13	Bleomycin	5.8 ± 1.4	6.68
14	Bleomycin	7.2 ± 12.8	7.56
15	Bleomycin	6.2 ± 11.2	3.42

Figure 5-9 shows representative trichrome-stained micrographs obtained using a 40x objective from a control rat (Rat #3), an LPS-instilled rat (Rat #7), and a bleomycin rat (Rat #12). The blue areas in Figure 5-9 indicate that there was substantial fibrosis in the bleomycin-instilled rat compared to both the LPS-instilled rat and the control.

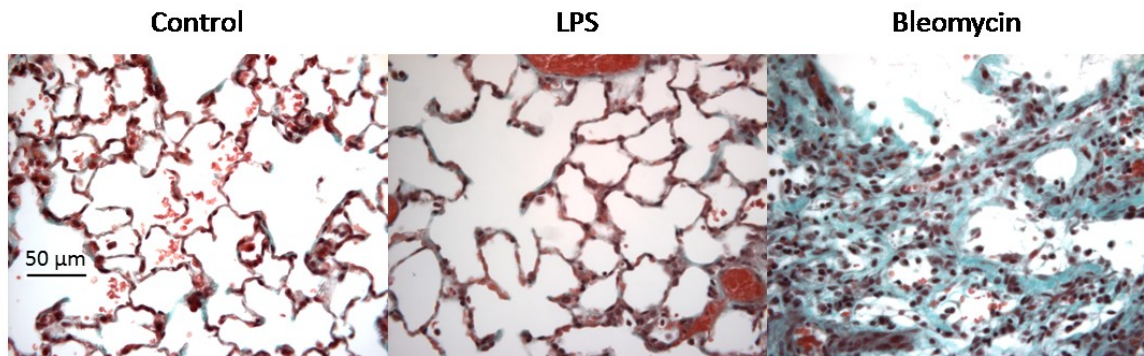


Figure 5-9: Representative trichrome-stained micrographs obtained from a control rat (left), and LPS-instilled rat (middle), and a bleomycin-instilled rat (right) imaged using a 40x objective.

Table 5-2 also summarizes the percent area containing fibrosis for all rats in this study, and these results are shown graphically in Figure 5-10. The mean area containing collagen was 0.77 ± 0.29 % for control rats, 1.8 ± 1.5 % for LPS-instilled rats, and 9.2 ± 8.1 % for bleomycin-instilled rats. The bleomycin-instilled rats had a significantly greater amount of fibrosis compared to both LPS-instilled rats ($p = 0.009$) and controls ($p = 0.010$). On the other hand, the percent area containing fibrosis was not statistically different between LPS-instilled rats and controls ($p = 0.413$).

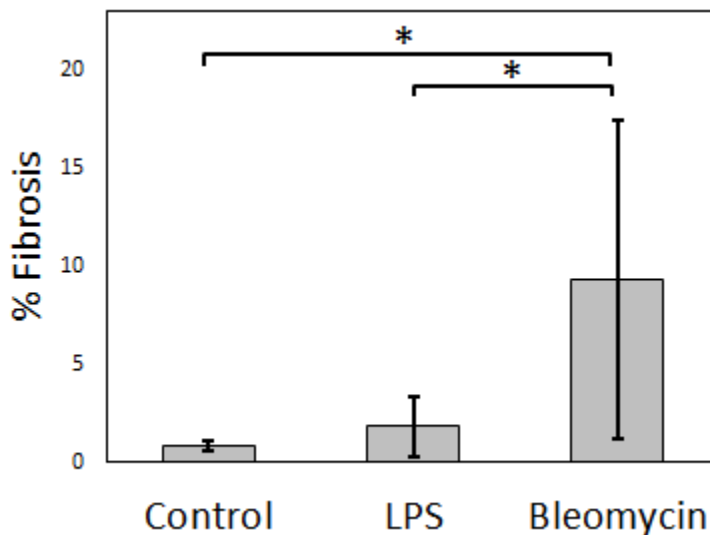


Figure 5-10: Comparison of the fraction of collagen content for all rats in this study. The collagen content was significantly different for bleomycin-instilled rats compared to both LPS-instilled rats ($p = 0.009$) and controls ($p = 0.010$).

5.5 Discussion

This study demonstrates for the first time, dynamic ^{19}F MRI of inert fluorinated gases in rat models of pulmonary inflammation and fibrosis. Fractional ventilation mapping, performed using SF_6 in this study, was able to provide quantitative information that was related to lung function, and gradients in ventilation were able to provide insight into the

regional distribution of ventilation. The mean r values from control rats in this study agreed with expectations based on the known ventilator settings and expected lung size [TV = 8 mL/kg, FRC = 8 mL, $r = TV / (TV + FRC) = 0.25$]. The results from control rats were also consistent with fractional ventilation mapping techniques that have been reported in animals using xenon-enhanced computed tomography (Xe-CT) (39,40), HP noble gas MRI (38,41-43), and inert fluorinated gas MRI (34). The mean r values in LPS-instilled rats were somewhat less than the control rats, but not significantly different from the control group. On the other hand, the mean r values in bleomycin-instilled rats were less than both the controls and LPS-instilled rats, but only significantly different from the control rats. Similarly, reduced fractional ventilation values were observed in a study involving fractional ventilation mapping using HP ^3He MRI in bleomycin-instilled rats, and it was suggested that a decrease in lung compliance was a major factor in diminishing alveolar expansion and ventilation (44).

The fractional ventilation gradients from control rats agreed with expectations from the literature, where rats in the supine position had a greater ventilation in more dependent regions of the lung (34). As discussed in Section 4.4.1, there is a gravitational gradient in lung compliance that leads to the well-known gradient in ventilation (45). This relationship in ventilation distribution has been previously demonstrated with a variety of imaging techniques, such as Xe-CT (40), O₂-enhanced ^1H MRI (46), HP noble gas MRI (41,47) and inert fluorinated gas MRI (34). The mean fractional ventilation gradients from LPS- and bleomycin-instilled rats had a positive slope, and this result might be explained by a decrease in lung compliance in dependent regions of the lung due to the

presence of inflammation and fibrosis. On the other hand, the variability in the fractional ventilation gradients in LPS- and bleomycin-instilled rats may also be explained by heterogeneity in the distribution of the instilled agent, which would lead to disruptions in normal fractional ventilation gradients.

This work made use of a linear dual-tuned $^1\text{H}/^{19}\text{F}$ transmit/receive birdcage coil (36), so that conventional ^1H MRI and inert fluorinated gas MRI could be performed without moving the animal. Although, the SNR will theoretically be a factor of $\sqrt{2}$ less than the quadrature ^{19}F birdcage coil used by Ouriadov et al. (34) (assuming all parameters are equal), the ability to acquire high quality conventional ^1H MR images provides an important baseline for comparison. For example, the conventional ^1H MR images acquired in this study suggested that there was substantial fibrosis throughout the lungs of bleomycin-instilled rats; however, these images do not provide information related to changes in gas replacement inside the lungs. Furthermore, the conventional ^1H MR images from the LPS-instilled rats appeared to be very similar to the control rats, insofar as there was little ^1H signal inside the lungs other than blood vessels. On the other hand, fractional ventilation mapping was able to demonstrate changes in ventilation gradients in the LPS-instilled rats. Future work will investigate the use of a quadrature dual-tuned $^1\text{H}/^{19}\text{F}$ transmit/receive birdcage coil.

It is also interesting to note that the ^{19}F images presented in this study were able to visualize the major airways slightly better than the images presented by Ouriadov et al. (34), which is likely due to the use of a slightly shorter TE (0.48 ms compared to 0.54

ms). Although an r value close to unity would be expected in the major airways, the control rats in this study had an r value of approximately 0.45 in the major airways. Ouriadov et al. estimated that the T_2^* in the major airways was as short as 0.5 ms, while the T_2^* in the lung parenchyma was expected to be approximately 1 ms. Thus, the very short T_2^* explains the relatively poor visualization of the major airways.

The alveolar wall thickness measurements from control rats in this study were similar to morphological measurements reported in the literature (48). As expected, the LPS- and bleomycin-instilled rats generally had increased alveolar wall thicknesses, which led to impaired gas exchange and reduced ventilation. Histological measurements of the collagen content confirmed that the bleomycin model produced diffuse fibrosis, especially surrounding airways and vessels, whereas after 2 days the LPS model produced substantial wall thickening with no noticeable fibrosis. Furthermore, it is interesting to note that the fibrosis produced in the bleomycin model led to significant changes in fractional ventilation, whereas the inflammation produced in the LPS model led to significant changes in ventilation gradients. Future work will determine if fractional ventilation mapping can be used to differentiate between inflammation and fibrosis.

Fractional ventilation mapping using ^{19}F MRI has potential limitations compared to HP ^{129}Xe MRI techniques. Since inert fluorinated gases have a very low available magnetization compared to HP gases, efficient acquisition strategies, such as x-centric (34,37) are required in order to compensate for the low thermally polarized signal. In this

study, the use of x-centric imaging provided a short TE and short acquisition window, and the final images had minimal blurring and reconstruction artifacts. Since inert fluorinated gases have a very low solubility (49), this technique mainly yields information related to alveolar ventilation. Although V/Q mapping has been demonstrated in animals using T_1 mapping of inert fluorinated gases (33), it remains to be seen how feasible T_1 mapping will be in humans. Therefore, HP ^{129}Xe MRI may be a more sensitive technique for detecting inflammation and ILD due to the ability to probe ^{129}Xe in the dissolved phase. However, this study demonstrates that changes in lung function due to inflammation and fibrosis can be detected using ^{19}F MRI of inert fluorinated gases, and this technique is inexpensive compared to HP gases. That is, inert fluorinated gases do not require an expensive polarizer, and the source gases cost approximately \$20 per litre, compared to \$200 per litre for enriched ^{129}Xe (50). Other ^{19}F MRI techniques have also been used to detect the presence of inflammation induced by LPS, such as using injected perfluorocarbons (PFCs) (51). The use of injected PFCs may in fact complement the inert fluorinated gas fractional ventilation mapping technique used in this study, since the PFCs are able to directly localize the site of inflammation in tissue, while the ventilation mapping is able to provide additional quantitative information with respect to changes in lung function.

Ventilation mapping has recently been performed in humans using HP ^3He MRI, and the expected gravitational gradient in fractional ventilation was observed (52). Furthermore, altered distributions of fractional ventilation have recently been observed using HP ^3He MRI in patients cystic fibrosis and asthma (53). It should also be possible to measure

fractional ventilation in humans using a ^{19}F MRI technique similar to the animal imaging in this study, where dynamic ^{19}F MR imaging is performed during consecutive breaths of a fluorinated gas mixture that contains at least 21% O_2 . Preliminary efforts to quantify inert fluorinated gas wash-in and wash-out time constants using ^{19}F MRI are currently underway in healthy volunteers and patients with COPD (54,55), and these results appear to be promising. Continuing this work will help to determine if fractional ventilation mapping obtained using ^{19}F MRI of inert fluorinated gases in humans can provide meaningful and functional information regarding lung physiology and the gravitational distribution of ventilation in the lungs.

5.6 Conclusion

Fractional ventilation mapping using ^{19}F MRI of inert fluorinated gases was successfully performed in two models of pulmonary inflammation in rats. The detection of reduced fractional ventilation and altered ventilation gradients in LPS- and bleomycin-instilled rats demonstrates the potential for using inert fluorinated gas MRI to detect the effects of inflammation and fibrosis on lung function using a simple and inexpensive approach. The fact that an expensive polarizer and scarce noble gas isotopes are not required will make clinical translation very attractive. This technique may help to provide clinicians with diagnostic information that can aid in decision making for respiratory diseases such as ILD.

5.7 References

1. Saag KG, Kline JN. Interstitial Lung Diseases. In: Baum GL, Crapo JD, Celli BR, Karlinsky JB, editors. Textbook of Pulmonary Diseases. 6th Edition. Philadelphia, PA: Lippincott-Raven; 1998. p 341-365.
2. Brass DM, Savov JD, Gavett SH, Haykal-Coates N, Schwartz DA. Subchronic endotoxin inhalation causes persistent airway disease. *Am J Physiol Lung Cell Mol Physiol* 2003;285(3):L755-761.
3. Blum RH, Carter SK, Agre K. A clinical review of bleomycin--a new antineoplastic agent. *Cancer* 1973;31(4):903-914.
4. Izbicki G, Segel MJ, Christensen TG, Conner MW, Breuer R. Time course of bleomycin-induced lung fibrosis. *Int J Exp Pathol* 2002;83(3):111-119.
5. Conti G, Tambalo S, Villetti G, Catinella S, Carnini C, Bassani F, Sonato N, Sbarbati A, Marzola P. Evaluation of lung inflammation induced by intratracheal administration of LPS in mice: comparison between MRI and histology. *Magn Reson Mater Phy* 2010;23(2):93-101.
6. Beckmann N, Tigani B, Sugar R, Jackson AD, Jones G, Mazzoni L, Fozard JR. Noninvasive detection of endotoxin-induced mucus hypersecretion in rat lung by MRI. *Am J Physiol Lung Cell Mol Physiol* 2002;283(1):L22-30.
7. Karmouty-Quintana H, Cannet C, Zurbruegg S, Ble FX, Fozard JR, Page CP, Beckmann N. Bleomycin-induced lung injury assessed noninvasively and in spontaneously breathing rats by proton MRI. *J Magn Reson Imaging* 2007;26(4):941-949.
8. Babin AL, Cannet C, Gerard C, Wyss D, Page CP, Beckmann N. Noninvasive assessment of bleomycin-induced lung injury and the effects of short-term glucocorticosteroid treatment in rats using MRI. *J Magn Reson Imaging* 2011;33(3):603-614.
9. Jacob RE, Amidan BG, Soelberg J, Minard KR. In vivo MRI of altered proton signal intensity and T2 relaxation in a bleomycin model of pulmonary inflammation and fibrosis. *J Magn Reson Imaging* 2010;31(5):1091-1099.
10. Olsson LE, Smailagic A, Onnervik PO, Hockings PD. (1)H and hyperpolarized (3)He MR imaging of mouse with LPS-induced inflammation. *J Magn Reson Imaging* 2009;29(4):977-981.
11. Thomas AC, Nouls JC, Driehuys B, Voltz JW, Fubara B, Foley J, Bradbury JA, Zeldin DC. Ventilation defects observed with hyperpolarized 3He magnetic

- resonance imaging in a mouse model of acute lung injury. *Am J Respir Cell Mol Biol* 2011;44(5):648-654.
12. Walker TG, Happer W. Spin-exchange optical pumping of noble-gas nuclei. *Rev Mod Phys* 1997;69(2):629-642.
 13. Albert MS, Cates GD, Driehuys B, Happer W, Saam B, Springer CS, Jr., Wishnia A. Biological magnetic resonance imaging using laser-polarized ^{129}Xe . *Nature* 1994;370(6486):199-201.
 14. Couch MJ, Blasiak B, Tomanek B, Ouriadov AV, Fox MS, Dowhos KM, Albert MS. Hyperpolarized and Inert Gas MRI: The Future. *Mol Imaging Biol* 2015;17(2):149-162.
 15. Kaushik SS, Freeman MS, Cleveland ZI, Davies J, Stiles J, Virgincar RS, Robertson SH, He M, Kelly KT, Foster WM, McAdams HP, Driehuys B. Probing the regional distribution of pulmonary gas exchange through single-breath gas- and dissolved-phase ^{129}Xe MR imaging. *J Appl Physiol* 2013;115(6):850-860.
 16. Kaushik SS, Robertson SH, Freeman MS, He M, Kelly KT, Roos JE, Rackley CR, Foster WM, McAdams HP, Driehuys B. Single-breath clinical imaging of hyperpolarized Xe in the airspaces, barrier, and red blood cells using an interleaved 3D radial 1-point Dixon acquisition. *Magn Reson Med* 2015.
 17. Qing K, Ruppert K, Jiang Y, Mata JF, Miller GW, Shim YM, Wang C, Ruset IC, Hersman FW, Altes TA, Mugler JP, 3rd. Regional mapping of gas uptake by blood and tissue in the human lung using hyperpolarized xenon-129 MRI. *J Magn Reson Imaging* 2014;39(2):346-359.
 18. Driehuys B, Cofer GP, Pollaro J, Mackel JB, Hedlund LW, Johnson GA. Imaging alveolar-capillary gas transfer using hyperpolarized ^{129}Xe MRI. *Proc Natl Acad Sci U S A* 2006;103(48):18278-18283.
 19. Fox MS, Ouriadov A, Thind K, Hegarty E, Wong E, Hope A, Santyr GE. Detection of radiation induced lung injury in rats using dynamic hyperpolarized (^{129}Xe) magnetic resonance spectroscopy. *Med Phys* 2014;41(7):072302.
 20. Mansson S, Wolber J, Driehuys B, Wollmer P, Golman K. Characterization of diffusing capacity and perfusion of the rat lung in a lipopolysaccharide disease model using hyperpolarized ^{129}Xe . *Magn Reson Med* 2003;50(6):1170-1179.
 21. Abdeen N, Cross A, Cron G, White S, Rand T, Miller D, Santyr G. Measurement of xenon diffusing capacity in the rat lung by hyperpolarized ^{129}Xe MRI and dynamic spectroscopy in a single breath-hold. *Magn Reson Med* 2006;56(2):255-264.

22. Cleveland ZI, Virgincar RS, Qi Y, Robertson SH, Degan S, Driehuys B. 3D MRI of impaired hyperpolarized (^{129}Xe) uptake in a rat model of pulmonary fibrosis. *NMR Biomed* 2014;27(12):1502-1514.
23. Couch MJ, Ball IK, Li T, Fox MS, Ouriadov AV, Biman B, Albert MS. Inert fluorinated gas MRI: a new pulmonary imaging modality. *NMR Biomed* 2014;27(12):1525-1534.
24. Couch MJ, Ball IK, Li T, Fox MS, Littlefield SL, Biman B, Albert MS. Pulmonary ultrashort echo time ^{19}F MR imaging with inhaled fluorinated gas mixtures in healthy volunteers: feasibility. *Radiology* 2013;269(3):903-909.
25. Halaweish AF, Moon RE, Foster WM, Soher BJ, McAdams HP, MacFall JR, Ainslie MD, MacIntyre NR, Charles HC. Perfluoropropane gas as a magnetic resonance lung imaging contrast agent in humans. *Chest* 2013;144(4):1300-1310.
26. Rinck PA, Petersen SB, Lauterbur PC. NMR-Imaging von fluorhaltigen Substanzen. ^{19}F -Fluor-Ventilations- und -Perfusionsdarstellungen. *Fortschr Röntgenstr* 1984;140(3):239-243.
27. Kuethe DO, Caprihan A, Fukushima E, Waggoner RA. Imaging lungs using inert fluorinated gases. *Magn Reson Med* 1998;39(1):85-88.
28. Schreiber WG, Eberle B, Laukemper-Ostendorf S, Markstaller K, Weiler N, Scholz A, Burger K, Heussel CP, Thelen M, Kauczor HU. Dynamic ^{19}F -MRI of pulmonary ventilation using sulfur hexafluoride (SF_6) gas. *Magn Reson Med* 2001;45(4):605-613.
29. Kuethe DO, Behr VC, Begay S. Volume of rat lungs measured throughout the respiratory cycle using ^{19}F NMR of the inert gas SF_6 . *Magn Reson Med* 2002;48(3):547-549.
30. Jacob RE, Chang YV, Choong CK, Bierhals A, Zheng Hu D, Zheng J, Yablonskiy DA, Woods JC, Gierada DS, Conradi MS. ^{19}F MR imaging of ventilation and diffusion in excised lungs. *Magn Reson Med* 2005;54(3):577-585.
31. Perez-Sanchez JM, Perez de Alejo R, Rodriguez I, Cortijo M, Peces-Barba G, Ruiz-Cabello J. In vivo diffusion weighted ^{19}F MRI using SF_6 . *Magn Reson Med* 2005;54(2):460-463.
32. Kuethe DO, Caprihan A, Gach HM, Lowe IJ, Fukushima E. Imaging obstructed ventilation with NMR using inert fluorinated gases. *J Appl Physiol* 2000;88(6):2279-2286.
33. Adolphi NL, Kuethe DO. Quantitative mapping of ventilation-perfusion ratios in lungs by ^{19}F MR imaging of T1 of inert fluorinated gases. *Magn Reson Med* 2008;59(4):739-746.

34. Ouriadov AV, Fox MS, Couch MJ, Li T, Ball IK, Albert MS. In vivo regional ventilation mapping using fluorinated gas MRI with an x-centric FGRE method. *Magn Reson Med* 2015;74(2):550-557.
35. Nouls J, Fanarjian M, Hedlund L, Driehuys B. A Constant-Volume Ventilator and Gas Recapture System for Hyperpolarized Gas MRI of Mouse and Rat Lungs. *Concepts Magn Reson Part B Magn Reson Eng* 2011;39B(2):78-88.
36. Gajawada G, Li T, Couch MJ, Fox MS, Albert MS. A 19F - 1H Linear Dual Tuned RF Birdcage Coil for Rat Lung Imaging at 3T. In *Proc 23rd Annual Meeting of ISMRM*, 2015. p 1461.
37. Santyr GE, Lam WW, Parra-Robles JM, Taves TM, Ouriadov AV. Hyperpolarized noble gas magnetic resonance imaging of the animal lung: Approaches and applications. *J Appl Phys* 2009;105:102004.
38. Deninger AJ, Mansson S, Petersson JS, Pettersson G, Magnusson P, Svensson J, Fridlund B, Hansson G, Erjefeldt I, Wollmer P, Golman K. Quantitative measurement of regional lung ventilation using 3He MRI. *Magn Reson Med* 2002;48(2):223-232.
39. Santyr GE, Couch MJ, Lam WW, Ouriadov A, Drangova M, McCormack DG, Holdsworth DW. Comparison of hyperpolarized (3) He MRI with Xe-enhanced computed tomography imaging for ventilation mapping of rat lung. *NMR Biomed* 2011;24(9):1073-1080.
40. Lam WW, Holdsworth DW, Du LY, Drangova M, McCormack DG, Santyr GE. Micro-CT imaging of rat lung ventilation using continuous image acquisition during xenon gas contrast enhancement. *J Appl Physiol* 2007;103(5):1848-1856.
41. Couch MJ, Ouriadov A, Santyr GE. Regional ventilation mapping of the rat lung using hyperpolarized 129Xe magnetic resonance imaging. *Magn Reson Med* 2012;68(5):1623-1631.
42. Emami K, Hamedani H, Kadlecek S, Han B, Xin Y, Ishii M, Rossman M, Rizi R. A pilot fractional ventilation imaging study in healthy subjects, asymptomatic smokers and obstructive pulmonary disease patients. In *Proc 21st Annual Meeting of ISMRM*, 2013. p 1463.
43. Imai H, Matsumoto H, Miyakoshi E, Okumura S, Fujiwara H, Kimura A. Regional fractional ventilation mapping in spontaneously breathing mice using hyperpolarized 129Xe MRI. *NMR Biomed* 2015;28(1):24-29.
44. Stephen MJ, Emami K, Woodburn JM, Chia E, Kadlecek S, Zhu J, Pickup S, Ishii M, Rizi RR, Rossman M. Quantitative assessment of lung ventilation and microstructure in an animal model of idiopathic pulmonary fibrosis using hyperpolarized gas MRI. *Acad Radiol* 2010;17(11):1433-1443.

45. West JB. Regional differences in the lung. *Chest* 1978;74(4):426-437.
46. Sa RC, Cronin MV, Henderson AC, Holverda S, Theilmann RJ, Arai TJ, Dubowitz DJ, Hopkins SR, Buxton RB, Prisk GK. Vertical distribution of specific ventilation in normal supine humans measured by oxygen-enhanced proton MRI. *J Appl Physiol* 2010;109(6):1950-1959.
47. Mansson S, Deninger AJ, Magnusson P, Pettersson G, Olsson LE, Hansson G, Wollmer P, Golman K. ³He MRI-based assessment of posture-dependent regional ventilation gradients in rats. *J Appl Physiol* 2005;98(6):2259-2267.
48. Escolar JD, Escolar MA, Blasco J, Ros LH. Airway and lung parenchyma morphology during the respiratory cycle. *Histol Histopathol* 2007;22(1):43-49.
49. Sarkar K, Katiyar A, Jain P. Growth and dissolution of an encapsulated contrast microbubble: effects of encapsulation permeability. *Ultrasound Med Biol* 2009;35(8):1385-1396.
50. Kruger SJ, Nagle SK, Couch MJ, Ohno Y, Albert M, Fain SB. Functional imaging of the lungs with gas agents. *J Magn Reson Imaging* 2015;DOI:10.1002/jmri.25002.
51. Ebner B, Behm P, Jacoby C, Burghoff S, French BA, Schrader J, Flogel U. Early assessment of pulmonary inflammation by ¹⁹F MRI in vivo. *Circ Cardiovasc Imaging* 2010;3(2):202-210.
52. Horn FC, Deppe MH, Marshall H, Parra-Robles J, Wild JM. Quantification of regional fractional ventilation in human subjects by measurement of hyperpolarized ³He washout with 2D and 3D MRI. *J Appl Physiol* 2014;116(2):129-139.
53. Horn FC, Marshall H, Siddiqui S, Horsley A, Smith L, Aldag I, Kay R, Taylor CJ, Parra-Robles J, Wild JM. Ventilation heterogeneity in obstructive airways disease – comparing multi-breath washout-imaging with global lung measurements. In *Proc 23rd Annual Meeting of ISMRM, 2015*. p 852.
54. Charles HC, MacIntyre NR, Moon R, Foster WM, McAdams HP, Ainslie M. In-Vivo Visualization Of Slow To Fast Filling Compartments In Human Lungs Using ¹⁹F MRI Of Perfluorinated Gases Mixed With Oxygen. *Am Respir Crit Care Med* 2014;189:A4348.
55. Charles C, Soher B, Halaweish AF. Modeling of the Spatio-Temporal Distribution of Pulmonary Ventilation via Perfluoropropane Gas Enhanced MRI. *Am Respir Crit Care Med* 2015:A2125.

Chapter 6

Discussion

6.1 Summary

Due to the significant prevalence of respiratory diseases, such as asthma, COPD, ILD, and CF, there is a need in the medical community for new technologies that can potentially aid in diagnosis and treatment management. Standard PFTs, such as spirometry and plethysmography, lack the regional information that imaging technologies are able to provide. Although imaging modalities such as CT, SPECT, and PET are able to obtain functional and regional information from the lung, they all use significant levels of ionizing radiation, which limits the potential for longitudinal assessment of the lung. Conventional ^1H MRI is a non-ionizing technique that is able to study lung structure and function; however, the image quality has historically been very poor. It is also unclear whether indirect ^1H -based imaging techniques, such as OE MRI and FD MRI can truly measure ventilation in the air spaces of the lung. With HP ^3He and ^{129}Xe MRI, it is possible obtain a direct measurement of lung function using a completely non-invasive and non-ionizing method. Although HP gas MRI has been a successful research tool for over 20 years, it may not be implemented into routine diagnostic imaging, since it is a technique that requires an expensive polarizer, scarce isotopes, and specialized personnel.

^{19}F MRI using inhaled inert fluorinated gases is a relatively new pulmonary imaging modality that can potentially provide high quality structural and functional images of the lungs. Inert fluorinated gases have the advantages of being nontoxic, abundant, relatively inexpensive, and the technique can be performed on any MRI scanner with broadband imaging capabilities. Therefore, inert fluorinated gas MRI has the potential to be clinically adopted as a pulmonary imaging modality that can aid in disease diagnosis. Inert fluorinated gas MRI of the lungs has been performed extensively in animals since the 1980s, and the measurement of various functional biomarkers has been demonstrated, such as ADC, fractional ventilation, wash-in/wash-out kinetics, and V/Q. Preliminary work in the lungs of healthy volunteers and patients with lung diseases has been reported recently, and improvements in image quality are ongoing. This thesis reports inert fluorinated gas MR imaging in healthy human volunteers and in animal models of pulmonary disease. Various imaging techniques were introduced, including static breath-hold ventilation imaging and preliminary measurements of functional image-derived biomarkers.

6.2 ^{19}F MRI Developments in Thunder Bay, Ontario

Chapter 2 discussed an initial feasibility study involving inert fluorinated gas imaging in healthy volunteers (1). Since initial reports of ^{19}F MRI in human lungs had a very poor image quality, it was hypothesized that a UTE approach would help to overcome the very short relaxation times of inert fluorinated gases. Thus, a ^{19}F UTE acquisition was optimized, and imaging was performed in a group of 10 healthy volunteers. In addition,

this work compared the image quality from two different gas breathing techniques: a single 1 L bolus inhalation that is commonly used for HP gas MRI, and continuous breathing from a large fluorinated gas reservoir. As expected, the continuous breathing method allowed for a greater ^{19}F spin density in the lungs, and hence a significantly improved image quality. Overall, the SNR from the optimized UTE approach and continuous breathing was a factor of about two times higher than previous results in the literature (2).

Since inert fluorinated gas MRI is still being developed and optimized, the work to date has reported stand-alone studies that used different techniques, different hardware, and different imaging parameters. Thus, the literature lacks quantitative comparisons between different types of ^{19}F image acquisitions. Chapter 3 discussed a quantitative comparison of inert fluorinated gas MR imaging that was performed in a group of 5 healthy volunteers using both UTE and gradient echo imaging (3). Although SNR from UTE imaging was significantly higher than gradient echo imaging, the UTE images suffered from blurring and poorly defined edges. These results were confirmed with similar imaging performed in a resolution phantom. Overall these data will help to guide future developments in ^{19}F MRI and the choice of pulse sequence parameters to be used in future imaging studies.

In addition to static breath-hold ventilation imaging, inert fluorinated gas MRI can potentially provide image-derived biomarkers that can yield insight into lung function and disease severity. Chapter 4 discussed initial efforts to quantify imaging biomarkers

using inert fluorinated gas MR images obtained in healthy volunteers. Ventilation defect measurements can provide indicators of airway obstruction, and a preliminary comparison to HP ^3He MR imaging suggested that ventilation defect volumes were indistinguishable between the two techniques (4). The ADC is a biomarker for microstructural changes in the lungs, and preliminary ^{19}F ADC maps were presented for a single healthy volunteer (5). Finally, gravitational gradients in ventilation are expected based on known patterns in lung physiology, and preliminary ^{19}F MRI measurements of gravitational gradients were presented for 6 healthy volunteers (5,6).

In order to demonstrate the potential of inert fluorinated gas MRI for detecting pulmonary diseases, it is worthwhile to pilot novel imaging biomarker measurements in animal models. Chapter 5 discussed inert fluorinated gas fractional ventilation mapping that was performed in rat models of inflammation and fibrosis (7). Fractional ventilation maps were obtained using an established dynamic wash-out imaging technique (8), and the results were compared between controls and rats that were instilled with LPS or bleomycin. There was a trend towards decreased ventilation values in LPS- and bleomycin-instilled rats, and these rats also had substantially different patterns of gravitational ventilation gradients. These results were confirmed with a comparison to histology.

6.3 Future Work

6.3.1 Reproducibility and Validation

As researchers consider the potential clinical implementation of inert fluorinated gas MRI, rigorous reproducibility and validation studies will be required. For example, various studies have established the reproducibility of HP ^3He MRI in COPD (9), CF (10) and in exercise-induced bronchoconstriction (11). One preliminary study at Duke University has demonstrated a reasonable reproducibility for inert fluorinated gas MR imaging in patients with asthma (12). Future work will evaluate the reproducibility of inert fluorinated gas MRI in larger cohorts, including both healthy individuals, as well as patients with various respiratory diseases.

Since ^{129}Xe has emerged as the preferred HP gas in recent years, quantitative comparisons between PFTs, CT, HP ^3He MRI, and HP ^{129}Xe MRI have helped to establish the clinical relevance of HP ^{129}Xe imaging (13,14). Furthermore, these quantitative validation studies can help researchers to understand how differences in the physical properties of the gases relate to differences in the measured biomarkers. Since SF_6 and PFP are both heavier than Xe, similar comparison studies will be required to help validate inert fluorinated gas MRI. Although the preliminary results presented in this thesis comparing ^{19}F MRI and HP ^3He MRI appear to be promising (Section 4.2), more subjects will be required in order to increase statistical power and to fully validate the technique.

6.3.2 Hardware Improvements

In general, the image SNR is a function of many variables, including spin density, relaxation, hardware, and pulse sequence parameters. Since the human imaging presented in this thesis used flexible coils shaped like a life vest, the coil design may have contributed to inhomogeneities in the excitation flip angle. Therefore, future quantification of image-based biomarkers will require corrections for B_1 inhomogeneities, and similar techniques have already been characterized for HP gas MRI (15). Alternatively, the application of novel RF coil designs may help to provide an improved SNR as well as more robust measurements of functional biomarkers. For example, Dregely et al. recently reported a ^{129}Xe coil that included a phased-array receiver and an asymmetric birdcage transmit coil (16). The asymmetric birdcage transmit coil maximizes space inside the scanner bore while providing a uniform B_1 excitation homogeneity. The 32-channel phased-array receive coil provides the SNR benefits of combining data many small coil elements that individually have a very high SNR (17).

The animal imaging presented in Chapter 5 made use of a linear dual-tuned $^1\text{H}/^{19}\text{F}$ birdcage RF coil (18). The purpose of using a dual-tuned RF coil was so that conventional ^1H localization and inert fluorinated gas imaging could be performed without moving the animal to change RF coils. Thus, the resulting ^1H and ^{19}F lung images will be perfectly co-registered. Likewise, the use of dual frequency coils might also allow for a more accurate comparison of HP ^3He , HP ^{129}Xe , and inert fluorinated gas imaging in humans. A dual-tuned $^{129}\text{Xe}/^3\text{He}$ RF coil has been recently reported for

simultaneous ^1H , ^3He , and ^{129}Xe imaging during a single breath-hold (19). Since the resonance frequency of ^{19}F is relatively close to the frequencies of ^3He and ^1H (see Table 1-1), it remains to be seen what dual-tuned coil designs will be possible.

Since inert fluorinated gases are used in numerous industrial applications, atmospheric concentrations of these gases have been increasing in recent decades. Furthermore, fluorinated gases are known to be potent greenhouse gases with long lifetimes (20). Therefore, efforts will be made to capture and recycle the exhaled fluorinated gases. For example, the MR-compatible gas delivery system reported by Halaweish et al. was designed to use a non-rebreathing valve that isolates the inspiratory and expiratory gases, so that the exhaled gases can be collected in a large reservoir (21). Similarly, the high cost of ^3He has motivated the development of devices that can capture ^3He gas and purify it after an imaging experiment (22).

6.3.3 Pulse Sequence Improvements

Various accelerated image acquisition techniques have been reported for HP ^3He MRI, such as parallel imaging (23) and compressed sensing (24). In essence, these techniques undersample the data acquisition such that spatial and/or temporal redundancies in the acquired data can be exploited to reconstruct the correct image. HP ^3He has the advantage of having an initially very large available magnetization that can be manipulated to obtain high quality accelerated images despite undersampling. Since inert fluorinated gases have a much lower available magnetization than HP gases, it remains to be seen how much of an advantage accelerated acquisition techniques can offer. Parallel imaging with inert

fluorinated gases will likely be explored in conjunction with the development of phased-array coil designs (25).

The use of a computer-controlled gas delivery system may also help improve the robustness of inert fluorinated gas images by gating long acquisitions. If the image acquisition is longer than a breath-hold, then data can be acquired over multiple respiratory cycles and the gas delivery system could trigger the acquisition so that data is only acquired during a particular portion of the respiratory cycle (21). A number of other gating methods have been successfully demonstrated for ^1H -based lung MRI, including the use of a respiratory bellows (26), navigator signals (27), or direct current (DC) signals from coil elements near the diaphragm (28). Although this thesis focused on developing optimized imaging techniques for 10 – 25 second breath-holds, the true power of inert fluorinated gas MRI may be realized by imaging during continuous breathing. Longer acquisitions will enable inert fluorinated gas lung imaging with a higher SNR and higher resolution.

Since pulmonary MR imaging is typically performed during a breath-hold, it is extremely difficult to perform repeated imaging at a consistent lung inflation state. Any errors in the inhaled lung volume will result in a change in the apparent lung size and gas distribution. Therefore, it may be extremely difficult to accurately compare conventional ^1H MRI and inert fluorinated gas MRI for the measurement of ventilation defects. For this reason, the human volunteers imaged in this thesis were coached to hold their breath at approximately $\text{FRC} + 1 \text{ L}$ for imaging. The use a computer-controlled gas delivery

system may help to alleviate issue by recording inhaled gas volumes; however, another approach might be to perform simultaneous ^1H and ^{19}F imaging following an inert fluorinated gas breath-hold. Simultaneous imaging of ^1H and HP ^3He lung imaging has been previously demonstrated, and it allows for a perfect co-registration of the anatomical information from conventional ^1H MRI and the functional information provided by HP ^3He MRI (29).

6.3.4 Functional Imaging

Dynamic imaging during continuous breathing of a mixture of inert fluorinated gas and O_2 can potentially provide physiologically meaningful indicators of lung function, such as wash-in/wash-out kinetics, fractional ventilation, and air trapping. The dynamic wash-out imaging technique presented in Chapter 5 could easily be translated to clinical imaging, as similar techniques have been reported in humans using HP ^3He imaging (30). Dynamic imaging using HP gases is challenging, since the HP magnetization has a finite lifetime, and polarizers typically have limited production rates. Inert fluorinated gases, on the other hand, are not subject to such restrictions. Preliminary reports of dynamic imaging in humans using inert fluorinated gas MRI have been presented at scientific meetings (31-33), and future work using optimized acquisition strategies will help to refine these techniques.

Pre-clinical imaging of animal models has been recognized as an important step in drug development, since imaging can provide functional biomarkers that relate to disease severity (34). Thus, inert fluorinated gas imaging of animal models will remain important

for the development of novel biomarkers as well as for validating biomarkers that have previously been established using HP gas MRI. Future work will likely continue to prototype novel pulse sequences (8), as well as improve dynamic imaging techniques (7), ADC measurements (35) and S/V ratio measurements (36). This work will help to refine novel inert fluorinated gas imaging techniques prior to clinical implementation.

6.4 Outlook

Although the first inert fluorinated gas images reported by Heidelberger and Lauterbur were extremely primitive, it was recognized in their 1982 abstract that gas phase MRI could potentially become an important component of pulmonary imaging technology (37). That statement still rings true today, as HP noble gas and inert fluorinated gas technology continues to evolve. The same group that originally co-pioneered HP noble gas MRI in 1994 is now helping to develop the next pulmonary imaging modality: inert fluorinated gas MRI. Once fully optimized, this technique may have a significant advantage over HP noble gas MRI, since it is inexpensive, the gases are abundant, and an expensive polarizer is not required. All of these developments and advantages may help lead to Health Canada regulatory approval for clinical imaging using inert fluorinated gas MRI.

Since this is a very new pulmonary imaging modality that is still under development, only healthy volunteers were imaged in this thesis. Dr. Mitchell Albert's research group at TBRI is currently seeking regulatory approval to perform inert fluorinated gas MR

imaging in patients with pulmonary diseases, such as COPD, asthma, lung cancer, lung transplants, mesothelioma, pulmonary embolism, ILD, and CF. Although inert fluorinated gas MRI has already been performed in patients with pulmonary diseases at Duke University, the reported imaging quality has been relatively poor, and there is a lack of quantitative functional data (2). Therefore, continued imaging in patients with pulmonary diseases will help to determine if inert fluorinated gas MRI can provide diagnostic information that is relevant and clinically meaningful.

Pulmonary inert fluorinated gas MRI can potentially help to address the disproportionately high rates of obstructive lung diseases in aboriginal populations. For example, aboriginals are 1.41 times more likely to have asthma (38) and up to 2.4 times more likely to have COPD (39) than non-aboriginals. There are a number of strong risk factors for obstructive lung diseases that are particularly prevalent in First Nations communities, such as smoking, second-hand smoke, and biomass burning. Therefore, the development of inert fluorinated gas MRI will provide a substantial benefit to aboriginal communities, since it is a technique that can provide many critical indicators of lung function, thereby providing insight into the burden of obstructive lung diseases. TBRRRI is also uniquely situated, since it has access novel lung imaging technologies, and there is a relatively large population (9.8%) of aboriginal individuals in the Thunder Bay community (40).

6.5 Conclusion

This thesis has presented a number of exciting developments in inert fluorinated gas MR imaging, including static breath-hold ventilation imaging and a number of image-derived biomarkers that may be important in detecting and understanding respiratory diseases. Inert fluorinated gas MRI can potentially provide functional lung information that is similar to HP ^3He and ^{129}Xe MRI, but without the need for scarce isotopes and expensive polarizer equipment. Overall, interest in pulmonary ^{19}F MRI of inert fluorinated gases is increasing, and numerous sites around the world are now interested in developing this technique. The ongoing improvements in image quality will allow for the continued investigation of novel and robust functional biomarkers, such as ADC, S/V, and fractional ventilation. Overall, inert fluorinated gas MRI has the potential to become a viable clinical imaging modality for non-invasively imaging the lung and for providing critical diagnostic information.

6.6 References

1. Couch MJ, Ball IK, Li T, Fox MS, Littlefield SL, Biman B, Albert MS. Pulmonary ultrashort echo time 19F MR imaging with inhaled fluorinated gas mixtures in healthy volunteers: feasibility. *Radiology* 2013;269(3):903-909.
2. Halaweish AF, Moon RE, Foster WM, Soher BJ, McAdams HP, MacFall JR, Ainslie MD, MacIntyre NR, Charles HC. Perfluoropropane gas as a magnetic resonance lung imaging contrast agent in humans. *Chest* 2013;144(4):1300-1310.
3. Couch MJ, Ball IK, Li T, Fox MS, Ouriadov AV, Biman B, Albert MS. Optimized Strategies for 19F MRI of Human Lungs and Comparison of UTE and Gradient Echo Imaging. In Proc 22nd Annual Meeting of ISMRM, 2014. p 777.
4. Couch MJ, Ball IK, Li T, Fox MS, Biman B, Albert MS. Comparing Pulmonary MRI using Inert Fluorinated Gases and Hyperpolarized 3He: Is 19F MRI Good Enough? In Proc 23rd Annual Meeting of ISMRM, 2015. p 1501.
5. Couch MJ, Ball IK, Li T, Fox MS, Ouriadov AV, Biman B, Albert MS. Inert fluorinated gas MRI: a new pulmonary imaging modality. *NMR Biomed* 2014;27(12):1525-1534.
6. Couch MJ, Ball IK, Li T, Fox MS, Biman B, Albert MS. Gravitational Distribution Gradient of Inert Fluorinated Gases in Human Lungs Using 19F Ultra-Short Echo Time MRI. In Proc 22nd Annual Meeting of ISMRM, 2014. p 2304.
7. Couch MJ, Fox MS, Viel C, Gajawada G, Li T, Albert MS. Fractional Ventilation Mapping using Inert Fluorinated Gas MRI in a Rat Model of Inflammation. In Proc 23rd Annual Meeting of ISMRM, 2015. p 1033.
8. Ouriadov AV, Fox MS, Couch MJ, Li T, Ball IK, Albert MS. In vivo regional ventilation mapping using fluorinated gas MRI with an x-centric FGRE method. *Magn Reson Med* 2015;74(2):550-557.
9. Mathew L, Evans A, Ouriadov A, Etemad-Rezai R, Fogel R, Santyr G, McCormack DG, Parraga G. Hyperpolarized 3He magnetic resonance imaging of chronic obstructive pulmonary disease: reproducibility at 3.0 tesla. *Acad Radiol* 2008;15(10):1298-1311.
10. O'Sullivan B, Couch M, Roche JP, Walvick R, Zheng S, Baker D, Johnson M, Botfield M, Albert MS. Assessment of repeatability of hyperpolarized gas MR ventilation functional imaging in cystic fibrosis. *Acad Radiol* 2014;21(12):1524-1529.

11. Niles DJ, Kruger SJ, Dardzinski BJ, Harman A, Jarjour NN, Ruddy M, Nagle SK, Francois CJ, Fain SB. Exercise-induced bronchoconstriction: reproducibility of hyperpolarized ^3He MR imaging. *Radiology* 2013;266(2):618-625.
12. Charles C, Baumgartner R, Carayannopoulos LN, Lugogo N, Kraft M, Railkar RA, Thornton B, Womack SJ, Ainslie MD, Halaweish AF, Moon RE, MacIntyre NR, Foster WM, Feng D, Macfall JR, Evelhoch J. Short Term Repeatability of Perfluorinated Gas Imaging in a Series of Subjects with Asthma (Mild and Moderate/Severe). *Am Respir Crit Care Med* 2015;191:A2256.
13. Kirby M, Svenningsen S, Kanhere N, Owrangi A, Wheatley A, Coxson HO, Santyr GE, Paterson NA, McCormack DG, Parraga G. Pulmonary ventilation visualized using hyperpolarized helium-3 and xenon-129 magnetic resonance imaging: differences in COPD and relationship to emphysema. *J Appl Physiol* 2013;114(6):707-715.
14. Kirby M, Svenningsen S, Owrangi A, Wheatley A, Farag A, Ouriadov A, Santyr GE, Etemad-Rezai R, Coxson HO, McCormack DG, Parraga G. Hyperpolarized ^3He and ^{129}Xe MR imaging in healthy volunteers and patients with chronic obstructive pulmonary disease. *Radiology* 2012;265(2):600-610.
15. Miller GW, Altes TA, Brookeman JR, De Lange EE, Mugler JP, 3rd. Hyperpolarized ^3He lung ventilation imaging with B1-inhomogeneity correction in a single breath-hold scan. *Magn Reson Mater Phy* 2004;16(5):218-226.
16. Dregely I, Ruset IC, Wiggins G, Mareyam A, Mugler JP, 3rd, Altes TA, Meyer C, Ruppert K, Wald LL, Hersman FW. 32-channel phased-array receive with asymmetric birdcage transmit coil for hyperpolarized xenon-129 lung imaging. *Magn Reson Med* 2013;70(2):576-583.
17. Roemer PB, Edelstein WA, Hayes CE, Souza SP, Mueller OM. The NMR phased array. *Magn Reson Med* 1990;16(2):192-225.
18. Gajawada G, Li T, Couch MJ, Fox MS, Albert MS. A ^{19}F - ^1H Linear Dual Tuned RF Birdcage Coil for Rat Lung Imaging at 3T. In Proc 23rd Annual Meeting of ISMRM, 2015. p 1461.
19. Rao M, Wild JM. RF instrumentation for same-breath triple nuclear lung MR imaging of H and hyperpolarized He and Xe at 1.5T. *Magn Reson Med* 2015.
20. Khalil MAK, Rasmussen RA, Culbertson JA, Prins JM, Grimsrud EP, Shearer MJ. Atmospheric perfluorocarbons. *Environ Sci Technol* 2003;37(19):4358-4361.
21. Halaweish AF, Charles HC. Physiorack: An integrated MRI safe/conditional, Gas delivery, respiratory gating, and subject monitoring solution for structural and functional assessments of pulmonary function. *J Magn Reson Imaging* 2014;39(3):735-741.

22. Lourette SA, Che AW, Woods JC, Conradi MS. Recovery and Purification of ^3He Gas from Pulmonary MRI. In Proc 19th Annual Meeting of ISMRM, 2011. p 887.
23. Lee RF, Johnson G, Grossman RI, Stoeckel B, Trampel R, McGuinness G. Advantages of parallel imaging in conjunction with hyperpolarized helium--a new approach to MRI of the lung. *Magn Reson Med* 2006;55(5):1132-1141.
24. Ajraoui S, Parra-Robles J, Marshall H, Deppe MH, Clemence M, Wild JM. Acquisition of (^3He) ventilation images, ADC, $T(2)^*$ and $B(1)$ maps in a single scan with compressed sensing. *NMR Biomed* 2012;25(1):44-51.
25. Charles HC, Jones RW, Halaweish AF, Ainslie MD. Parallel Imaging for Short Breath Hold Times in Perfluorinated Gas Imaging of the Lung. In Proc 23rd Annual Meeting of ISMRM, 2015. p 3984.
26. Johnson KM, Fain SB, Schiebler ML, Nagle S. Optimized 3D ultrashort echo time pulmonary MRI. *Magn Reson Med* 2013;70(5):1241-1250.
27. Oechsner M, Pracht ED, Staeb D, Arnold JF, Kostler H, Hahn D, Beer M, Jakob PM. Lung imaging under free-breathing conditions. *Magn Reson Med* 2009;61(3):723-727.
28. Fischer A, Weick S, Ritter CO, Beer M, Wirth C, Hebestreit H, Jakob PM, Hahn D, Bley T, Kostler H. Self-gated Non-Contrast-Enhanced Functional Lung imaging (SENCEFUL) using a quasi-random fast low-angle shot (FLASH) sequence and proton MRI. *NMR Biomed* 2014;27(8):907-917.
29. Wild JM, Ajraoui S, Deppe MH, Parnell SR, Marshall H, Parra-Robles J, Ireland RH. Synchronous acquisition of hyperpolarised ^3He and ^1H MR images of the lungs - maximising mutual anatomical and functional information. *NMR Biomed* 2011;24(2):130-134.
30. Horn FC, Deppe MH, Marshall H, Parra-Robles J, Wild JM. Quantification of regional fractional ventilation in human subjects by measurement of hyperpolarized ^3He washout with 2D and 3D MRI. *J Appl Physiol* 2014;116(2):129-139.
31. Charles HC, MacIntyre NR, Moon R, Foster WM, McAdams HP, Ainslie M. In-Vivo Visualization Of Slow To Fast Filling Compartments In Human Lungs Using ^{19}F MRI Of Perfluorinated Gases Mixed With Oxygen. *Am Respir Crit Care Med* 2014;189:A4348.
32. Halaweish AF, Foster WM, Moon RE, MacIntyre NR, MacFall JR, Charles HC. Dynamics of Pulmonary Ventilation Distribution at Steady State via ^{19}F Fluorine-Enhanced MRI: Initial Experiences and Future Developments. In Proc 21st Annual Meeting of ISMRM, 2013. p 4111.

33. Charles C, Soher B, Halaweish AF. Modeling of the Spatio-Temporal Distribution of Pulmonary Ventilation via Perfluoropropane Gas Enhanced MRI. *Am Respir Crit Care Med* 2015:A2125.
34. Beckmann N, Kneuer R, Gremlich HU, Karmouty-Quintana H, Ble FX, Muller M. In vivo mouse imaging and spectroscopy in drug discovery. *NMR Biomed* 2007;20(3):154-185.
35. Carrero-Gonzalez L, Kaulisch T, Stiller D. In vivo diffusion-weighted MRI using perfluorinated gases: ADC comparison between healthy and elastase-treated rat lungs. *Magn Reson Med* 2013;70(6):1761-1764.
36. Jacob RE, Chang YV, Choong CK, Bierhals A, Zheng Hu D, Zheng J, Yablonskiy DA, Woods JC, Gierada DS, Conradi MS. ¹⁹F MR imaging of ventilation and diffusion in excised lungs. *Magn Reson Med* 2005;54(3):577-585.
37. Heidelberg E, Lauterbur PC. Gas Phase ¹⁹F-NMR Zeugmatography: A New Approach to Lung Ventilation Imaging. In *Proc 1st Annual Meeting Society of Magnetic Resonance in Medicine*, 1982. p 70-71.
38. Ospina MB, Voaklander DC, Stickland MK, King M, Senthilselvan A, Rowe BH. Prevalence of asthma and chronic obstructive pulmonary disease in Aboriginal and non-Aboriginal populations: a systematic review and meta-analysis of epidemiological studies. *Can Respir J* 2012;19(6):355-360.
39. Ospina MB, Voaklander D, Senthilselvan A, Stickland MK, King M, Harris AW, Rowe BH. Incidence and Prevalence of Chronic Obstructive Pulmonary Disease among Aboriginal Peoples in Alberta, Canada. *PLoS One* 2015;10(4):e0123204.
40. National Household Survey: Statistics Canada; 2011.

Appendix A: Research Ethics Board Approval



Research Ethics Board

May 30, 2012

Dr. Mitchell Albert albertma@tbh.net
Thunder Bay Regional Research Institute
980 Oliver Road
Thunder Bay, Ontario P7B 6V4

Dear Dr. Albert,

Re: Project Number: TBRHSC REB # 2011138
 Project Title: Hyperpolarized Noble Gas (3He) MR Imaging for Pulmonary Disorders
 Initial Approval: January 23, 2012 - January 23, 2013

The Thunder Bay Regional Health Sciences Centre Research Ethics Board (TBRHSC REB) conducted a full board review of the research study referenced above on January 23, 2012. REB approval includes the following:

- TBRHSC REB Application dated May 3, 2012, received May 22, 2012,
- Clinical Study Protocol version 5 received May 14, 2012,
- Healthy Volunteer Consent Form version 6, received May 14, 2012,
- Lung Disorder Consent Form version 6, received May 23, 2012,
- Detailed Study Budget received December 29, 2011
- Recruitment Flyer received February 14, 2012,
- Referral Form for Research Study Participation version 3 received February 14, 2012,
- Protocol Synopsis and Evaluation version 3 dated, received February 14, 2012,
- Participant Information Form, version 2, received February 14, 2012,
- IB Hyperpolarized Noble Gas (3HE) MR Imaging for Pulmonary Disorders version 2, dated November 1, 2011 received December 29, 2011,
- Health Canada No Objection letter dated March 23, 2012,
- Health Canada Investigational Testing Authorization dated January 31, 2012,
- Lakehead University initial REB approval dated May 11, 2012,
- Lakehead University REB Amendment Approval letter dated May 24, 2012,
- Research Development Committee endorsement dated December 12, 2011.

Quorum was free from conflict and did not involve any member directly associated with this project. TBRHSC REB is guided by the Tri-Council Policy Statement: Ethical Conduct for Research Involving Human Subjects and ICH: Good Clinical Practice (GCP) guidelines.

If this project includes accompanying contracts or agreements to be signed by TBRHSC (e.g., industry-sponsored clinical trials, researchers' agreements) research activity **must not** begin until the contract has been executed.

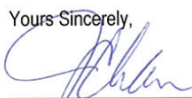


Research Ethics Board

Continuing ethics review is the responsibility of the Principal Investigator. Any changes to the approved research study (e.g., information letter, consent form) must be submitted to the TBRHSC REB for review and approval using the appropriate forms. Additional reporting may be required depending on research methodology (e.g., serious adverse events, protocol deviations). REB approval is required should your project extend beyond the approval period noted above. Upon completion/termination of the study, you are required to submit a Study Completion Report. All forms are available at:

http://www.tbrhsc.net/about_TBRHSC/research_ethics/forms.asp

Yours Sincerely,



Jeff Chan, RPh PharmD
Chair, TBRHSC REB

Individuals accessing medical records or paper charts for the purposes of research are required to contact Information Systems and/or Health Records **before** accessing records. The Principal Investigator will be required to request access to files for research purposes for themselves and/or any member of his/her research team.

TBRHSC Information Systems contact information:

Dawn Bubar: bubard@tbh.net, Tel: (807) 684-6429

TBRHSC Health Records contact information:

Heidi Greenwell: greenweh@tbh.net Tel: (807) 684-6641

Description of Research Team

Research
Ethics Office
Room 1534 – Level 1
980 Oliver Road
Thunder Bay, Ontario
Canada P7B 6V4
Tel.: (807) 684-6422
e-mail: REO@tbh.net

Principal Investigator:	Dr. Mitchell Albert Thunder Bay Regional Research Institute Room 3106 980 Oliver Road Thunder Bay, Ontario P7B 6V4 (807) 684-7270 albertma@tbh.net
Co-Investigator(s):	Dr. Birubi Biman Internal Medicine Thunder Bay Regional Health Sciences Centre bbiman@hotmail.com
Best Contact for Project:	Dr. Mitchell Albert

e-copied: Research Development Committee, TBRHSC
Research Ethics Office, TBRHSC

Lakehead

UNIVERSITY

Office of Research Services

May 11, 2012

Tel 807-343-8934
Fax 807-346-7749

Principal Investigator: Dr. Mitchell S. Albert
Co-Investigators: Drs. Biman and Kisselgoff
Thunder Bay Regional Research Institute
980 Oliver Road
Thunder Bay, ON P7B 6V4

Dear Dr. Albert, Biman and Kisselgoff:

Re: REB Project #: 131 11-12 / Romeo File No: 1462537
Granting Agency: TBRII start-up funds
Granting Agency Project #: N/A

On behalf of the Research Ethics Board, I am pleased to grant ethical approval to your research project titled, "Hyperpolarized Noble Gas (3He) MR Imaging for Pulmonary Disorders".

Ethics approval is valid until May 11, 2013. Please submit a Request for Renewal form to the Office of Research Services by April 11, 2013 if your research involving human subjects will continue for longer than one year. A Final Report must be submitted promptly upon completion of the project. Research Ethics Board forms are available at:

http://research.lakeheadu.ca/ethics_resources.html

During the course of the study, any modifications to the protocol or forms must not be initiated without prior written approval from the REB. You must promptly notify the REB of any adverse events that may occur.

Completed reports and correspondence may be directed to:

Research Ethics Board
c/o Office of Research Services
Lakehead University
955 Oliver Road
Thunder Bay, ON P7B 5E1
Fax: (807) 346-7749

Best wishes for a successful research project.

Sincerely,



Dr. Richard Maundrell
Chair, Research Ethics Board

/scw



Research Ethics Board

Research Ethics Office
Room 1534 – Level 1
980 Oliver Road
Thunder Bay, Ontario
Canada P7B 6V4
Tel.: (807) 684-6422
e-mail: REO@tbh.net



November 19, 2012

Dr. Mitchell Albert albertmi@tbh.net
Thunder Bay Regional Research Institute
Room 3106
980 Oliver Road
Thunder Bay, Ontario P7B 6V4

Dear Dr. Albert,

Re:	Project Number:	TBRHSC REB # 2012124
	Project Title:	Development of a Functional Imaging Protocol Using Magnetic Resonance Imaging of the Lungs with Inhaled Inert Fluorinated Gases as Contrast Agents
	Initial Approval:	October 22, 2012 - October 22, 2013

The Thunder Bay Regional Health Sciences Centre Research Ethics Board (TBRHSC REB) conducted a full board review of the research study referenced above on October 22, 2012. REB approval includes the following:

- TBRHSC REB Application received October 26, 2012,
- Response to TBRHSC REB's requests for clarifications received October 26, 2012,
- Clinical Study Protocol Version 3 dated and received October 26, 2012,
- Information Letter/Consent Form - Version 2 dated and received October 26, 2012,
- Case Report Form 1 and 2- Versions 1 dated July 2012, received September 19, 2012,
- MRI Patient Screening Form-FCS-052 dated June 2011, received September 19, 2012,
- Detailed Study Budget dated and received September 19, 2012,
- Recruitment Poster received November 9, 2012,
- Health Canada Qualified Investigator Undertaking (Birubi Biman) dated August 7, 2012, received September 19, 2012,
- Health Canada Investigational Testing Authorization Letter dated September 13, 2012, received September 19, 2012,
- Health Canada No Objection dated September 21, 2012, received September 26, 2012,
- Investigator's Brochure-Sulfur Hexafluoride, Perfluoropropane Version 1 dated January 1, 2012 received September 19, 2012,
- RDC Proposal endorsement dated January 30, 2012, received September 19, 2012
- Lakehead University Research Ethics Board Approval dated and received November 16, 2012.

Quorum was free from conflict and did not involve any member directly associated with this project. TBRHSC REB is guided by the Tri-Council Policy Statement: Ethical Conduct for Research Involving Human Subjects and ICH: Good Clinical Practice (GCP) guidelines.

If this project includes accompanying contracts or agreements to be signed by TBRHSC (e.g., industry-sponsored clinical trials, researchers' agreements) research activity **must not** begin until the contract has been executed.

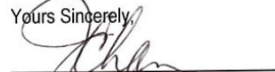
...2/

-2-

Continuing ethics review is the responsibility of the Principal Investigator. Any changes to the approved research study (e.g., information letter, consent form) must be submitted to the TBRHSC REB for review and approval using the appropriate forms. Additional reporting may be required depending on research methodology (e.g., serious adverse events, protocol deviations). REB approval is required should your project extend beyond the approval period noted above. Upon completion/termination of the study, you are required to submit a Study Completion Report. All forms are available at:

http://www.tbrhsc.net/about_TBRHSC/research_ethics/forms.asp

Yours Sincerely,



Jeff Chan, RPh PharmD
Chair, TBRHSC REB

Individuals accessing medical records or paper charts for the purposes of research are required to contact Information Systems and/or Health Records **before** accessing records. The Principal Investigator will be required to request access to files for research purposes for themselves and/or any member of his/her research team.

TBRHSC Information Systems contact information:

Dawn Bubar: bubard@tbh.net, Tel: (807) 684-6429

TBRHSC Health Records contact information:

Heidi Greenwell: greenweh@tbh.net Tel: (807) 684-6641

Description of Research Team

Principal Investigator:	Dr. Mitchell Albert Thunder Bay Regional Research Institute Room 3106 980 Oliver Road Thunder Bay, Ontario P7B 6V4 (807) 684-7270 albertmi@tbh.net
Co-Investigator(s):	Dr. Birubi Biman bbiman@hotmail.com Dr. David Kisselgoff (kisselgd@tbh.net)
Best Contact for Project:	Dr. Mitchell Albert

e-copied: Heidi Greenwell, Health Records, TBRHSC
Steven Exley, Diagnostic Imaging, TBRHSC
Jeanine Lewis, Purchasing, TBRHSC
Research Development Committee, TBRHSC
Research Ethics Office, TBRHSC

Lakehead

UNIVERSITY

Office of Research Services

November 16, 2012

Tel 807-343-8934
Fax 807-346-7749

Principal Investigator: Dr. Mitchell S. Albert
Co-Investigators: Dr. Birubi Biman, Dr. David Kisselgoff, Marcus Couch, Tao Li
TBRRI
980 Oliver Road, Room 3119
Thunder Bay, ON P7B 6V4

Dear Researchers:

Re: REB Project #: / Romeo File No: 1462943
Granting Agency: TBRRI Start-up Funds
Granting Agency Project #: N/A

On behalf of the Research Ethics Board, I am pleased to grant ethical approval to your research project titled, "Development of a functional imaging protocol using MRI of the lungs with inhaled inert fluorinated gases as MR contrast agents".

Ethics approval is valid until November 16, 2013. Please submit a Request for Renewal form to the Office of Research Services by October 16, 2013 if your research involving human subjects will continue for longer than one year. A Final Report must be submitted promptly upon completion of the project. Research Ethics Board forms are available at:

http://research.lakeheadu.ca/ethics_resources.html

During the course of the study, any modifications to the protocol or forms must not be initiated without prior written approval from the REB. You must promptly notify the REB of any adverse events that may occur.

Completed reports and correspondence may be directed to:

Research Ethics Board
c/o Office of Research Services
Lakehead University
955 Oliver Road
Thunder Bay, ON P7B 5E1
Fax: (807) 346-7749

Best wishes for a successful research project.

Sincerely,



Dr. Richard Maundrell
Chair, Research Ethics Board

/scw

Lakehead Research...CREATING THE FUTURE NOW

955 Oliver Road Thunder Bay Ontario Canada P7B 5E1 www.lakeheadu.ca

Appendix B: Animal Care Committee Approval



Office of Research

(807) 343-8283
(807) 346-7749

MEMORANDUM

Date: July 8, 2013

To: Dr. Mitchell Albert, Dr. Matthew Fox, TBRR1

From: Dr. Brian McLaren, Acting Chair, Animal Care Committee

Subject: Approval for AUP #04 2013 / Romeo #1463130

Thank you for providing the Lakehead University Animal Care Committee the amendments requested at the March 19, 2013 ACC meeting for your research study titled, "Magnetic Resonance Imaging of Dissolved and Gas Phase Xenon in Rat Lungs".

The project has received positive peer review with no requested amendments from reviewers.

On behalf of the Committee, I am pleased to inform you that the project has been **approved**.

If any amendments are required throughout the life of the project, please complete a Protocol Modification Form for submission to the ACC. Annually the ACC will request you renew your protocol as needed.

Once your project has been completed, please inform Sue Wright (swright@lakeheadu.ca) so that your file can be closed.

Animal Care Committee forms are available through the Romeo Research Portal at:

<http://romeo.lakeheadu.ca>

Best wishes for success with your project.

Sincerely,

A handwritten signature in black ink that reads "Brian McLaren".

Dr. B. McLaren
Acting Chair, Animal Care Committee

/scw